EFFECTS OF ROADSIDE STRUCTURES ON NEAR-ROAD AIR QUALITY AND IMPLICATIONS FOR ROADWAY DESIGN

A Dissertation

Presented to the Faculty of the Graduate School

of Cornell University

in Partial Fulfillment of the Requirements for the Degree of

Doctor of Philosophy

by

Jonathan Thomas Steffens

January 2015

EFFECTS OF ROADSIDE STRUCTURES ON NEAR-ROAD AIR QUALITY AND IMPLICATIONS FOR ROADWAY DESIGN

Jonathan Thomas Steffens, Ph.D.

Cornell University 2015

Near road air quality is a growing concern for urban developers and transportation engineers as exposure to common vehicle emissions has been linked to numerous adverse health effects. Roadway design is being considered as one potential solution for mitigating exposure for those living and working nearby. This work examines the effectiveness of various roadway configurations, such as elevations and depressions, as well as the presence of solid barriers, such as those erected to reduce noise pollution, and vegetation barriers. Various experimental work has shown the potential benefits of these features. However, there is still a lack of mechanistic understanding of how they impact the air flow and pollutant transport in the near-road environment.

In this work, we propose that Computational Fluid Dynamics (CFD) models can be utilized to further our understanding in this regard. To this end, we first use existing experimental data to validate our CFD model. Once validated, we can use the computational model to observe any number of other configurations. We find that flat terrain often has worse pollutant concentrations at grade than any of the other roadway configurations. Solid barriers near roadways in particular can reduce ground level concentrations by up to 80%. However, there are potential drawbacks, such as higher concentrations at higher elevations and higher on-road concentrations. Furthermore, vegetation barriers often have mixed results. They enhance particle deposition, but often lead to

increased concentrations due to lower convective and turbulent transport.

In the latter part of this work, we aim to use the knowledge gained from our computational simulations to help create a simple parameterized model to characterize pollutant transport near roadside barriers. CFD models are computationally very expensive and require extensive understanding in order to properly use. We propose a modification to Gaussian plume dispersion models to account for the impact of both solid and vegetative barriers. This model is shown to be only slightly less accurate than the CFD model while saving large amounts of computational time. In doing this we hope to make our findings more accessible to those who will need to utilize them for policy making decisions.

BIOGRAPHICAL SKETCH

Jonathan received a B.S. from the Rochester Institute of Technology in 2009 graduating with highest honors as part of the RIT honor college. He also earned his M.S. from RIT in 2009 as well, as part of the RIT dual degree program. His master's research, under the mentorship of Risa Robinson, involved computational modeling of cigarette smoke particle deposition. Specifically, he studied the difference in deposition between an adult and an adolescent lung by constructing computer models based on Computerized Tomography (CT) scans and performing Computational Fluid Dynamics analysis. After graduating from RIT, he began to study at Cornell University in pursuit of his Ph.D. While there, he joined the Energy and the Environment Research Lab (EERL) under the mentorship of his adviser K. Max Zhang. His primary work has focused on studying the effects of roadside structures such as solid noise barriers and vegetation on vehicle exhaust dispersion. Initially, he focused on CFD models, but transitioned into developing simpler parameterizations to incorporate into Gaussian plume dispersion models. Jonathan is also a member of the American Association of Aerosol Research (AAAR) and has given several presentations at their annual conference.

For Mom and Dad, whom I never call enough.

ACKNOWLEDGEMENTS

None of my accomplishments would be possible without the support and assistance of numerous individuals. First, I would like to thank Dr. K. Max Zhang, my primary adviser and mentor for the past five years at Cornell. He was always there to lend advice when I asked and to give motivation when I needed it. I would also like to thank Dr. Risa Robinson, my adviser at RIT. She introduced to me academic research and for that I will be forever grateful. And thank you to the faculty and staff of Cornell, who are always eager to answer a question, and in particular Zellman Warhaft and Martin Wells for serving on my committee. I would like to thank David Heist, Steven Perry, Gayle Hagler, and Rich Baldauf of the Environmental Protection Agency, Dennis Finn of the National Oceanic and Atmospheric Administration, and Andrey Khlystov of Duke University for sharing valuable research data and even more valuable insight into its analysis. Finally, and perhaps most importantly, I would like to thank my family for their continual support and encouragement. I would not be where I am without you and I would not be who I am without you.

TABLE OF CONTENTS

LIST OF TABLES

LIST OF FIGURES

CHAPTER 1

INTRODUCTION

Exposure to traffic related air pollutants (TRAP) has been linked to a wide variety of health concerns including respiratory and cardiovascular problems, birth and developmental defects, and cancer (HEI, 2010). On road air quality is also a matter of concern to those who live in urban environments or spend long periods of time commuting. Of those who do live near roadways, a disproportionately high number are from low income families (Houston et al., 2008) making the issue one of social justice in addition to public health. It is critical to develop policies which are effective in improving near road air quality by mitigating pollution levels. It becomes important then, to try to find alternative methods of mitigating near road pollutant levels beyond vehicle emission control. It may be possible that the roadway design itself can be such that it improves air quality. This design may include raised or depressed highways or roadside barriers (Baldauf et al., 2009). For instance, the Federal Highway Administration (FHWA) has started investigating the cost effectiveness of using National Highway System (NHS) right of way (ROW) and roadside vegetation barriers for carbon sequestration (Earsom et al., 2010).

Wind tunnel experiments (Hagler et al., 2011; Heist et al., 2009), an atmospheric tracer study (Finn et al., 2010) and several field measurements (Baldauf et al., 2008; Bowker et al., 2007; Nokes and Benson, 1984) have shown that solid and vegetative barriers may significantly lower pollutant concentrations when compared to a roadway with no barriers. It has also been observed that noise barriers may have an adverse effect on pollutant concentrations (Lidman, 1985) and that pollutant concentration levels may increase on the highway side when

a noise barrier is present, thus increasing harmful exposure for motorists (Baldauf et al., 2008; Nokes and Benson, 1984). The effect of vegetation on the wind field and microclimate have been investigated (Cleugh, 1998; Santiago et al., 2007) as well as the effects of vegetation height, wind speed and wind angle on the wind characteristics (Wilson, 2004a,b). Vegetation barriers may also providing ecological benefits such as soil conservation and carbon sequestration. As it pertains to pollutant levels, vegetation elements may improve air quality by enhancing turbulent mixing and providing a source of deposition for pollutants, primarily particulate matter (Bouvet et al., 2007; Raupach et al., 2001). However, few studies have observed the plume transport across and through the vegetation barriers. In addition, the effects of vegetation on pollutant deposition are unclear (Buccolieri et al., 2009; Gromke et al., 2008; Gromke and Ruck, 2007), with decreases and increases in concentration behind vegetative barriers have also been observed (Maerschalck et al., 2008). Disagreement in the literature pertaining to the effect of roadside structures necessitates further research on the matter. It is clear, though, that roadside structures do affect plume dispersion and concentration levels near the roadway. Since these barriers are extremely common, it is necessary to deepen our understanding of these structures in order to make informed policy decisions.

In Chapter 2, Chapter 3, and Chapter 4, we first develop and apply numerical modeling tools to analyze and supplement existing experimental data. While experiments provide essential empirical evidence, they are often prohibitively expensive to cover a sufficient range of road, traffic and meteorological conditions. However, computational models are not similarly constrained. Our general approach is to use Computational Fluid Dynamics (CFD) models to simulate previous experiments. In doing this we hope to provide confidence in

our numerical approach. From there, we will simulate a number of other supplementary conditions in order to broaden our understanding of how near-road pollutant concentration responds to a variety of parameters.

CFD, while providing a high degree of accuracy, is nonetheless still rather complicated to properly set-up and requires extensive knowledge to properly perform. Additionally, high fidelity models can be quite computationally expensive. Many urban planners and environmental regulators use very simple and very fast models (often taking only minutes to complete), such as Gaussian Plume Dispersion models, in order to characterize near-road pollutants. These models, while shown to be accurate for flat terrain do not account for the effects of solid or vegetative barriers. In Chapter 5 and Chapter 6, we work to develop modifications to the Gaussian Plume Dispersion model to account for these effects. Our goal is to create a model which only requires a few, known inputs, such as barrier height, wind speed, and atmospheric stability which runs on the framework of Gaussian Plume Dispersion models while retaining sufficient accuracy so as to still give useful results.

CHAPTER 2

MODELING THE EFFECTS OF A SOLID BARRIER ON POLLUTANT DISPERSION UNDER VARIOUS ATMOSPHERIC STABILITY CONDITIONS

There is a growing need for developing mitigation strategies for near-road air pollution. Roadway design is being considered as one of the potential options. Particularly, it has been suggested that sound barriers, erected to reduce noise, may prove effective at decreasing pollutant concentrations. However, there is still a lack of mechanistic understanding of how solid barriers affect pollutant transport, especially under a variety of meteorological conditions. In this study, we utilized the Comprehensive Turbulent Aerosol Dynamics and Gas Chemistry (CTAG) model to simulate the spatial gradients of SF6 concentrations behind a solid barrier under a variety of atmospheric stability conditions collected during the Near Road Tracer Study (NRTS08). We employed two different CFD models, RANS and LES. A recirculation zone, characterized by strong mixing, forms in the wake of a barrier. It is found that this region is important for accurately predicting pollutant dispersion, but is often insufficiently resolved by the less complex RANS model. The RANS model was found to perform adequately away from the leading edge of the barrier. The LES model, however, performs consistently well at all flow locations. Therefore, the LES model will make a significant improvement compared to the RANS model in regions of strong recirculating flow or edge effects. Our study suggests that advanced simulation tools can potentially provide a variety of numerical experiments that may prove useful for roadway design communities to intelligently design roadways, making effective use of roadside barriers.

2.1 Introduction

Studies have shown that people who live, work, or go to school near roadways are at risk for a variety of health problems, including respiratory and cardiovascular problems, birth and developmental defects, and cancer, due to exposure to harmful traffic-related air pollutants (HEI, 2010). In addition to vehicle emissions control, there are potential opportunities for mitigating near-road air pollution in roadway design options that affect pollutant transport and dispersion such as road configurations and the presence of roadside barriers (Baldauf et al., 2008; Bowker et al., 2007; Cahill, 2010). Designing or evaluating roadside barriers to maximize their benefits requires a mechanistic understanding on how barrier geometry location and traffic and meteorological conditions affect the fate and transport of traffic-related air pollutants. Recent wind tunnel experiments and field measurements (Heist et al., 2009; Finn et al., 2010) have begun to characterize the effects of roadside barriers. Additionally, much work has recently been done with experiment and simulation in urban street canyons (Chang and Meroney, 2003; Neophytou et al., 2011; Xie and Castro, 2009). However, significant knowledge gaps exist in terms of both our fundamental understanding and practical applications of using roadside barriers to mitigate near-road air pollution.

This paper continues our efforts in developing predictive tools in elucidating the effects of roadside barriers on near-road air quality. Our modeling framework is called the Comprehensive Turbulent Aerosol Dynamics and Gas Chemistry (CTAG) model. It is a computational fluid dynamics (CFD)-based environmental turbulent reacting flow model designed to simulate the transport and transformation of multiple air pollutants on and near roadways, taking into

consideration roadway design including vehicle induced turbulence (VIT) created by vehicular traffic and roadway induced turbulence (RIT) created by the roadway design such as roadway configurations, roadside buildings and roadside barriers (Wang and Zhang, 2009, 2012; Wang et al., 2011; Tong et al., 2011). Previously, we created and evaluated a computational model within the CTAG framework to assess the impact of a roadside vegetation barrier (Steffens et al., 2012). Our sensitivity analysis suggests that fully capturing the flow field is critical to improving the prediction of particle size distributions. While some computational models have been applied to urban environments (Gowardhan et al., 2011; Hanna et al., 2002), relatively few modeling studies have specifically addressed the case of solid barriers, such as sound walls. And those that have typically used only simplistic flow models (Hagler et al., 2011). Modeling can provide insight into the behavior of air flow and pollutant transport in these areas.

In this paper, we apply two CFD models to investigate the effects of a solid barrier on downwind pollutant concentrations. The models we employ are the Reynolds Averaged Navier-Stokes (RANS) model and the Large Eddy Simulation (LES) model. The RANS model requires a turbulence model to close the system and the LES model requires a subgrid model, as described in Section 2.2. There are a number of options for these models. Since the goal of this work is the comparison of RANS and LES in general, we have selected basic, commonly used models. We utilize the k- turbulence model and the Smagorinsky-Lilly subgrid model for the RANS and LES models, respectively. The RANS model is often used due to its wide general applicability and fairly low computational cost. The LES model offers overall greater accuracy but at the cost of much higher computational times, due to finer meshing requirements and the

requirement of an unsteady flow solver. There are three main objectives in our study: 1) to examine the capabilities of different CFD models in resolving the flow fields and pollutant transport behind a solid barrier by comparing model predictions with field measurements under a variety of atmospheric stability conditions; 2) to quantify the accuracy of both a RANS and LES model in order to give guidelines for when a less complex model is appropriate and when a more complex model is needed; and 3) to deepen our understanding on the underlying physical mechanisms that contribute to pollutant transport across the solid barrier with the validated models. All three objectives will help further improve the CTAG model in terms of simulating the effects of roadside barriers.

2.2 Model Description

The CTAG model contains the functionality to fully resolve the flow field including turbulent reacting flows, aerosol dynamics and gas chemistry. More information about the model is found in Wang and Zhang (2009) and Wang and Zhang (2012), Wang et al. (2011), and Tong et al. (2011). The CTAG model employs ANSYS Fluent commercial software package (ANSYS, 2009) as the CFD flow solver. Flow simulations are often highly sensitive to the type of flow model employed. As such, this paper will investigate the effects of both a RANS model and a LES model on the flow field simulations. Both the RANS and LES flow models are derived from the Navier-Stokes and Continuity equations and must include further models to fully close the system of equations. In this paper, the RANS model employs the k-e turbulent flow solver to compute the turbulence field and the LES model employs the Smagorinsky-Lilly subgrid model.

The RANS equations are derived by averaging the instantaneous velocities in the governing equations. Mass conservation is given by the equation:

$$\frac{\partial u_i}{\partial x_i} = 0 \tag{2.1}$$

and the Reynolds Averaged Navier-Stokes (RANS) equations can be written as:

$$\rho u_j \frac{\partial u_i}{\partial x_j} = -\frac{\partial P}{\partial x_i} + \mu \frac{\partial}{\partial x_j}\left(\frac{\partial u_i}{\partial x_j} + \frac{\partial u_j}{\partial x_i}\right) - \rho \frac{\partial \overline{u_i' u_j'}}{\partial x_j} + S_u \tag{2.2}$$

where ρ is the fluid density, u_i is the ith component of velocity, x_i is the direction vector, P is pressure, μ is viscosity, $\overline{u_i' u_j'}$ is the Reynolds Stress tensor and S_u is any additional source term.

This averaging creates a closed system except for the Reynolds Stress term that is introduced. Various methods for computing this property exist. Eddy viscosity models, such as the k- model, relate the Reynolds Stresses to the mean flow by way of a turbulent eddy viscosity using the Boussinesq eddy viscosity assumption. The $k - \varepsilon$ model computes the eddy viscosity and closes the system by introducing transport equations for turbulent kinetic energy, TKE, and turbulent dissipation, ε, given by Jones and Launder (1972):

$$u_j \frac{\partial k}{\partial x_j} = \frac{\partial}{\partial x_j}\left(\frac{\mu_t}{\rho \sigma_k} \frac{\partial k}{\partial x_j}\right) + P_k - \varepsilon + S_k \tag{2.3}$$

$$u_j \frac{\partial \varepsilon}{\partial x_j} = \frac{\partial}{\partial x_j}\left(\frac{\mu_t}{\rho \sigma_\varepsilon} \frac{\partial \epsilon}{\partial x_j}\right) + C_1 \frac{\varepsilon}{k} P_k - C_2 \frac{\varepsilon^2}{k} + S_\varepsilon \tag{2.4}$$

where P_k is the production of turbulent kinetic energy and C_1 and C_2 are model

constants. The model constants were selected based on the values given in Launder and Sharma (1974) which have been found to be sufficiently accurate for a wide variety of turbulent flows.

The LES model is formulated based on the principal that important flow properties, such as momentum, mass, and energy, are transported primarily by the larger eddies in the flow. Additionally, large eddies are more dependent on the specific problem configuration, i.e. geometry and inlet conditions, while small eddies tend to behave more universally. As such, LES models explicitly resolves the large scale eddies found in turbulent flow by solving filtered Navier-Stokes equations. Smaller eddies, residing in the subgrid, are modeled. LES is much more computationally expensive than RANS models in part because the LES model requires an unsteady numerical scheme. Additionally, resolution of the turbulent eddies requires a finer grid than is necessary for a RANS model. In practice, LES schemes explicitly resolve the eddies that contain the majority of the flow energy, usually 80% or more (Pope, 2000). Further resolution of the turbulent eddies requires smaller grid size, which in turn requires a smaller time step, increasing the computational time by many factors. Thus, LES strikes a balance between the less accurate RANS models and fully resolving the flow, such as a Direct Numerical Simulation (DNS). The filtered forms of the continuity and Navier-Stokes equations given by:

$$\frac{\partial p}{\partial t} + \frac{\partial}{\partial x_i}\left(\rho\overline{u_i}\right) = 0 \tag{2.5}$$

$$\frac{\partial}{\partial t}\left(\rho\overline{u_i}\right) + \frac{\partial}{\partial x_i}\left(\rho\overline{u_i u_j}\right) = \frac{\partial}{\partial x_j}\left(\mu\frac{\partial \sigma_{ij}}{\partial x_j}\right) - \frac{\partial \overline{P}}{\partial x_i} - \frac{\partial \tau_{ij}}{\partial x_j} \tag{2.6}$$

where σ_{ij}, and τ_{ij} are given by:

$$\sigma_{ij} = \left[\mu\left(\frac{\partial\overline{u_i}}{\partial x_j} + \frac{\partial\overline{u_j}}{\partial x_i}\right)\right] - \frac{2}{3}\mu\frac{\partial\overline{u_i}}{\partial x_i}\delta_{ij} \tag{2.7}$$

$$\tau_{ij} = \rho\overline{u_i u_j} - \rho\overline{u_i} * \overline{u_j} \tag{2.8}$$

$$\tau_{ij} - \frac{1}{3}\tau_{kk}\delta_{ij} = -2\mu_t\overline{S_{ij}} \tag{2.9}$$

where S_{ij} is the rate of strain tensor and δ_{ij} is the Kronecker delta. We employ the Smagorinsky-Lilly subgrid model (Smagorinsky, 1963; Lilly, 1992) given by:

$$\mu_t = \rho L_s^2|\overline{S_{ij}}| \tag{2.10}$$

where L_s is the mixing length.

2.3 Measurement Data

We evaluated our simulations against the data collected from Near Roadway Tracer Study (NRTS08), which was conducted near the Idaho National Laboratory (INL) by the Air Resources Laboratory (ARL) of the National Oceanic Atmospheric Administration (NOAA) and in collaboration with the Atmospheric Modeling and Analysis Division of the U.S. Environmental Protection Agency (EPA). A detailed description of the experiment can be found in Finn et al. (2010). A brief summary is presented here. The experiment was performed in order to characterize the effect of a solid barrier on tracer gas concentration

under a variety of atmospheric stability conditions. In the experiment, a solid barrier 6 m high by 90 m long was erected from straw bales in an open field near the INL in order to approximate a typical solid sound barrier found near many highways. A tracer gas, Sulfur Hexaflouride (SF6), was released from a 54 m line source located 6m upwind of the barrier. This gas was chosen due to negligible background concentrations. An array of bag samplers, depicted in Figure 2.1, was used to measure the spatial gradients of SF6 concentration behind the barrier at various downwind and crosswind locations and in an identical configuration in a nearby clearing (i.e., without a barrier).

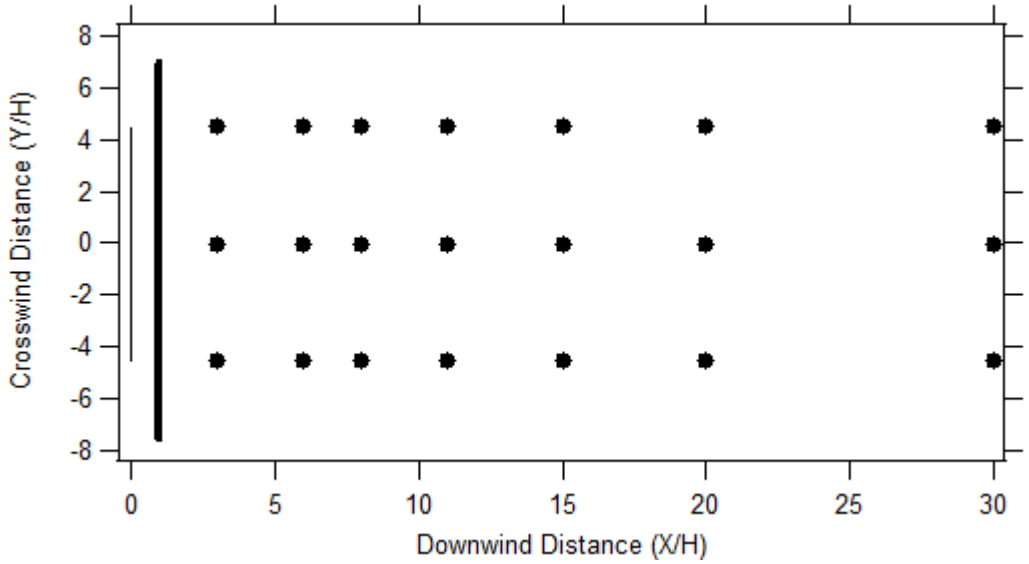

Figure 2.1: Schematic showing measurement points for the barrier site in NRTS08. The clearing site has the same configuration except the presence of the barrier. Solid barrier is bold line. The thin line represents the line source. Samplers are represented by dots.

All heights and distances have been normalized by the barrier height, i.e. H = 6 m. Anemometers were placed 6H downwind of the tracer release point at vertical heights of $0.5H$, $1H$, and $1.5H$ and $11H$ downwind of the tracer release point at a height of $0.5H$ in order to characterize the aerodynamic effect of the

barrier. A meteorological tower with 1 Hz anemometers at 3 m and 30 m vertically was used to characterize the approach flow of the atmospheric boundary layer including wind speed, wind direction, turbulence characteristics, friction velocity, and atmospheric stability. Additionally, a nearby mesonet tower measured wind speed at 10 m height. All recorded measurements are conservatively considered accurate to within 20%, and usually accurate within 10%.

2.4 Geometry, Mesh and Boundary Conditions

A geometry representing the experimental site was created and meshed in ANSYS Gambit. Separate domains were created for the clearing site and the barrier site. Each domain has dimensions of 300 m long, 180 m wide and 100 m high. The barrier is placed 30 m from the inlet of the domain and the domain extends 90 m past the location of the final sampling point to ensure there is no interference from the boundaries of the domain outlet on the measurement comparison (Cowan et al., 1997). A small emissions zone was created measuring 54 m long by 0.25 m wide and 0.25 m high centered 1 m above ground level placed 6 m upwind of the barrier. A structured mesh consisting of 4,178,431 elements for the barrier case and 561,600 elements for the no barrier case was created. The high number of elements in the barrier case is a result of the need to create a finer mesh in the region near the barrier. A mesh refinement test showed this level of refinement to be necessary to accurately resolve the LES model. A coarse mesh containing approximately one eighth the number of elements for both the barrier and no barrier cases and a more refined mesh containing approximately four times the number of elements were created. The RANS model showed virtually no difference in velocity or concentration results between the

three meshes for either the barrier or no barrier cases. For the LES model, the difference between the coarse and nominal meshes for any of the velocity or concentration results was no more than 6%. The more refined mesh showed only slight differences with the nominal mesh, showing at most a 2% difference. It is assumed that the huge computational increase from the more refined mesh is too great for the marginal benefit in accuracy.

In addition to the geometry, boundary conditions are required in order to perform the simulation. The ground and barrier are considered to be a no-slip wall. The inlet of the domain is set to be a velocity inlet, where profiles of wind speed, TKE and turbulent dissipation must be provided. The outlet is assumed to be a simple outflow condition. The top of the domain, assumed to be sufficiently far away from the barrier as to not affect the flow in the area, is set to a no-shear condition. The sides of the domain are set to periodic boundary conditions. Careful attention is needed at the inlet of the domain as inlet flow conditions will greatly affect the simulation results. The meteorological tower measurements of wind speed at 3 m and 30 m height were used to generate the inlet velocity profile. Since two measurement points at different heights were available, the standard power law atmospheric boundary layer profile, given by Equation 11, was used to fit the data.

$$U(z) = U_{ref}\left(\frac{z}{z_{ref}}\right)^{p} \tag{2.11}$$

where U_{ref} is the velocity at reference height z_{ref} and p is an empirically determined coefficient which increases with increasing surface roughness and increasing atmospheric stability (Huang, 1979).

Since this is a two parameter model, the model is fully constrained by the tower measurements. The 10 m mesonet tower was used to validate the use of the power low profile by comparing the experimental measurement with predicted 10 m velocity from model. The error was found to be 5.00%, 4.54%, and 4.76% for the stable, neutral, and unstable cases, respectively, which indicate that we were able to capture the inlet velocity profiles with good accuracy.

Additionally, turbulence characteristics must be specified at the inlet to the domain. For the steady $k-\varepsilon$ model, this included TKE and turbulent dissipation. TKE was determined from the filtered velocity data according to the equation:

$$TKE = \frac{1}{2}\left(u'^2 + v'^2 + w'^2\right) \tag{2.12}$$

where u', v', and w' are the fluctuating components of the velocity in the x, y, and z directions, respectively. Turbulent dissipation was characterized by the equation:

$$\varepsilon = zu^{*3}/\kappa \tag{2.13}$$

where u^* is the friction velocity and κ is the Von Karman constant equal to 0.41. For the unsteady LES simulation, instantaneous velocity fields must be generated at the domain inlet. A vortex method based on the Spectral Synthesizer method is used (Kraichnan, 1970; Smirnov et al., 2001). The method produces a perturbation to the mean velocity at each grid point and time step based on the inlet TKE and turbulent dissipation.

2.5 Modeling Scenarios

For this study, we consider several representative subsets of the experimental data. The subsets of data were selected based on the criteria of statistically steady flow properties and various atmospheric stability, as discussed below. We are interested in a validating the model under a variety of atmospheric stability classes. The applicability of various flow models to represent various atmospheric stability conditions is an active topic of research (Hargreaves and Wright, 2007; Pontiggia et al., 2009). For this work, we are careful to select periods of data that exhibit strongly steady conditions to minimize any potential issues with varying atmospheric conditions.

An important parameter in characterizing atmospheric stability is the Monin-Obukhov Length (Obukhov, 1971), which is interpreted, physically, as the height at which the production of turbulence from both buoyancy and wind shear is equal and is given by the equation:

$$L = \frac{-u^{*3}\rho c_p T}{\kappa g q} \tag{2.14}$$

where c_p is the specific heat of air, T is absolute temperature, g is gravitational acceleration and q is vertical heat flux at the surface. Typically, atmospheric stability is presented as the ratio z/L, which non-dimentionalizes vertical height by the Monin-Obukhov Length. Finn et al. (2010) computed the atmospheric stability parameter, z/L, for each data set, calculated from the turbulence measurements at the no barrier site, upwind of the tracer release line, and presented scenarios representing stable, neutrally stable, and unstable conditions. Generally speaking, a neutrally stable atmosphere corresponds to a stability param-

eter of zero, while more positive and negative z/L values correspond to more stable and unstable conditions, respectively.

For our study, a subset of data from each of these three scenarios was selected for simulation and comparison. The data subsets will be selected on the basis of statistically steady wind speed, i.e. the mean wind speed does not fluctuate, even though the instantaneous wind speed does. This selection criterion will allow for a more appropriate comparison between the models. Since we only use the RANS model to simulate steady flow conditions and the LES model is necessarily unsteady, we can use the statistically steady experimental data and compare it to both the RANS results and an ensemble average of the LES results. In order to characterize statistical steadiness, the anemometer data was filtered using a simple first-order low pass filter. The high frequency data was used to determine turbulence characteristics and the low frequency data is assumed to be the mean wind flow. We considered only time periods where the mean flow maximum and minimum differ by less than 5%. While the anemometer data was collected at 1 Hz, the SF6 bag samplers only report 15-min mean concentrations. Therefore, to ensure we have applicable concentration data, only subsets of wind velocity data which begin and end at 15 minute intervals are considered. We selected the longest continuous subsets of data which conform to the above conditions. The total measurement time for the scenarios representing stable, neutral, and unstable atmospheric stabilities were found to be 90, 60, and 45 minutes, respectively. Table 2.1 summarizes the measured velocity for each of the modeled time periods as well as wind direction as measured from perpendicular to the barrier, turbulent kinetic energy, friction velocity ($u*$) and atmospheric stability parameter (z/L) and the duration of the sample period.

Table 2.1: Inlet flow velocity, turbulence, and atmospheric stability for stable, neutral, and unstable scenarios

Atmospheric Stability	u(z=3m) (ms^{-1})	u(z=30m) ($m\ s^{-1}$)	Direction (degrees)	TKE (m^2s^{-2})	u* (ms^{-1})	z/L	Duration (min)
Stable	3.61	8.71	8.1	0.3224	0.3110	0.048	90
Neutral	7.44	10.75	14.3	1.2503	0.8087	-0.015	60
Unstable	1.65	2.14	-28.1	0.1056	0.2925	-0.312	45

2.6 Results and Discussion

Simulation results were obtained for the three atmospheric stability conditions for both the barrier and no barrier cases for both the RANS and LES models. Additionally, we performed a sensitivity analysis to characterize the effects of wind speed and direction on pollutant transport.

2.6.1 Velocity Results

Figure 2.2 shows the vertical velocities behind the barrier for each case comparing the $k-\varepsilon$ and LES to experimental measurements. Flow around a barrier is often highly complex. Recirculation zones, formed in the wake of the barrier and characterized by strong mixing, are regions where a flow vortex attaches to the downwind side of the barrier as seen by the vector plot given in Figure 2.3. Additionally, the flow moving around the edge of the barrier can be observed to deflect inward towards the barrier, sometimes causing secondary recirculation. These edge effects can be observed in Figure 2.4, which shows the flow around the leading edge of the barrier.

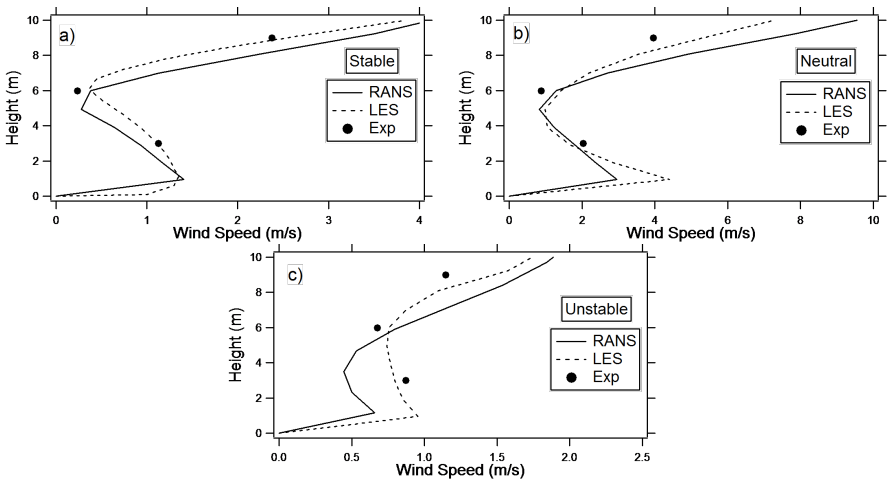

Figure 2.2: Vertical velocity profiles 4H downwind for scenarios: a) stable, b) neutral, and c) unstable

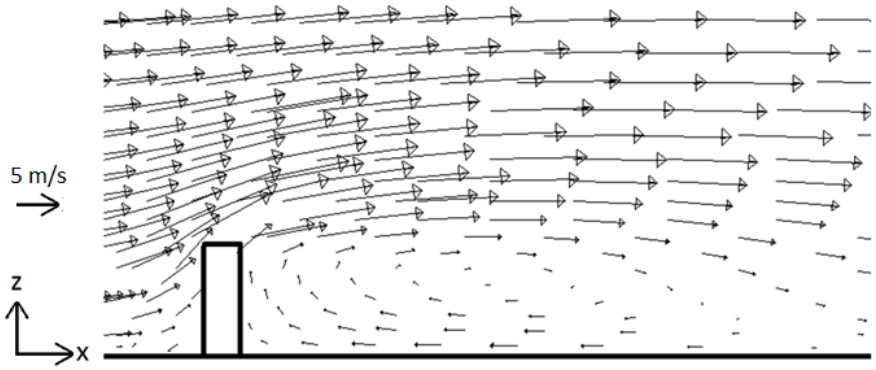

Figure 2.3: Illustration of flow recirculation shown by velocity vectors of side view along plume center plane perpendicular to the barrier. Aspect Ratio is 1:1.

From Figure 2.2 it is clear that both RANS and LES perform generally well at capturing the general shape of the recirculation zone behind the barrier. Table 2.2 tabulates mean fractional error (MFE) for these velocity results. MFE is a statistic used to capture the overall difference between two sets of data given by the equation:

$$MFE = \frac{1}{N}\sum_{i=1}^{N}\frac{C_{1,i} - C_{2,i}}{C_{1,i} + C_{2,i}/2} \tag{2.15}$$

where N is the total number of comparison points and C_1 and C_2 are the two sets of data to be compared.

Table 2.2: Mean fractional error (MFE) between simulation and experiment behind the barrier for vertical velocity at $x/H = 4$ for stable, neutral, and unstable scenarios

Atmospheric Stability	RANS	LES
Stable	0.248	0.136
Neutral	0.261	0.225
Unstable	0.248	0.102

The LES MFE is lower in all three scenarios, indicating the superiority of the LES model in capturing recirculating flow. It should be noted that some of the errors that seem high at around 25% MFE can be attributed to the sharp velocity gradients around the measurement points.

Experimental data for wind speed is available only along the center of the barrier. However, it is also beneficial to compare how the two turbulence models behave in the region near the leading edge of the flow, where secondary recirculation due to edge effects occurs. The vector plots in Figure 2.4 show the comparison of the two models. There are two distinct differences between the models common to all three scenarios we can observe. First, the flow upwind of the barrier is observed to deflect in the negative y direction a greater distance before the barrier for the LES model as compared with the RANS model. Second, the flow around the edge turns back towards the barrier more sharply for the RANS model. It should be noted that these differences are larger for the

stable and neutral cases than the unstable case. This is likely due to the lower wind speed in the unstable case causing less overall flow recirculation.

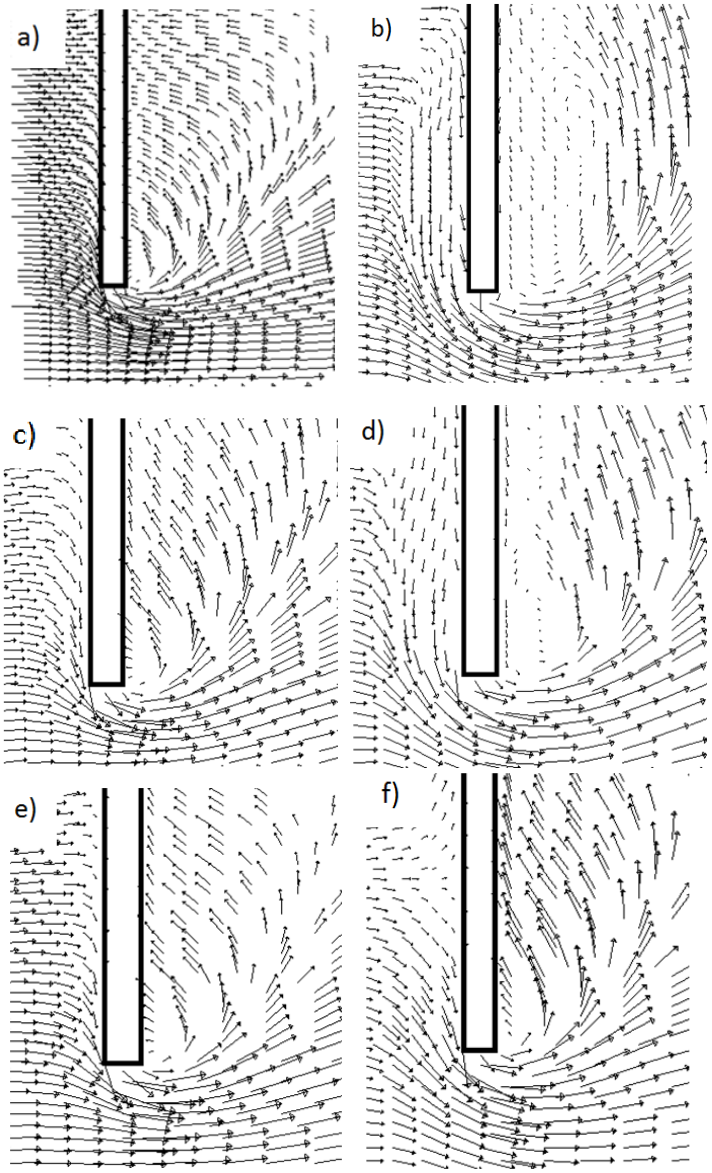

Figure 2.4: Velocity vectors for overhead view, at vertical height of 3m, near $y/H = -4.5$ (Figure 2.1) showing the leading 50 m of the 500 m barrier for cases a) stable RANS, b) stable LES, c) neutral RANS, d) neutral LES, e) unstable RANS, f) unstable LES. Aspect Ratio is 1:1.

2.6.2 Tracer Concentration Results

No Barrier Cases

Figure 2.5 shows the tracer results in the clearing along several lines of constant crosswind distance according to Figure 2.1 comparing the experimental data to the RANS model. Results were obtained at crosswind distances of $+4.5H$, $0H$, and $-4.5H$. Concentration, C, has been normalized similarly to Finn et al. (2010), by:

$$\chi = \frac{\rho c u_r L_x L_y}{Q} \tag{2.16}$$

where ρ is the tracer density, u_r is the reference wind speed at the clearing at 3 m height, L_x is the length of the line source, L_y is the virtual roadway length, and Q is the release rate. LES model results are not included in the figure due to the close similarity to the RANS results. For most points, the difference between the RANS and LES models is less than 5%, only becoming larger than that, but no larger than 10%, in the unstable case past $x/H = 20$. The results from the clearing site show a large degree of accuracy between both models and the experiment for each of the atmospheric stability classes, as seen by the mean fractional error (MFE) results in Table 2.3. There are 3 cases where the RANS model performs better than the LES model, but all of these cases occur when both models produce MFE values less than 0.1. Therefore both models still perform well and the fact that the RANS model performs slightly better is inconsequential. Likely, the lack of any disturbances in the flow field from the barrier reduces the complexity of the flow. For these cases, a lower accuracy turbulence model, such as RANS, is sufficient to capture the flow fields without a barrier.

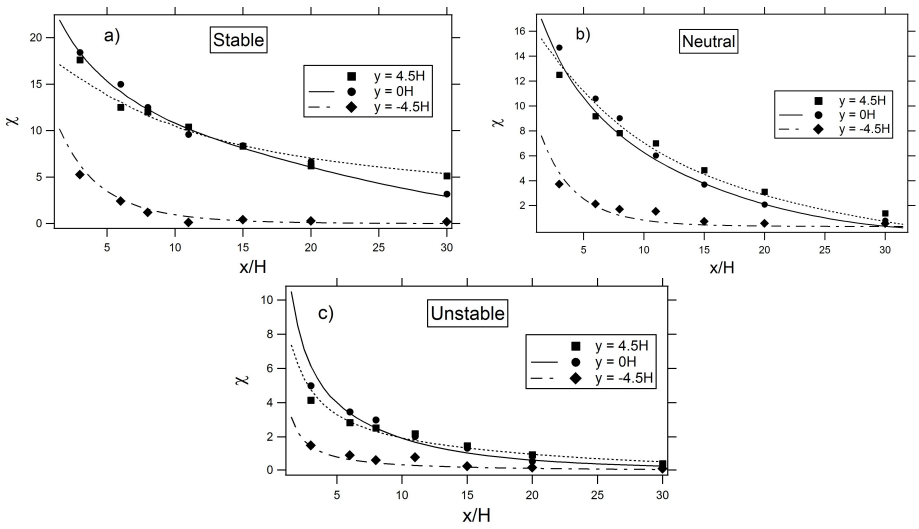

Figure 2.5: Normalized tracer concentration, χ, given by Equation 2.15, for clearing sites comparing experiment (markers) to RANS model (lines), for scenarios: a) stable, b) neutral, and c) unstable. LES results not included due to close similarity to RANS results

Barrier Cases

The presence of the barrier creates a much more complex flow field. Figure 2.6 shows the concentration results for each of the stability cases for both RANS and LES at crosswind locations of $4.5H$, $0H$, and $-4.5H$. It is clear that the LES model performs generally better than the RANS model, as seen by the mean fractional error (MFE) tabulated in Table 2.3. Additionally, the LES model shows to be highly accurate for almost all scenarios, while the RANS model shows the same level of accuracy for only some of the scenarios. The only scenario where the RANS model performs slightly better than the LES model is the unstable case at $y/H = 4.5$, where the MFE values are 0.093 and 0.135 for the RANS and LES models, respectively, indicating that both models perform very well for this particular case. The regions where LES performs significantly better than RANS are at $y/H = -4.5$ for each scenario, which is near the leading edge of the flow. This

corresponds to Figure 2.4, where the largest discrepancies between the RANS and LES flow fields are observed and described in Section 2.6.1. Likely, LES is needed to better resolve the complex flow phenomena that occur there.

Table 2.3: Mean Fractional Error (MFE) between experiment and the RANS and LES models behind the barrier and in the clearing for SF6 concentration for stable, neutral, and unstable cases

Atmospheric Stability	Location	No Barrier RANS	No Barrier LES	Barrier RANS	Barrier LES
Stable	-4.5H	.353	.349	.251	.177
	0H	.033	.064	.105	.088
	4.5H	.038	.054	.091	.059
Neutral	-4.5H	.101	.091	.645	.175
	0H	.099	.086	.137	.092
	4.5H	.237	.214	.251	.221
Unstable	-4.5H	.073	.090	.717	.107
	0H	.118	.097	.155	.133
	4.5H	.214	.198	.093	.135

Overall, it is found that the LES model performs better than the RANS model for most cases for both velocity and concentration measurements. The region where the two models differed the most in velocity, i.e. $y/H = -4.5$, they also differed the most in concentration. This is reasonable since velocity is a large driver of tracer gas transport.

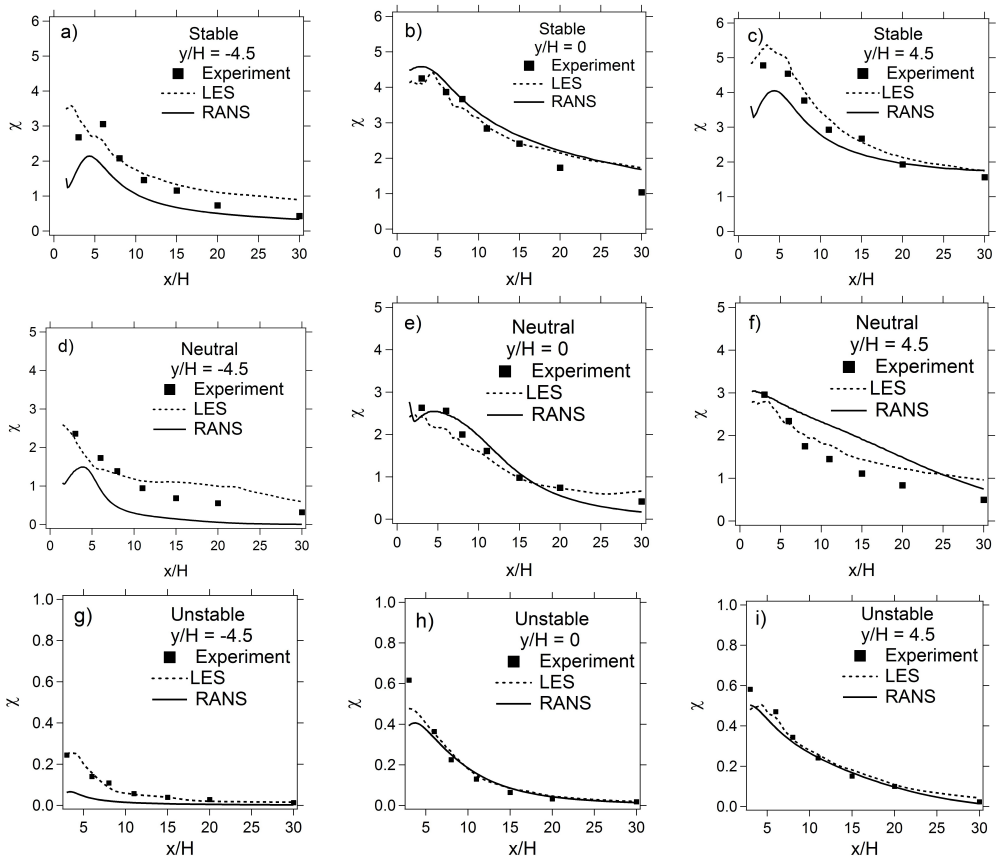

Figure 2.6: Profiles of normalized tracer concentration, χ, given by Equation 2.15 comparing experimental data to RANS and LES models for a) stable $y/H = -4.5$, b) stable $y/H = 0$, c) stable $y/H =$ 4.5, d) neutral $y/H =$ -4.5, e) neutral $y/H = 0$, f) neutral $y/H =$ 4.5, g) unstable $y/H =$ -4.5, h) unstable $y/H = 0$, i) unstable y/H = 4.5

2.6.3 Sensitivity Studies

Sensitivity studies were performed to examine how variations in wind speed and wind direction affect concentration results, and particularly observe the effect from the edge and recirculation effects. For these studies, the neutrally stable condition was used as the baseline case. All simulations are performed using the LES model.

To test the effect of wind speed, simulations were performed using an identical inlet wind profile multiplied by a constant value of two or one half. Figure 2.7 compares the concentration for the baseline case as well as the double and half wind speed cases. The results show that decreasing wind speed decreases the rate at which tracer can be transported away, thus increasing the tracer concentration. The double velocity case has the opposite effect. For a truly neutral atmospheric stability, we might expect the concentrations to be exactly proportional to wind speed. Thus wind speed should have no effect on . However, small differences are observed. The discrepancy is likely due to slight deviations from true neutral stability and potential additional effects from the edge of the barrier.

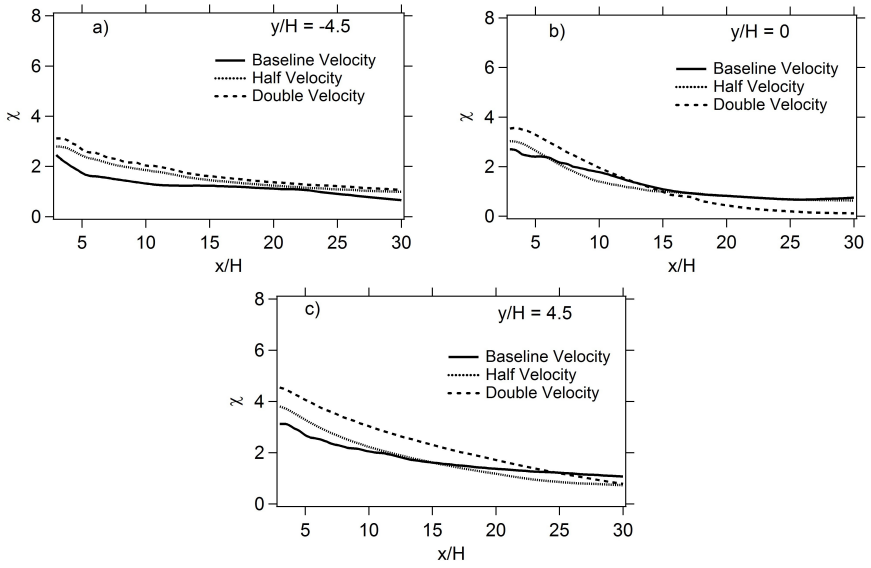

Figure 2.7: Normalized downwind concentration, χ, given by Equation 2.15, sensitivity to wind speed for a) y/H = -4.5, b) y/H = 0, and c) y/H = 4.5

Figure 2.8 shows the velocity vectors for each of the three cases along the plume center. The general shape of the recirculation zone behind the barrier was found to be the same for each case, but it can be seen in the figure that the

faster the wind speed, the larger the recirculation zone. It might be expected that at sufficiently high Reynolds number and neutral stability, the size of the recirculation zone would be independent of wind speed, further indicating that we may not have truly neutral conditions. Since this region is marked by a large amount of recirculating air, it is expected that there will be more mixing with higher wind speed, thus leading to more gradual decrease in concentration, as observed in Figure 2.7. It is also expected that the faster the wind speed, the stronger the edge effects become. Therefore, higher wind speeds are more likely to require a more accurate turbulence model such as LES.

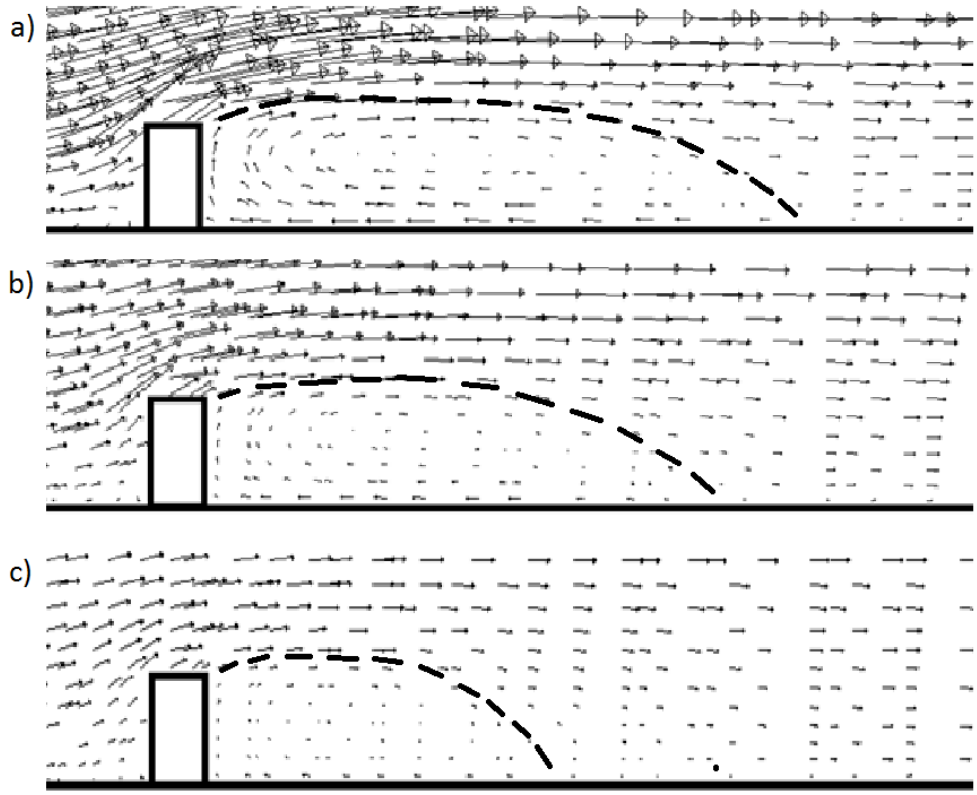

Figure 2.8: Velocity vectors along plume center for wind speed sensitivity, showing domain extending 6H downwind of barrier. Recirculation zone demarcated with dashed line. Scenarios a) double velocity, b) baseline velocity, and c) half velocity. Aspect Ratio is 1:1.

The effect of wind direction is more complex. For the sensitivity analysis, wind angle is measured from the line perpendicular to the barrier, i.e. perpendicular = 0 degrees. We consider three wind angles: the baseline case of 14 degrees, perpendicular to the barrier, and an angle of 30 degrees. Concentration results are shown in Figure 2.9. For the perpendicular case, the results at $y/H = \pm 4.5$ are identical and lower in concentration than those at $y/H = 0$, as we expect the flow to be symmetric and disperse horizontally, leading to lower concentrations away from $y/H = 0$. For the more oblique 30 degree case, the concentration at $+4.5H$ is much greater than the concentration at $0H$. The concentration at $-4.5H$ is insignificant. In the case of the more oblique wind angle, unlike the other cases, the tracer gas does not flow around the leading edge of the barrier. Additionally, the concentrations at $+4.5H$ and $0H$ decrease much more rapidly than the other cases as the plume has greater transport in the crosswind direction.

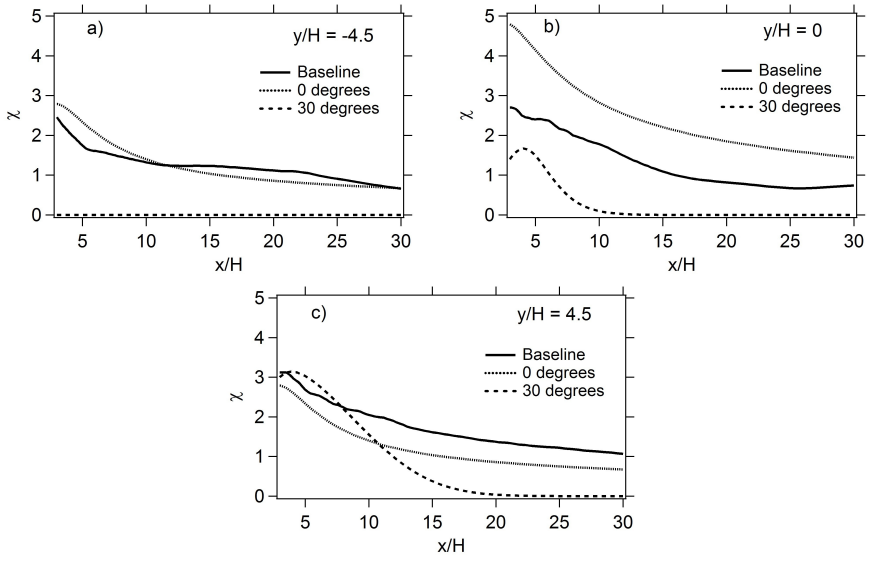

Figure 2.9: Normalized downwind concentration, χ, given by Equation 2.15, sensitivity to wind direction for a) y/H = -4.5, b) y/H = 0, and c) y/H = 4.5

Figure 2.10 shows contour plots of the velocity. The greatest crosswind transport is seen for the 30 degree wind angle, as expected. The figure also shows that the region of low velocity which denotes a recirculation zone is smaller for the more oblique wind angle and larger for the perpendicular wind angle. Additionally, the edge effects become stronger for more oblique wind angles. Thus, we expect the concentration to reach the background level faster for a more oblique wind angle as the pollutant is transported laterally more quickly. LES is expected to be more appropriate for large wind angles relative to a barrier.

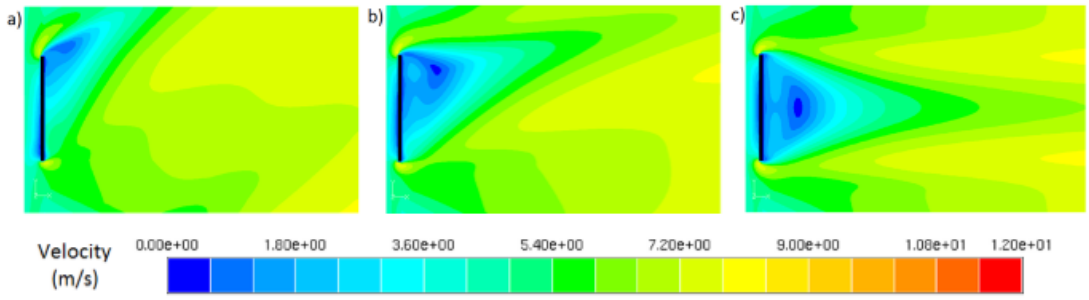

Figure 2.10: Velocity contours of entire domain at vertical height 3 m for wind direction sensitivity for a) 30 degrees, b) baseline, and c) perpendicular scenarios. Aspect Ratio is 1:1.

2.7 Conclusions and Recommendations

The CTAG model was used to simulate tracer gas concentrations downwind of a solid barrier and in a nearby clearing. Both a RANS model and a LES model were used to simulate the turbulent flow fields and SF6 dispersion and compared with the NRTS08 dataset. Flow around a solid barrier creates a recirculation zone characterized by an attached vortex downwind of the barrier. It was found that both models are able to capture the general shape of the recirculation

zone and velocity and concentration trends. However, for most cases, the LES model was shown to be more accurate overall and to be consistently accurate across all scenarios. In particular, the LES performed better in regions of strong edge effects and recirculation found along the leading edge of the barrier. In these regions of complex flow phenomenon, a more accurate turbulence solver is required.

Due to the high computational cost of the LES model, however, it is helpful to consider the circumstances under which a more simplistic RANS model is sufficiently accurate. Since the greatest inaccuracies appear to stem from edge effects, and these edge effects were found to be stronger during periods of more oblique wind angle or faster wind speeds, a RANS model becomes more applicable the slower and more perpendicular the flow is to the barrier.

Compared with a no barrier scenario, a barrier generally reduces downwind concentration. The amount of reduction is dependent on several factors such as wind speed, direction and atmospheric stability. As such, it is important to understand how these parameters affect concentration. These effects could be deduced with sufficient experimentation, but that is prohibitively expensive. With the CTAG model utilizing a LES turbulence model as described in this paper validated by experiment, however, a wide variety of numerical experiments can be performed to test various parametric effects. Ultimately, these simulations will prove useful in creating a parametric model which can be used to quickly and accurately inform roadway design communities of potential benefits of roadway barrier construction.

CHAPTER 3

EFFECTS OF ROADWAY CONFIGURATIONS ON NEAR-ROAD AIR QUALITY AND THE IMPLICATIONS ON ROADWAY DESIGNS

This paper presents an analysis of wind tunnel experiments of twelve different roadway configurations and modeling of these configurations using a Large-Eddy Simulation (LES) model, aiming at investigating how flow structures affect the impact of roadway features on near-road and on-road air quality. The presence of roadside barriers, elevated fill and depressed roadways, and combinations of these configurations all reduce ground-level air pollutant concentrations immediately downwind of roadways. However, all of these cases, except the elevated fill configuration, increase pollutant concentrations on the roadway itself. For a roadside barrier with finite length, higher concentrations than those without a barrier are present in a small region near the edge of the barrier, influenced by complex flow in that region which we term Edge Effects. The inclusion of multiple roadway features often result in lower downwind pollutant concentrations than those with single roadway features; however, adding features typically offers diminishing returns in concentration reduction. Generally, the effects on concentration, both beneficial and adverse will damp out within 15 multiples of the characteristic height, be it the barrier height or the elevation/depression height of the roadway. Thus, evaluating the trade-off between the air pollutant reductions near the ground and the air pollutant increases on the roadway and elevated above the ground will be important in designing a sustainable transportation system.

3.1 Introduction

Living and working near major roadways has been linked to increased risk of respiratory complications, cardiovascular disease, and other adverse health effects (HEI, 2010). While increasingly stringent tailpipe emission regulations have resulted in drastic reductions in the net amount of traffic-related emissions, the expansion of metropolitan areas and the rise in motor vehicle ownership have led to an increase in the number of people living, working and going to school near highways or other large roads. Therefore, there is a pressing need to develop additional mitigation strategies to protect public health besides those targeting reduced emissions from individual vehicles.

There are potential opportunities for mitigating near-road air pollution in roadway design options that affect pollutant transport and dispersion such as road configurations and the presence of roadside barriers (Baldauf et al., 2008, 2009; Wang and Zhang, 2009). To incorporate those options into actual design practices, a mechanistic understanding of the fate and transport of the traffic-related air pollutants is required but is currently lacking. The overall objective of this paper, along with our previous efforts (Wang and Zhang, 2009; Steffens et al., 2013, 2012; Tong et al., 2011), is to bridge this gap, and provide design guidance to urban, transportation and environmental planners.

Our general approach is to develop and apply numerical modeling tools to analyze and supplement existing experimental data. There are two major benefits to using this approach. While experiments provide essential empirical evidence, they do not directly reveal the underlying physical mechanisms, which can be studied by comparing modeling results against measurements; Experi-

ments are often costly and time intensive to cover a wide range of road, traffic and meteorological conditions, which can be investigated by a validated model based on fundamental principles. Several researchers applied this approach to study the effects of barriers on dispersion of pollutants near roadways. Steffens et al. (2012) studied the effects of a vegetation barrier on near-road particle size distributions, and Steffens et al. (2013) investigated the effects of a solid barrier on tracer dispersion under different atmospheric stability conditions. Similar approaches have been taken to study pollutant dispersion in street canyon environments (Chang and Meroney, 2003; Xie and Castro, 2009; Neophytou et al., 2011). Hagler et al. (2011) employed a $k - \varepsilon$ Reynolds-averaged Navier-Stokes (RANS) turbulence model to simulate two of the twelve configurations in the wind tunnel experiment described in Heist et al. (2009) that include a solid barrier, and investigated the sensitivity of simulated near-road air pollution to roadside barrier height, various wind directions, and secondary road emission. Steffens et al. (2013) showed that Large-Eddy Simulation (LES) turbulence model has a clear advantage over RANS in capturing the flow fields near barriers, especially in regions affected by flow recirculation.

In this paper, we apply our approach to simulate the wind tunnel experiment conducted by Heist et al. (2009), which characterized the 3-D concentration gradients of a tracer gas under twelve different roadway configurations, the most comprehensive to date. Here, we substantially advance the work by Hagler et al. (2011) by adopting an LES turbulence model, and comparing the modeling and experimental results for all twelve roadway configurations, providing a detailed evaluation for a wide variety of road design scenarios.

3.2 Methodology

3.2.1 Wind Tunnel Experiment

The U.S. Environmental Protection Agency (EPA) performed a wind tunnel experiment detailing the effects of various roadway configurations on the concentration of a tracer gas. The full description of the experiment and methodology employed can be found in the work of Heist et al. (2009). A brief description is presented here.

The experiment was performed using a meteorological wind tunnel (Snyder, 1979) located in the EPAs Fluid Modeling Facility. The wind tunnel test section measures 370 cm wide by 210 cm high by 1830 cm long. The inlet boundary layer profile was created by utilizing three Irwin spires (Irwin, 1981) and the floor downwind of the spires was covered in roughness blocks to maintain and condition the boundary layer to approximate a typical atmospheric boundary layer profile.

Twelve roadway configurations (see Table 3.1, Section 3.3.1) including depressed and elevated roadways and roadways with noise barriers were studied based on the prevalence of use along U.S. highways and feasibility for simulation in the wind tunnel. Each was constructed at a scale height of 1:150 of a typical 6 lane divided highway, with the lanes (traffic) running perpendicular to the flow in the tunnel. The right-handed coordinate system used to record and display the results had the origin placed in the center of the roadway with the positive x in the downwind direction, y lateral and z vertical. The roadway extended 18 m (full-scale) in both the $\pm x$ direction at ground level and

centered laterally in the tunnel. The distances in the study were normalized by a characteristic length, assumed to be the standard height of a solid roadside barrier of 6 m. This corresponds to a scaled model barrier height of 4 cm. Turbulence generated by the presence of roadway vehicles was simulated by placing a number of small blocks (6 x 6 x 12 mm) on the roadway. A near-neutrally buoyant tracer gas, ethane, was released from six lines along the roadway at a total emission rate of 1500 cc/min. Tracer concentrations were measured by six Rosemount Model 400A hydrocarbon analyzers. A 20 Hz Laser Doppler Velocimetrer (LDV) system was used to measure velocity at various points on, above, and downwind of the roadway.

3.2.2 Model Description

The Comprehensive Turbulent Aerosol Dynamics and Gas Chemistry (CTAG) model contains the functionality to resolve the flow field including turbulent reacting flows, aerosol dynamics, and gas chemistry. The modular design of the model allows us to decide which components of the model to run in order to maximize simulation run time efficiency. In this paper, the model will be used to solve the flow field (velocity and turbulence) as well as compute the tracer gas concentration. A full description of the models theoretical background and implementation is presented in our previous work (Steffens et al., 2013), which evaluated the model against a solid roadway barrier. A condensed description is presented here.

The CTAG model employs a commercial Computational Fluid Dynamics (CFD) software package, ANSYS Fluent (ANSYS, 2009) to compute the velocity

and turbulence flow fields. We choose to use a Large Eddy Simulation with the Smagorinsky-Lilly subgrid model to compute the turbulence field as we have previously found it to be superior to any of the often used Reynolds-Averaged Navier Stokes (RANS) turbulence models, such as the $k - \varepsilon$ model. RANS models have the advantage of relatively low computational cost. However, we find the additional accuracy gained by the use of an LES model to necessitate the increased computational time cost for this study. Steffens et al. (2013) details the formulations of both RANS and LES models.

The only major uncertainty in the simulations arises from representing the vehicle-induced turbulence (VIT). As mentioned earlier, a large number of blocks were placed on the roadway to generate turbulence to mimic traffic in the wind tunnel experiment. However, due to their small size and increased complexity, it is computationally prohibitive to include these features in the computational model. The strategy we took to minimize this uncertainty is described as follows. First, we estimate the turbulence kinetic energy (TKE) of VIT by varying its values to fit the measured concentrations for the baseline case, i.e., a roadway on a flat terrain without barriers (Case A). Then we apply the same TKE value to the rest eleven cases.

As different roadway features affect on-road wind patterns, the stationary blocks deployed in the wind tunnel experiment generate turbulence as a (weak) function of the wind speed. In other words, the VIT in the experiment will vary from case to case. Therefore, a constant on-road TKE value assumed in the numerical simulations does not exactly replicate the experimental conditions. However, we argue that the constant on-road TKE value better represent the real-world conditions since the VIT is generated primarily by the movement of

traffic along the roadway, which is a strong function of vehicle speed and is not sensitive to ambient wind speed (Wang and Zhang, 2009). One important implication is that the constant TKE value allows better comparison of on-road concentrations. We have performed sensitivity analyses for the level of VIT for all of the cases, and the results will be described in Section 3.3.1.

Computational domains were created for each of the 12 cases from the experiment. Since each case has a unique geometry, the size of the mesh is different for each case ranging from 1,020,096 elements (Case A) to 3,554,412 elements (Case F). The grids are more refined near the roadway and any solid obstacles. We have performed a mesh size sensitivity analysis on each of the meshes to ensure the results are independent of grid size.

Inlet boundary conditions must also be specified. In the wind tunnel experiment, measurements upwind of the roadway were used to fit the parameters in the standard logarithmic velocity profile given by Equation 3.1. The best fit boundary layer parameters were found to be $z_0 = 0.52cm$, $d = 5.4cm$ and $u^* = 0.3m/s$. In this equation, u^* is the friction velocity, κ is the von Krmn constant, d is the displacement height, and z_0 is the surface roughness height.

$$\frac{U}{u} = \frac{1}{\kappa} ln\left(\frac{z-d}{z_0}\right) \tag{3.1}$$

For generating inlet turbulence boundary conditions in the LES model, a vortex method based on the Spectral Synthesizer method is used (Kraichnan, 1970; Smirnov et al., 2001). This method uses given profiles of TKE and turbulent dissipation to create perturbations in the given inlet velocity. The inlet profiles for TKE and dissipation are given by Equation 3.2 and Equation 3.3, respectively

(Deaves and Harris, 1982; Richards and Hoxey, 1993).

$$TKE = \frac{1}{2}\frac{(u^*)^2}{\sqrt{C_\mu}} \tag{3.2}$$

$$\varepsilon = \frac{(u^*)^3}{\kappa z} \tag{3.3}$$

3.3 Results and Discussions

In this section, we first evaluate the capability of the CTAG model at capturing the concentrations observed in the experiment under the various roadway configurations. Then we analyze the effects of local concentration caused by the various roadway configurations. We present data collected from both the experiment and simulations where possible. However, experimental data is not available for every scenario of interest. For these cases, we rely on simulation data to make observations and form conclusions.

3.3.1 Model Performance

In order to justify use of the simulation to draw conclusions, we must first show that the model accurately represents the experimental data. Each of the twelve configurations from the wind tunnel experiment conducted by Heist et al. (2009) were simulated and the comparison of simulation results to measured data is presented in Figure 3.1, showing ground level concentration, and Figure 3.2, showing vertical profiles of concentration a short distance from the roadway.

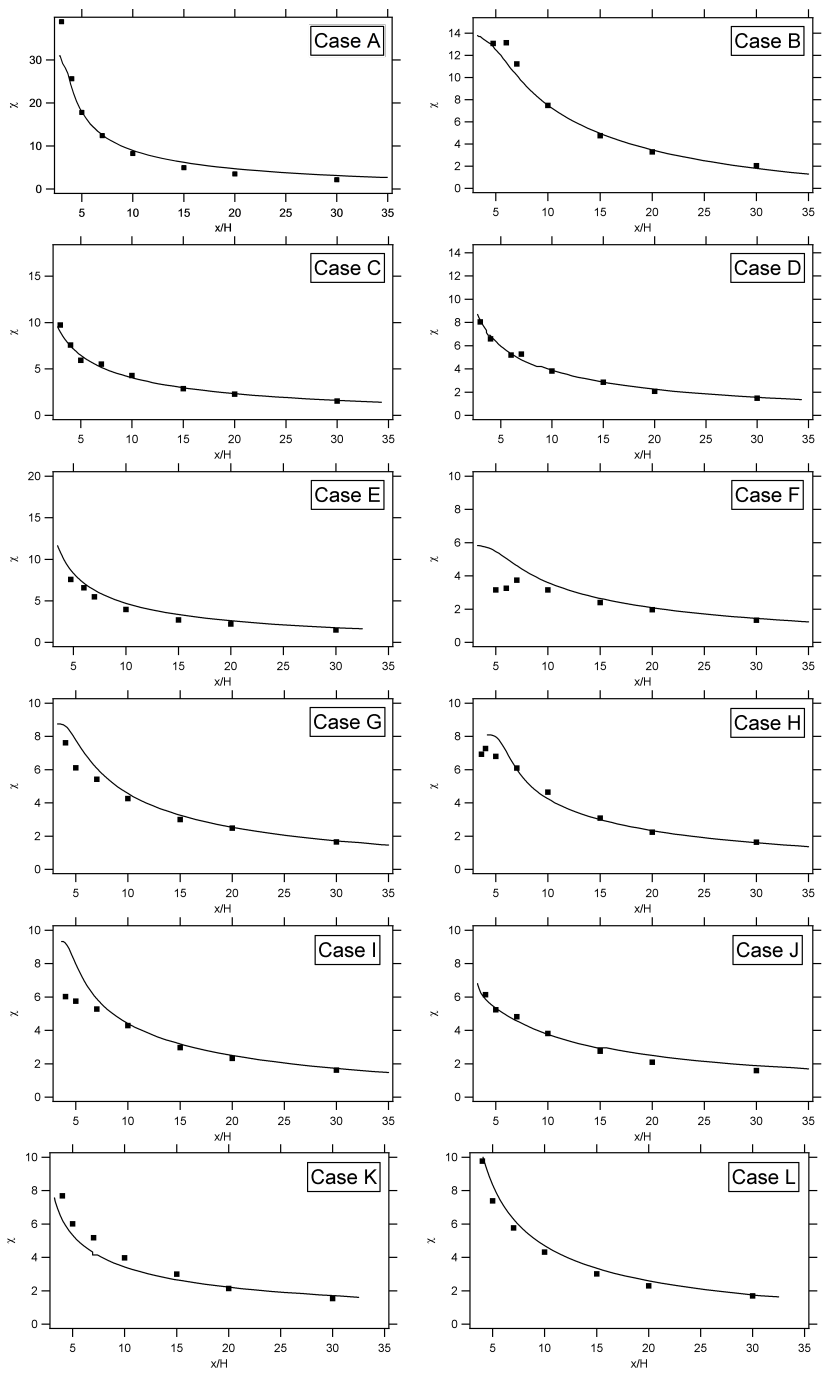

Figure 3.1: Normalized horizontal concentration comparison of Wind Tunnel experimental data (markers) to simulation results using the LES model (solid lines) at $z/H = 0$ (except for Case B compared at $z/H = 0.5$).

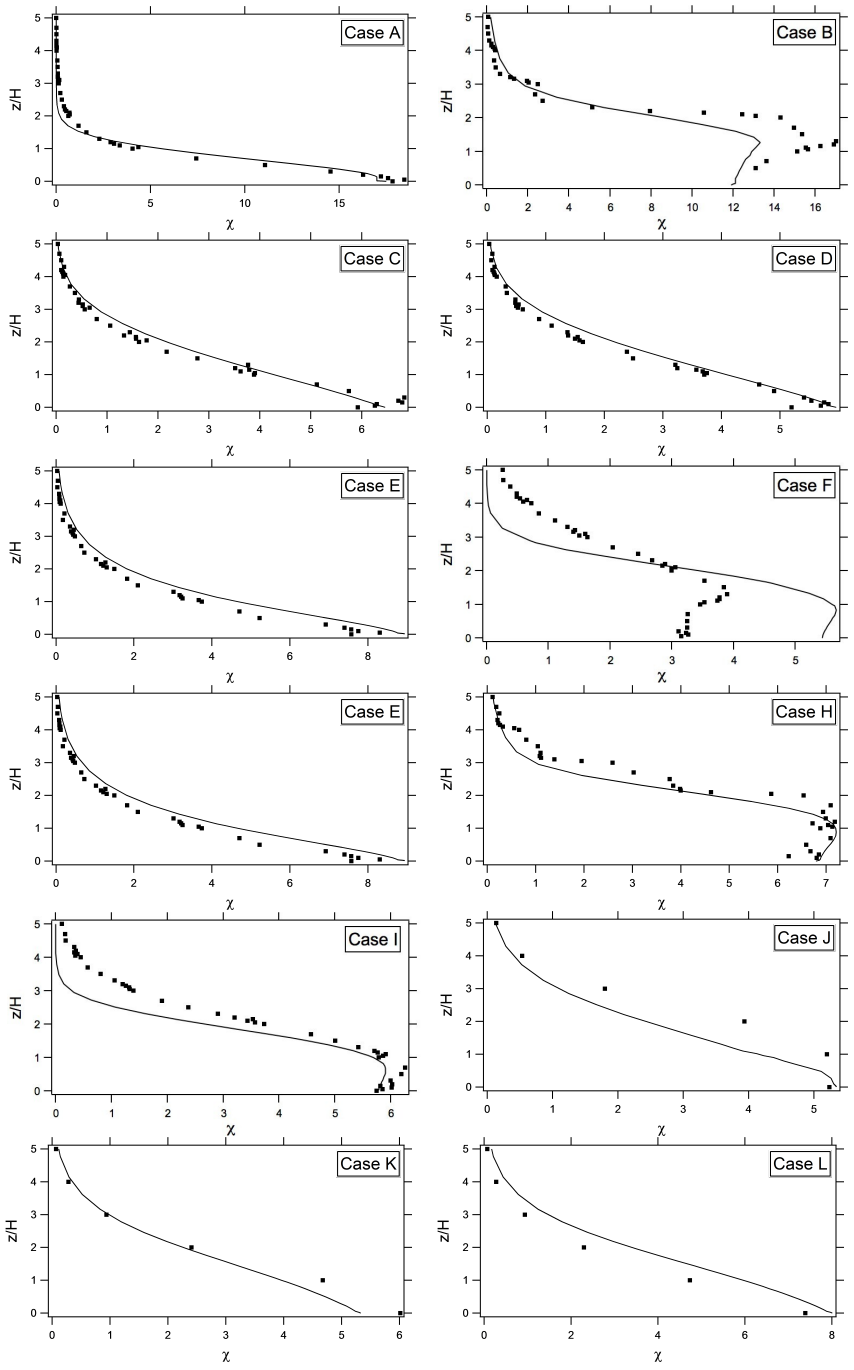

Figure 3.2: Normalized vertical concentration comparison of Wind Tunnel experimental data (markers) to simulation results using the LES model (solid lines) at $x/H = 5$ (except for Case B and Case E compared at $x/H = 4.75$ and Case F compared at $x/H = 5.25$).

Experimental uncertainty data were not available so only mean values are plotted. The case designations are those given in the wind tunnel experimental study. Table 3.1 gives a short summary of the configuration denoted by each ID letter in addition to the Normalized Mean Error (NME), a statistical measure of the overall deviations between the two sets of data as defined in Equation 3.4, between the data and the simulation results.

$$NME = \frac{\sum_{i=1}^{N} C_{1,i} - C_{2,i}}{\sum_{i=1}^{N} C_{1,i}} \tag{3.4}$$

where C_1 represents the simulated concentrations and C_2 the experimental measurements. Concentrations and distances in the experiment have been normalized in order to make appropriate comparisons between the scale model created in the wind tunnel and full scale, real-world scenarios. Distances have been normalized by the barrier height (6 m at full-scale for most cases). Concentration has been normalized according to the formula:

$$\chi = CU_r \Big/ \left(\frac{Q}{L_x L_y} \right) \tag{3.5}$$

where χ, is normalized concentration, C is the local mass fraction of tracer gas, U_r is a reference velocity (measured at full scale equivalent of 30 m), Q is the source strength, L_x and L_y are characteristic lengths of the roadway source region. The simulation geometry was built to the full-scale equivalent.

It is clear from Table 3.1, Figure 3.1 and Figure 3.2 that the model performs well in predicting the concentration profiles for most cases. The relatively high accuracy gives us confidence that the model can serve as a useful tool in in-

Table 3.1: Description of Case ID letters for the various roadway configurations with the Normalized Mean Error (NME) between the experimental data and simulation results, where H is the height of the feature as well as the scaling factor for evaluating the actual distance and elevation of modeled air quality effects; Fill angle is the angle from a line extending horizontal from the road surface down to the surface of the fill material; Cut angle is the angle from a line extending horizontal from the road surface up to the surface of the depression material.

Case ID	Description	Dimensions	NME
A	Level roadway and no barriers (base case)	H = 6 m*	0.090
B	Elevated roadway with solid fill underneath	H = 6 m Fill angle = 30	0.132
C	Depressed roadway, straight edges	H = 6 m Cut angle = 90	0.073
D	Deep depressed roadway, straight edges	H = 9 m Cut angle = 90	0.062
E	Depressed roadway, angled edges	H = 6 m Cut angle = 30	0.188
F	Depressed roadway with both upwind and downwind barriers	H = 6 m Cut angle = 30	0.403
G	Upwind barrier	H = 6 m	0.128
H	Downwind barrier	H = 6 m	0.058
I	Upwind and downwind barrier	H = 6 m	0.077
J	Tall upwind barrier	H = 9 m	0.147
K	Barrier at 1H upwind of roadway	H = 6 m	0.125
L	Barrier at 2H upwind of roadway	H = 6 m	0.157

*Value of H = 6 m is used as the scaling factor for comparative purposes.

vestigating the effects of other barrier configurations on local concentration that were not explicitly a part of the wind tunnel experiment.

The most notable deviation observed in the data comparison in Table 3.1 and Figure 3.1 and 3.2 is in Case F (depressed roadway with both upwind and downwind barriers adjacent to the road) occurring within a few barrier heights downwind of the barrier. Case F is a combination of both Case E (depressed roadway) and Case I (upwind and downwind barrier). Both Case E and Case I show reduced concentration behind the barrier, and the predicted results closely follow the measured values. In regards to the experimental data, Case F shows a reduction effect greater than either Case E or Case I. The simulation shows the right trend, but there is less reduction than observed in the experiment. One reason for the lower concentration in Case F is the possibility of greater lateral plume spread due to the location of the barriers being farther from the source than in Case I, thus allowing more time for the plume to develop laterally. Also, because of the addition of the depression in Case F, the recirculating region has more space to develop leading to a wider lateral spread. However, the model is not able to fully capture the more complex flow physics potentially exhibited here.

The other cases compare much more favorably, with only minor discrepancies, the largest of which are found in upwind barrier cases (Cases G, J, K, and L). These simulated cases all slightly, but systematically, underpredict the concentration immediately downwind of the barrier. Given that the constant TKE value for VIT is the only uncertainty in replicating the wind tunnel conditions, we have performed sensitivity analyses for the level of VIT for all of the cases. It is found that downwind concentration for Cases G, I, J and K, all of which have

upwind barriers and are more sensitive to on-road turbulence than other cases. Even though we were able to more accurately match the experimental results for those cases by fine-tuning the TKE values for those cases, we present and analyze the results (as shown in Table 3.1 and Figures 3.1 and 3.2) based on the constant TKE value for the reasons laid out in Section 3.2.2.

We also notice some deviation in the elevated roadway case (Case B) near the roadway. The vertical profile in Figure 3.2 shows lower concentration near the roadway height and a slightly larger concentrations vertically higher, indicating the simulation predicts a larger plume spread than was observed. These effects are damped out further from the roadway. The velocity measurements from the experiment show a small recirculation zone near the roadway that the simulation does not predict. We performed another simulation with an elevated roadway with a steeper fill angle (steep enough to cause a recirculation zone), and were able to more closely match the experimental results, suggesting that the presence of the recirculation zone has a significant impact on concentration.

3.3.2 Roadway Elevation/Depression

It is relatively common for major roadways in urban areas to be either elevated or depressed. As local flow structure has a significant impact on local concentration, it is important to first understand the impact of roadway elevation on the velocity field. Figure 3.3 shows four vector plots provided by the model for a level roadway, an elevated roadway with solid fill material underneath, a depressed roadway with straight edges and a depressed roadway with angled edges corresponding to Cases A, B, C, and E in the experiment, respectively.

The level roadway seen in Figure 3.3a shows a relatively unchanged velocity profile moving over the roadway. An elevated roadway (Figure 3.3b) acts to enhance vertical mixing as flow is deflected upwards over the roadway on the upwind side, which leads to the centerline of the plume located at about 1H vertically. As the plume expands downwind of the elevated roadway (Case B), the ground level concentration ($z = 0H$) becomes lower than that downwind of the level roadway without barrier (Case A). If the elevation is high enough or the incline is steep enough, a recirculation region may form downwind of the roadway, though one was not observed in the elevated roadway configuration in the simulation as the slope was gradual enough to allow the flow to expand. However, a small recirculation zone was observed in the experiment, which does impact our concentration results. Figure 3.3c and Figure 3.3d show a depressed roadway with straight edges and a depressed roadway with angled edges. These roadways are characterized by a low wind speed on and directly above the roadway.

Figure 3.4a shows the ground level ($z = 0$) concentration for the three cases. The elevated roadway shows a reduction in concentration compared with the level roadway case immediately downwind of the roadway (5-7 H) but the impact is quickly damped out. There seems to be little difference between the depressed roadway with straight edges or angled edges, but the concentration reduction for both is even larger than that of the elevated roadway. The increased residence time of the tracer over the depression (due to the reduced wind speeds) creates more on-road mixing than a level or elevated roadway, which facilitates mixing with the bulk flow. Furthermore, the decrease in concentration for the depression cases persists farther downwind than the elevated case, extending to approximately $15H$.

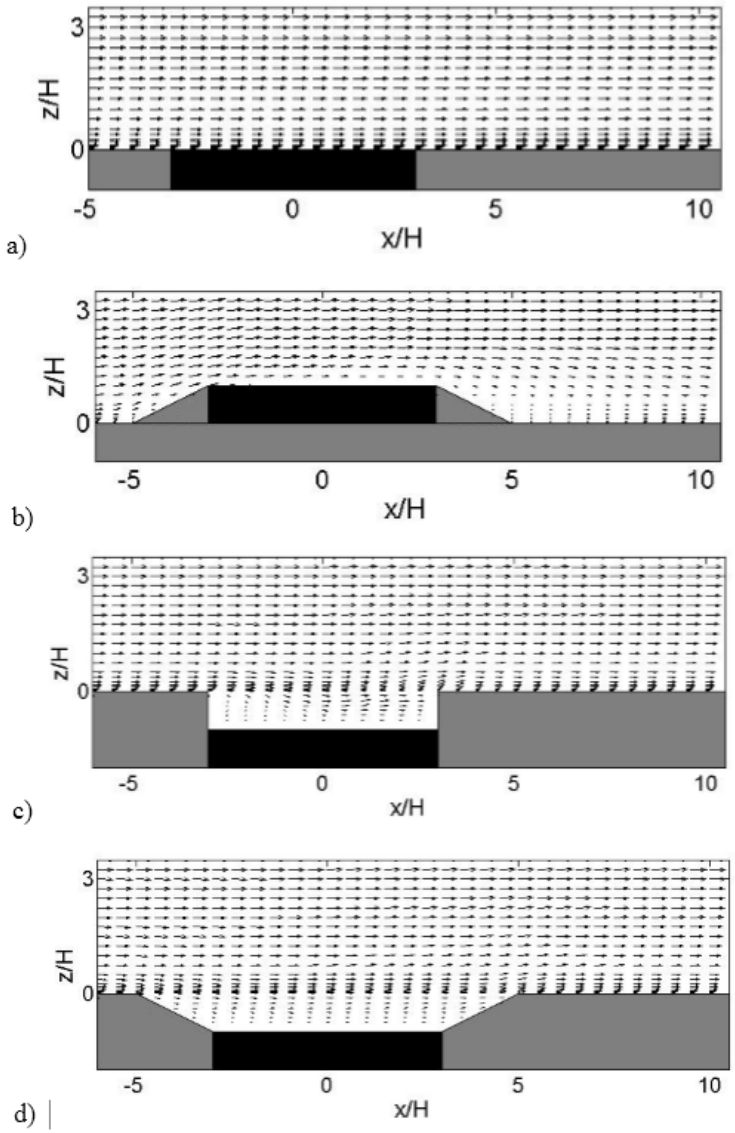

Figure 3.3: Velocity vectors for a) Case A (level), b) Case B (elevated), c Case C (depressed with straight edges), and d) Case E (depressed with angled edges). Origin is found in the center of the roadway at ground level, with the roadway extending from x/H = -3 to +3.

While the downwind concentrations are relatively similar, the on-road concentration can vary significantly. Figure 3.4b shows the on-road concentration for the various cases. The elevated roadway (Case B) has a generally lower

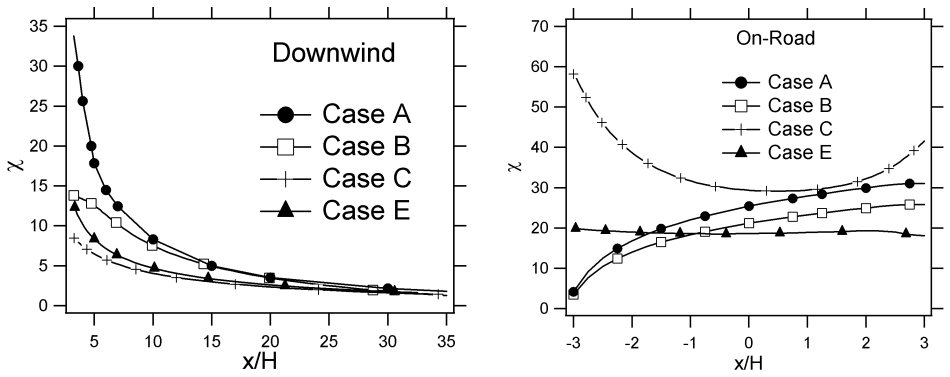

Figure 3.4: Comparison of ground-level (z=0) simulated concentration for Cases A (level), B (elevated), C (depressed with straight edges), and E (depressed with angled edges) for a) downwind, and b) on-road locations. Roadway extends from x/H = -3 to +3. Wind flow is from left to right in both figures.

on-road concentration compared with the level roadway (Case A). The depression with straight edges (Case C) shows a much greater on-road concentration, likely due to the extent to which pollutants become trapped in the road canyon. The depression with angled edges (Case E) shows similar concentration to the level roadway overall, despite the depression, due to the lack of recirculation trapping concentration on the roadway.

3.3.3 Barrier Location

The presence of an upwind or downwind barrier can significantly alter the local concentration both on and downwind of the roadway. Figure 3.5 shows velocity vectors for three cases: upwind barrier (Case G), downwind barrier (Case H), and both an upwind and downwind barrier (Case I). The no barrier (Case A) case is seen in Figure 3.3a.

For the no barrier case, there is relatively little change in vertical wind profile

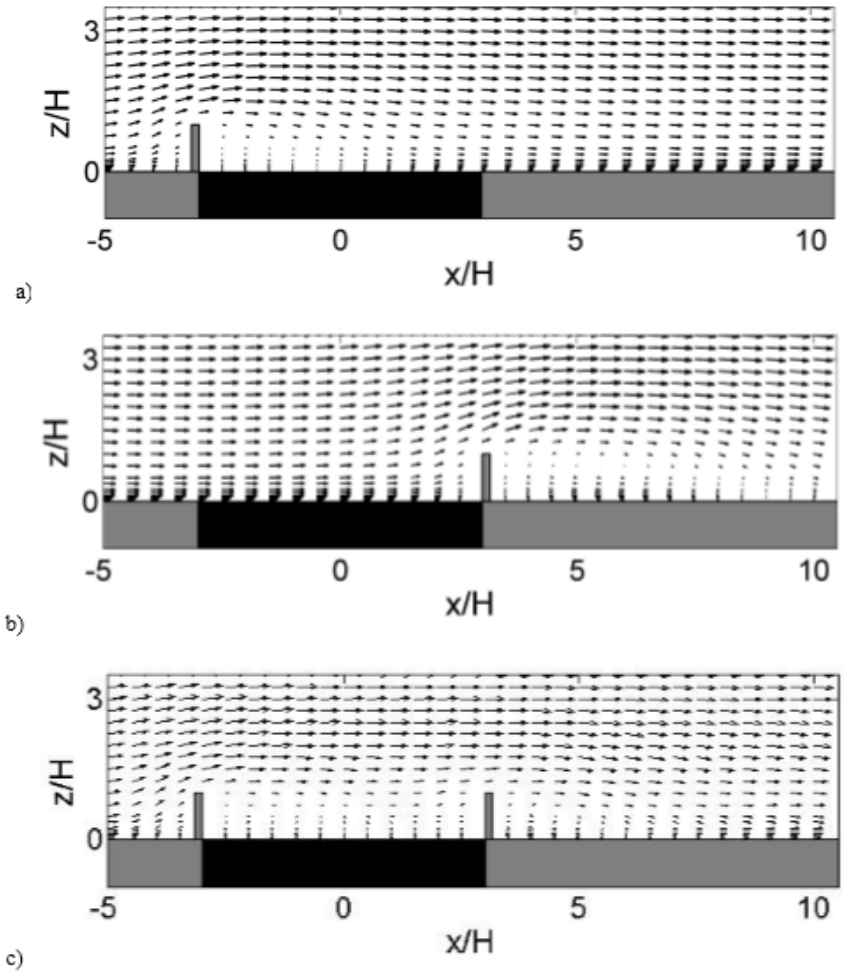

Figure 3.5: Velocity vectors for a) Case G (upwind barrier), b) Case H (downwind barrier), and c) Case I (both upwind and downwind barrier)

as the flow moves through the domain. The small changes that are observed are a result of the turbulence generated on the roadway. For the barrier cases, flow recirculation occurs due to the difference in pressure directly above the barrier and farther downwind. As flow moves up and over the barrier, it contracts, creating a high-pressure region. Farther downwind, the flow expansion reduces pressure. This difference in pressure causes the flow to recirculate back on itself. This phenomenon is clearly observed in Figure 3.5. Downwind of each of the

barriers a small recirculation region is formed. Within 10-12 H of the barrier, the vertical profile of velocity begins to return to the pre-barrier profile as the effects of the barrier are damped out.

Figure 3.6a shows the ground level concentration downwind of the roadway for the same four cases. It is clear that the presence of any barrier greatly improves air quality at the ground level as the barrier deflects the tracer over the solid structure, enhancing vertical mixing. Interestingly, the position of the barrier has only a small effect. For both the upwind and downwind barrier cases, the flow moves towards the barrier as it passes over the roadway (i.e. flow moves from the upwind side of the barrier for Case H and from the downwind side of the barrier in Case G as it approaches the barrier). Thus, in both cases, the flow travels towards the barrier before being deflected upward, causing a similar effect on the downwind concentration profile, as observed in Figure 3.5. (It should also be noted that the air concentration increases as the flow moves over the roadway, thus profiles of on-road concentration would tend to increase closer to (and on the roadside of) the barrier, be it upwind or downwind.) Cases K and L have a barrier further upwind of the roadway at 6m and 12m, respectively. Figure 3.1 shows that there is slightly less reduction in concentration for Cases K and L when compared to Case G, but both cases still show significant reduction in downwind ground-level concentrations compared to Case A. The presence of both an upwind and downwind barrier seems to offer a marginal increase in mitigation benefit downwind of the roadway and barrier over a single upwind or downwind barrier. Further discussion of this is found in Section 3.3.6.

Observing the horizontal profile of concentration at the barrier height ($1H$) in

Figure 3.6b, the barrier cases all have much higher concentrations than the no-barrier case, since the barrier acts to elevate the emission plume to the barrier height, which is of potential concern if there are multi-storied buildings near the roadway, leading to an increase in exposure due to the presence of the barrier. The elevated concentrations at $1H$ persist for about 7 to $15H$ downwind of the roadway.

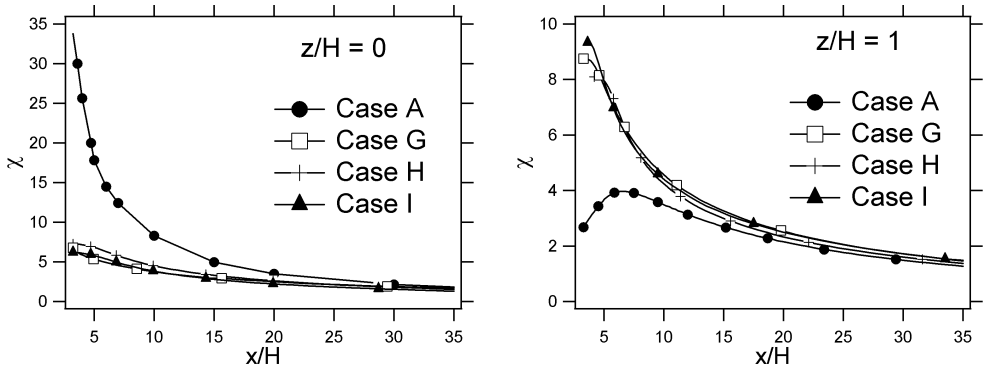

Figure 3.6: Simulated horizontal, downwind concentration gradients for Cases A (no barrier), G (upwind barrier), H (downwind barrier) and I (upwind and downwind barrier) at a) ground-level and b) one barrier height (1H) above ground.

Barriers also affect the on-road concentration. Average ground-level concentration was calculated for the four cases of A, G, H, and I. Figure 3.7 shows the profiles of on-road concentration for these cases. For the no barrier case (Case A), on-road concentration increases as flow moves over the roadway. The downwind barrier case (Case H) exhibits a similar behavior. Concentration increases similarly to the no barrier case until it approaches the barrier where the concentration then rises more rapidly. The upwind barrier case (Case G) behaves similarly to the downwind barrier, but as flow over the roadway is generally moving in the negative x direction, the trend is mirrored. Finally, for the upwind and downwind barrier case (Case I), concentration is highest near either barrier and lowest towards the middle of the roadway. The average ground-

level concentrations, for Cases A, G, H, and I were found to be 28.3, 37.5, 41.2, and 36.8, respectively.

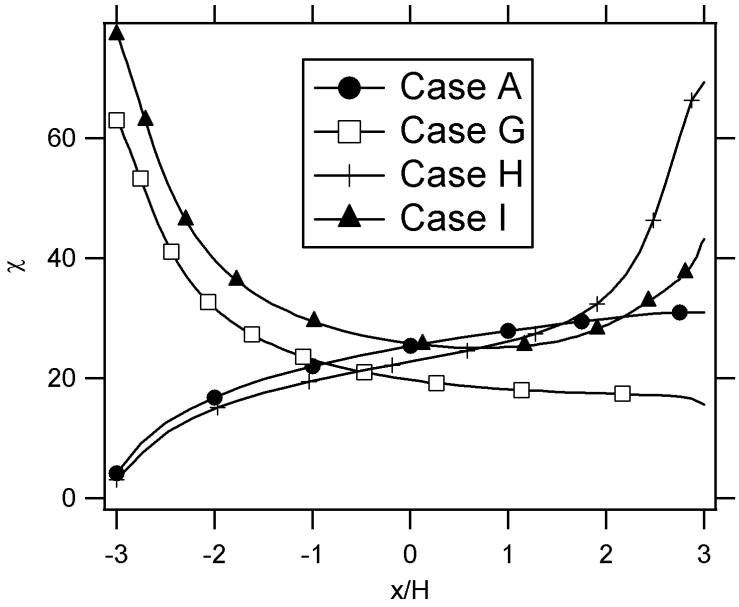

Figure 3.7: Horizontal ground-level gradients of on-road concentration from simulation data for Cases A (no barrier), G (upwind barrier), H (downwind barrier) and I (upwind and downwind barrier). General wind flow toward the road occurs from the left in this figure.

Overall, it is clear that the presence of a roadway barrier offers a significant reduction in concentration downwind of the roadway, but a significant increase in concentration on the roadway itself. For the barrier locations tested, the upwind/downwind location of the barrier has overall marginal impact on the concentrations. Having both an upwind and downwind barrier offers an added benefit over a single barrier. Nevertheless, it is small compared to the benefit of a single barrier over no barrier.

3.3.4 Barrier Height

Another interesting characteristic of barriers is the height. Simulations were performed using a downwind barrier of three different heights: 3 m, 6 m, and 9 m. Figure 3.8 shows vertical profiles of pollutant concentrations a horizontal distance of 1H downwind of the barrier in addition to a no barrier case for comparison. In the figure, the vertical axes are normalized to each barrier height, i.e. $1H$ for the 3 m barrier is at 3 m elevation, etc. The no barrier case was normalized with H=6 m, the average barrier height. The figure shows that behind the barriers, the vertical distribution of concentration is similar. For the no barrier case, the concentration is highest at the ground level and decreases steadily at higher elevations. Compared with the no barrier case, all three barriers show lower concentration at the ground level, and higher concentration above 0.5-1H in elevation. This is from the barriers lifting the tracer and enhancing vertical mixing.

Comparing the three barrier cases show that a larger barrier, normalized for barrier height, gives an overall lower concentration as it more effectively mixes the tracer gas. Smaller barriers also exhibit an increased plume spread relative to barrier height. This is due to the length and height of the virtual roadway not varying with respect to barrier height. It is also interesting to note the general shape of the three barrier profiles. Each profile shows a relatively uniform distribution below the barrier height, which suggests the mixing within the recirculation zone is strong. Above $1H$ however, all three profiles have a shape that one would expect for a simple elevated concentration source. That is, a symmetric parabolic curve. The maximum concentration for all three barrier heights occurs at about $1.5H$. This suggests that the concentration downwind

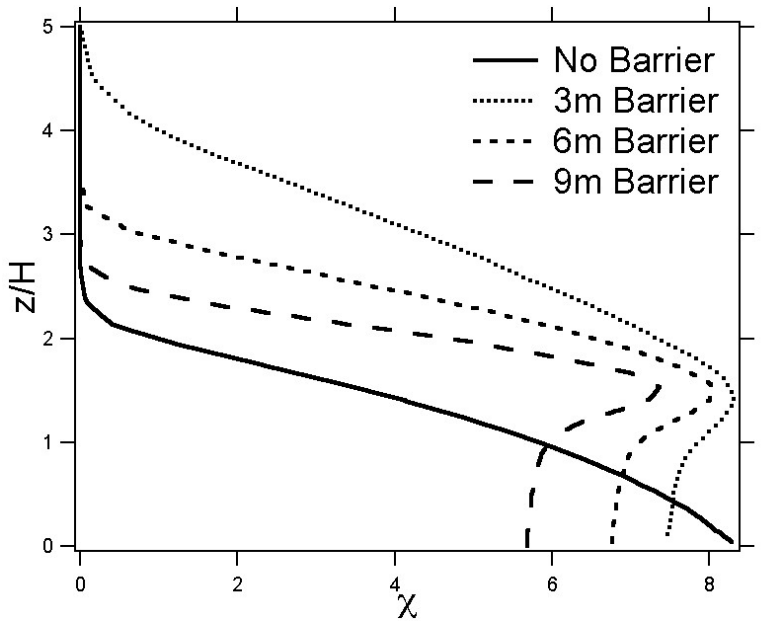

Figure 3.8: Vertical concentration profiles at a horizontal distance $1H$ downwind of a single barrier on the downwind side of the road. Profiles shown are for multiple barrier heights with concentrations normalized by barrier each height (no barrier case normalized by $H = 6m$)

of a barrier may be able to be modeled as an elevated source at $1.5H$ with a well-mixed zone below $1H$.

Figure 3.9 shows the on-road concentration for the multiple barrier heights and barrier configuration evaluated in Figure 3.8. It is clear that larger barriers lead to an increased concentration on the roadway as there is more flow deceleration and therefore longer on-road residence time.

3.3.5 Wind Speed

Simulations were performed for various wind speeds for both the no-barrier case and a single downwind barrier configuration. Three wind speeds were

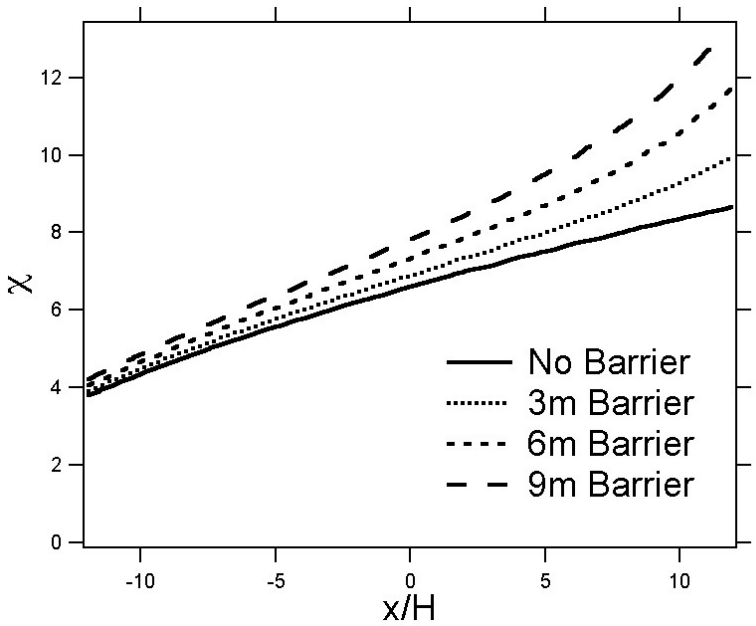

Figure 3.9: Horizontal on-road concentration profiles for single, downwind barriers of various heights. General wind flow is from left to right.

simulated. The nominal case uses the wind profile used in the wind tunnel experiment. The other two cases use the same profile scaled by a constant 0.5 and 2. Since concentration is normalized by wind speed, it stands to reason that changes in wind speed should have no significant impact on χ. Figure 3.10 shows a ratio of concentration for Case A (the no barrier case) to Case H (downwind barrier case) at the various wind speeds. Minor differences in concentration ratio are observed, which is explained by static on-road turbulence for all three conditions. This is in contrast to the results obtained in our previous work (Steffens et al., 2012) in which we observed the effects of particle deposition on a vegetative barrier under varying wind speeds. We found that smaller particles showed an increase in concentration relative to wind speed while larger particles showed a decrease in concentration. The reasoning being that size-dependent particle deposition rates do not scale linearly with wind

speed.

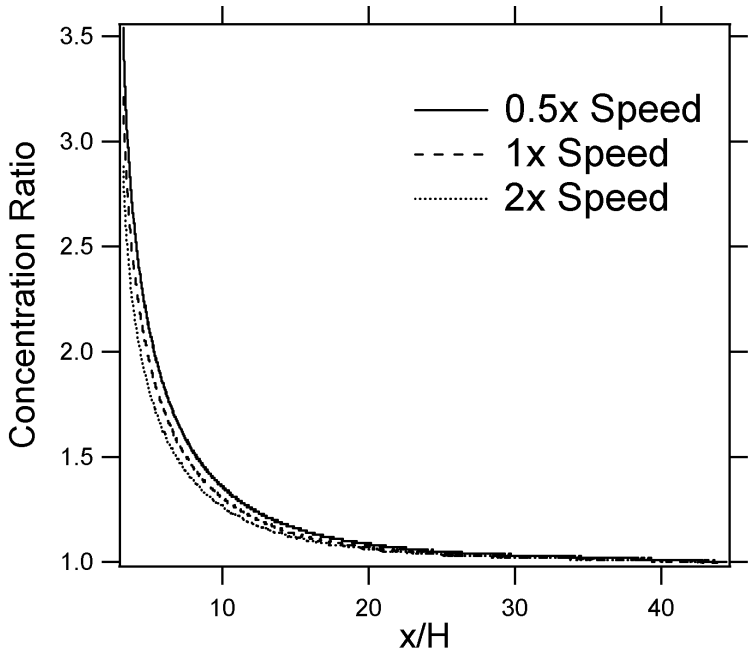

Figure 3.10: Reduction in ground level concentrations downwind of barrier under varying wind speeds. Concentration Ratio is defined as ratio of concentration for a no barrier case to barrier case.

We have performed simulations using no generated roadway turbulence that have shown the normalized concentrations to be essentially identical for varying wind speed. This was also observed in Heist et al. (2009) with the wind tunnel experimental data, where the turbulence induced by the small blocks was proportional to wind speed. In our simulations, an on-road turbulence independent of wind speed was chosen, which contributes to the minor differences in downwind concentration as seen in Figure 3.10. Since the on-road turbulence is mostly driven by moving traffic (Zhang and Wexler, 2004; Wang and Zhang, 2009), it is not a strong function of atmospheric conditions.

3.3.6 Additive Geometric Effects

It is also interesting to note the cases that are closely related or a combination of other cases. These cases highlight that the additional features from more complex roadway configurations have generally diminishing returns on effectiveness of air pollutant mitigation. For instance, Case C and D, seen in Figure 3.11a, both represent depressed roadways, 6 m and 9 m deep, respectively. And while the reduction for the level roadway to Case C is substantial, there is only a moderately greater reduction in Case D, despite being 50% deeper. The depression has the effect of trapping pollutants and creating a relatively well-mixed region. As the bulk flow moves over the depression the vertical profile remains relatively uniform as seen in Figure 3.3c (showing Case C). A recirculation zone is observed within the depression for both Case C and Case D, which creates some mixing. As the bulk flow moves over the depression, it will entrain some of this high concentration fluid, the result is that the bulk flow will increase in concentration, but at a lesser rate than if there was no depression, as much of the emissions are trapped on the roadway. For the deeper depression, there is a larger volume over which the emissions are spread, thus the plume entrained by the bulk flow is of slightly lower concentration in Case D than Case C. A similar effect is found when comparing Case G and Case J. Both are upwind barriers, but the barrier in Case J is 50% taller, resulting in a larger recirculation zone.

We showed in Section 3.3.3 that the additional benefit from both an upwind and a downwind barrier (Case I) was marginal over just a single barrier either upwind (Case G) or downwind (Case H). For the reasons discussed in Section 3.3.3, there is little difference between an upwind and a downwind barrier. The

presence of a second downwind recirculation zone does not change the fundamental flow physics. Observing the velocity vectors for Case I in Figure 3.5c, the flow is moving towards the upwind barrier as it recirculates over the roadway, increasing in concentration, similar to the velocity vectors for the downwind barrier case. It then reversed direction as it is entrained by the bulk flow. The bulk flow is deflected over the downwind barrier where it expands just as it does in the single downwind barrier case. Thus, there is a flow of similar concentration moving over an identical barrier, creating relatively little difference. The small improvement that is observed can be attributed to the longer residence time of the plume due to the second recirculation zone, increasing the amount of time for the plume to spread vertically.

Figure 3.11b shows ground level downwind concentration for configurations with various barrier heights. It is seen that taller barriers lead to lower concentrations, but the effect is not linear with barrier height. For example, the 6 m barrier configuration does not result in half of the concentration behind a 3 m barrier.

The only case with significant reduction from a combination of effects was Case F when compared with Cases E and I, as shown in Figure 3.11c. As discussed in Section 3.3.1, the barriers are located farther from the emission source in case F than Case I, creating more room for the plume to spread vertically. Note that despite other figures being presented showing simulated concentrations for the sake of a fair comparison, Figure 3.11c shows measured concentration from the experiment due to the inaccuracies of the simulation in capturing the concentrations in Case F.

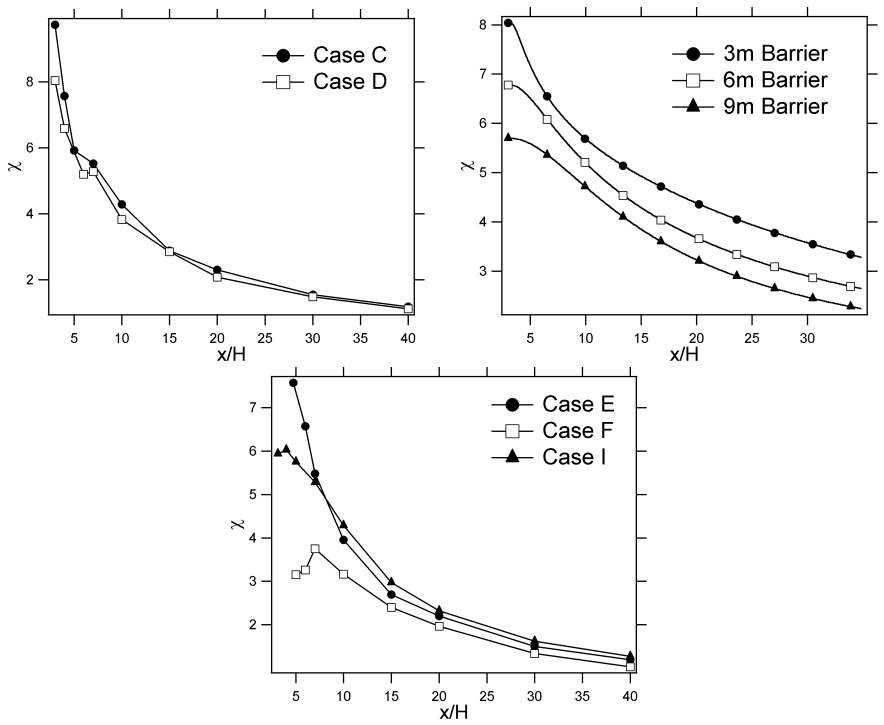

Figure 3.11: Comparison of concentration comparing a) Cases C (6m depression) and D (9m depression), b) Single downwind barriers of multiple heights; and c) Cases E (6m depression with angled edges), F (6m depression with angled edges and upwind and downwind 6m barriers), and I (no depression with upwind and downwind 6m barriers).

3.3.7 Edge Effects

The wind tunnel experiment simulated an infinitely long barrier. However, our previous work (Baldauf et al., 2008; Finn et al., 2010; Steffens et al., 2013) showed that near the edge of a barrier, the flow field behavior changes, which can have a significant effect on local concentration. It stands to reason that far away from the edge, the concentration profiles behave just as it would for an infinitely long barrier. From a design perspective, it is important to know how far these effects persist from the edge. We have performed simulations using the conditions from Case H of the wind tunnel experiment to create a finite barrier case in

order to make it comparable to the other cases from the experimental data. The created barrier is 500 m long with a height of 6 m.

Figure 3.12 shows the downwind ground-level profiles of concentration at various distances from the edge of the barrier, as well as the concentration profile for an infinitely long barrier compared with a case with no barrier. The highest concentrations occur with no barrier present, with the maximum concentration occurring slightly beyond the barrier, at about 10m from the edge. This is the result of the high concentration flow from the roadway moving around the barrier where a lateral recirculation zone forms. Farther away from the barrier, the overall concentration decreases. Since some of the tracer is diverted around the barrier, the flow moving up and over the barrier, away from the edge, is cleaner than that of an infinitely long barrier. We call this phenomenon the Edge Effects. However, the region of higher concentrations influenced by the Edge Effects is small, and further behind the finite barrier, a large concentration reduction similar to an infinite barrier is observed.

Farther from the edge of the barrier, we do observe the concentration profile behaving as it would with an infinitely long barrier. At 50 m from the edge, the maximum deviation from the infinite barrier is about 25%. At 150m from the edge, it is only about 10%. At 250 m from the edge, the difference is less than 1%. This suggests that for barriers longer than 500 m (since edge effects will manifest on both ends), at least part of the barrier can be treated under an infinitely long barrier assumption.

We have also performed simulations with the inlet velocity multiplied by a constant 0.5 and 2 to determine if these results are sensitive to changes in wind speed. The results show that the general trends are similar to those observed

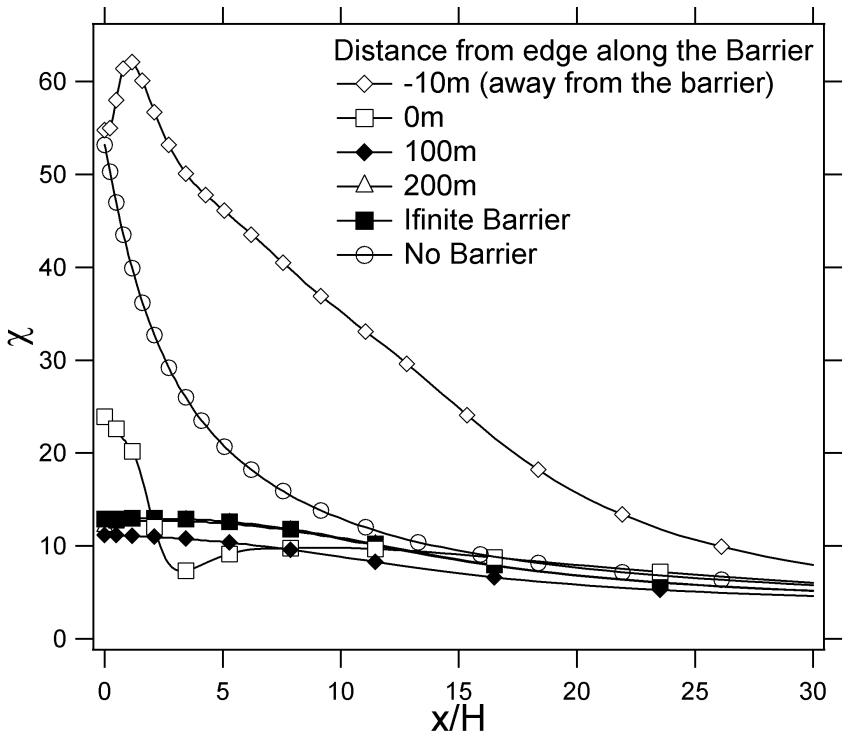

Figure 3.12: Ground-level concentration profiles perpendicular to the roadway at a given distance away from the edge of a single downwind barrier ($H = 6m$), both behind the barrier and away from the edge where no barrier is present (negative values indicate distance from the edge in the no barrier direction). These concentrations are compared with an infinitely long barrier case and a no barrier case.

in Figure 3.12. Halving the wind speed shows a slight decrease in the severity of the edge effects and how far they persist away from the edge. Doubling the wind speed has the opposite effect. However, these effects do not seem overly significant. For comparison, at 50 m from the edge, the maximum deviation in the half speed and double speed cases are 20% and 35%, respectively, as compared with the 25% observed in the nominal case.

3.4 Conclusion

The results of the wind tunnel experiments suggest, confirmed by our numerical simulations, that the near road structures (such as roadway elevation, depression, or solid barrier) impact the dispersion of pollutants near roadways and therefore can be considered as a potential mitigation option. For all roadway configurations studied in the wind tunnel experiment, concentrations downwind of the obstacle were found to be lower compared to a case without the obstacle. Our analysis combining the wind tunnel measurements and numerical simulations elucidates the flow structures for the different configurations, and results in a number of important implications for roadway designs and their air quality impacts.

An elevated roadway configuration with solid fill underneath is the only case that achieved a reduction in ground-level concentrations for both downwind of the roadway and on the roadway itself. However, this configuration had the lowest reductions in downwind concentrations for any of the configurations evaluated. In addition, there is an increase in concentration near the elevation height downwind of the barrier compared with a level highway.

Depressed roadways show significant ground-level concentration reductions compared with level roadways. However, on-road concentration is much higher for depressed roadways, and depressions with straight edges in particular have significantly higher on-road concentration of any of the configurations.

Solid barriers provide significant downwind ground-level concentration reduction, but with higher concentration on-road and near the barrier height elevation. The height of the barrier is important, as a higher barrier increases ver-

tical mixing and thus creates a lower downwind concentration and a higher on-road concentration. We find that the location of the barrier (upwind or downwind) has minor impact on these trends. This is also true of the overall on-road concentration, even though concentration tends to accumulate near the barrier, whether upwind or downwind of the road. We also find a slight additional reduction from adding both an upwind and downwind barrier, but with diminishing returns.

We also investigated the effect of a finite-length barrier on concentration, compared to the infinite-length barrier case and the no-barrier case. We find that higher concentrations generally occur for the no-barrier case, while the highest concentrations appear close to the edge where the finite-length barrier begins, highlighting the influence of the Edge Effects. These edge effects also influence reductions behind the barrier, with maximum reductions occurring closer to the center of the barrier (approximately 150 m from the edge). At distances approaching 250 m from the edge, the profile of concentration is comparable to the infinitely long barrier case.

Generally, the effects on downwind concentration will damp out relatively quickly. Within approximately 15 multiples of the characteristic height, be it the barrier height or the elevation difference of the roadway to the surrounding terrain, the difference from the no barrier case is less than 10%. For a typical barrier height of approximately 6 m, this equates to only 90 m from the roadway. Changes in on-road concentrations also generally depend on the characteristic height of the configuration of interest. Thus, the trade-off between the potentially beneficial effects downwind of the road at ground-level breathing heights with the potential adverse effects on the roadway and elevated from the ground

requires significant consideration when designing a roadway. Consideration must be given to surrounding land use and roadway activities. For example, drivers on the road may only be exposed to elevated on-road concentrations for short periods of time, while residents near the road experience much longer exposure times. However, if the roads are congested, then drivers exposures may be elevated due to the longer time on the road. In addition, if the surrounding land use includes multi-story dwellings, offices, or schools, exposures may also be higher for the varying configurations compared to level roads with no obstructions.

CHAPTER 4

EXPLORATION OF EFFECTS OF A VEGETATION BARRIER ON PARTICLE SIZE DISTRIBUTIONS IN A NEAR-ROAD ENVIRONMENT

Roadside vegetation barriers have been suggested as a potential mitigation strategy for near-road air pollution. However, there is still a lack of mechanistic understanding of how roadside barriers affect pollutant transport and transformation on and near roadways, especially under different meteorological conditions and barrier properties. In this study, we incorporated the representations of particle aerodynamics and deposition mechanisms into the Comprehensive Turbulent Aerosol Dynamics and Gas Chemistry (CTAG) model, and explored the effects of vegetation barriers on near-road particulate air pollution by comparing the simulation results against field measurements. The model shows generally adequate agreement with concentrations of particles larger than 50nm, but tends to overpredict concentrations of particles less than 50nm behind a vegetation barrier. Sensitivity tests were performed by comparing two different particle dry deposition models and varying the vegetation density and local meteorology. It was found that an increase in leaf area density (LAD) further reduces particle concentration, but the responses were non-linear. Increases in wind speed were shown to enhance particle impaction, but reduce particle diffusion, which result in reduction in concentration for particles larger than 50nm but have a minimal effect on particles smaller than 50nm. Further improvements in representing particle deposition and aerodynamics in near-road environments are needed to fully capture the complex effects of roadside vegetation barriers.

4.1 Introduction

Exposure to traffic related air pollutants has been linked to a wide variety of health concerns, including respiratory and cardiovascular problems, birth and developmental defects, and cancer (HEI, 2010). Given the enormous health and societal impacts resulting from near-road air pollution, it is critical to develop effective strategies to mitigate near-road air pollution. In addition to vehicle emissions control, there are potential opportunities for mitigating near-road air pollution in roadway design options that affect pollutant transport and dispersion such as road configurations and the presence of roadside barriers (Bowker et al., 2007; Baldauf et al., 2008, 2009; Cahill, 2010). Recent wind tunnel and field studies (Heist et al., 2009; Finn et al., 2010) have suggested that roadside barriers, such as sound walls and vegetation, may provide a cost effective strategy to mitigate near-road air pollution. However, there is still a lack of mechanistic understanding of how roadside barriers affect pollutant transport and transformation on and near roadways, especially under different meteorological conditions and barrier properties.

In this paper, we attempt to explore the effects of roadside vegetation barriers on transport of exhaust particles near roadways. The presence of vegetation barriers affects two major atmospheric processes governing the plume transport near roadways, i.e., turbulent mixing and dry deposition of atmospheric constituents. These two processes have been studied by separate communities. First, windbreak/shelterbelt and meteorological research communities have long focused on the aerodynamic aspects of vegetation barriers, i.e., how porous heterogeneous vegetative structures affect the wind field, microclimate and boundary layer meteorology (Cleugh, 1998; Wilson, 2004a,b; San-

tiago et al., 2007). Second, the deposition of gaseous and particulate species on vegetation canopies has been an active research area in aerosol science, and several deposition models have been proposed and implemented in multi-scale air quality and ecological models. There are only few modeling studies so far which have investigated how the vegetation affects plume transport. However, they did not consider pollutant deposition (Bouvet et al., 2007; Buccolieri et al., 2009; Gromke and Ruck, 2007; Gromke et al., 2008; Raupach et al., 2001).

In this paper, we expand the capability of the Comprehensive Turbulent Aerosol Dynamics and Gas Chemistry (CTAG) model to characterize the aerodynamic and deposition effects of roadside vegetation barriers. The focus of this paper will be to evaluate the model performance against experimental results from a recent field measurement conducted in Chapel Hill, NC. This study marks the first time to combine the effects of aerodynamics, deposition and plume transport into a single model, constrained by experimental data. While aerodynamic vegetation models have been developed for use in local environments, vegetation deposition models are typically developed for larger forest canopies and for use in large-scale regional models. While not conclusive, the simulation results will give insight into the performance of the deposition models of Zhang et al. (2001) and Petroff and Zhang (2010) at the local level. In addition, sensitivity analyses will be performed to predict how the near-road air quality will respond to changes in parameters such as modeling geometry, upwind meteorological conditions and canopy leaf area density.

4.2 Theoretical Basis

Understanding the behavior of particles suspended in a turbulent flow is crucial for developing models to predict concentration and deposition as it pertains to vegetation. Here, we discuss the important particle and flow parameters which characterize the interaction between particulate and surrounding fluid. Relating these parameters to each other allows for the creation of non-dimensional properties, such as Reynolds number and Stokes number, which are highly useful in comparing similar flows.

4.2.1 Stokes Flow

Spherical particles are essentially defined by their diameter, D_p, and their density, ρ_p (or mass, m_p). Particles suspended in a fluid will experience a force imparted by the fluids viscosity. The relative importance of the particle's inertia and the fluid's viscosity is given by the particle Reynolds number, Re_p, which is defined as:

$$Re_p = \frac{\rho D_p U}{\mu} \tag{4.1}$$

where ρ is the fluid density, μ is the fluid viscosity, and U is the relative velocity between the fluid and particle. The motion of very small particles, i.e. particles with small Reynolds numbers ($Re_p \ll 1$), such as we study in this paper, will be completely dominated by viscous effects. These types of flows are generally called Stokes flows or creeping flows. Under the assumption of very small Reynolds number, inertial effects in the Navier-Stokes equations can be ignored,

and a drag force experienced by the particle can be derived. Stokes law is the expression which defines this drag force and is given by:

$$F_D = 3\pi\mu D_p U \tag{4.2}$$

The majority of particles in typical atmospheric flows are less than $20\mu m$ (Seinfeld and Pandis, 2012, p.406) and Stokes law is generally appropriate. However, for the particles at the larger sizes or in faster motion, Re_p may begin to exceed unity. At these higher Reynolds numbers, inertial terms become more significant and Stokes law becomes less appropriate. To account for this, the drag force is rewritten to include a drag coefficient, C_D, which is a function of Reynolds number and evaluated empirically. Thus, drag force becomes:

$$F_D = \frac{1}{8}\pi C_D \rho D_p^2 u^2 \tag{4.3}$$

Numerous empirical fits have been proposed by researchers such as Flemmer and Banks (1986); Massey et al. (1989); Morrison (2013); Perry et al. (1999) just to name a few. For one example, Perry et al. (1999) defines the drag coefficient as:

$$C_D = \begin{cases} \frac{24}{Re_p}, & Re_p \leq 0.3 \\ 18.5 Re_p^{-0.6}, & 0.3 \leq Re_p \leq 1000 \\ 0.44, & 1000 \leq Re_p \leq 200000 \end{cases} \tag{4.4}$$

In this formulation, and indeed all formulations, Equation 4.3 reduced to Equation 4.2 for very small Reynolds number.

4.2.2 Characteristic Time Scales and Stokes Number

One very important characteristic of particle motion is the characteristic particle time scale. The viscous drag imparted on the particle will cause it to tend towards the motions in the flow, but the particle will need time to respond. Consider a particle moving with some initial velocity in a quiescent fluid. The equation which describes the motion of the slowing particle is an exponential decay with some time constant, τ_p, given by:

$$\tau_p = \frac{\rho_p D_p^2}{18\mu} \tag{4.5}$$

This definition is the typically used for the characteristic particle time scale.

It would be useful to compare the response time of the particle to some characteristic time of the flow to determine the overall impact of flow motion on the particle. Because turbulence is an inherently multiscale phenomenon, there are multiple potential ways to define the characteristic time scale of the fluid. It makes sense, then, to define two time scales based on the largest scales of turbulent eddies and the smallest, or Kolmogorov, scales. Thus we can define the large eddy turnover time, τ_L, and the Kolmogorov timescale, τ_η, as:

$$\tau_L = \frac{L}{u} \tag{4.6}$$

$$\tau_\eta = \left(\frac{\nu}{\varepsilon}\right)^{1/2} \tag{4.7}$$

where u is the characteristic flow time, L is the large eddy length, ν is the fluid

kinematic viscosity, and ε is the average dissipation rate of the turbulent kinetic energy. For shear flows, such as atmospheric flow, it is also convenient to define a viscous time scale, τ_F, based on the flow friction velocity, $u*$, as it is a commonly measured parameter, particularly in atmospheric dispersion modeling. This time scale is define as:

$$\tau_F = \frac{\nu}{u*^2} \tag{4.8}$$

The Stokes Number, St, is a dimensionless quantity generally defined as a ratio of the particle response time to the characteristic time of the flow in which it is suspended. By comparing the relative time scales of the particles and fluid, the Stokes number gives an indication of the sensitivity of particle motion to the flow. Specifically for turbulent flow, if the Stokes number based on the Kolmogorov time scale, $St_\eta = \tau_p/\tau_\eta$, is very small ($St_\eta \ll 1$), the particle responds very quickly to even the smallest velocity fluctuations and can be treated as a passive scalar. If the Stokes number based on the integral time scale, $St_L = \tau_p/\tau_L$, is very large ($St_L \gg 1$), then the particle is generally not influenced by even the largest scales of turbulent motion (Tanire et al., 1997).

At intermediate size ($St \sim 1$), particles may be trapped and then expelled from the vortex structure of the turbulence (Yule, 1980). Because of this, particle concentration is generally not uniform in a turbulent flow. A centrifugal effect from the rotation of the eddies causes particles to tend towards regions of low vorticity and high strain, in a process known as preferential concentration or clustering (Chen et al., 2006; Sundaram and Collins, 1997). Because particles tend to group more closely, an increase in the number of particle collisions is observed. This effect is most strongly observed in particles with intermediate

Stokes numbers as very small particles tend to conform to the random fluctuations of the velocity field and very large particles tend to ignore the turbulent fluctuations.

The Stokes number also has important implications for particle concentration and deposition. At large Stokes numbers, particles respond slowly to changes in flow direction. Because of this, in regions where the flow field is diverted away from obstacles in the flow, high particle inertia may prevent the particle from similarly changing course and lead to a collision with the object (Lapple and Shepherd, 1940; May and Clifford, 1967; Michael and Norey, 1969). Of particular interest to this work, this includes the impaction of large particles on vegetation canopies (Aylor, 1975; Legg and Powell, 1979; Petroff et al., 2009; Slinn, 1982; Zhang et al., 2001).

Additionally, heavier particles have increased gravitational settling due to their higher mass, which further enhances deposition to a surface layer or vegetative canopy (Guha, 2008; Petroff et al., 2009; Zhang et al., 2001). However, the actual effect can be somewhat complicated as gravitational settling in a turbulent field is not the same as settling in a still fluid (Maxey, 1987). Nielsen (1993) notes that particles settling through turbulence are subject to the rotational motions in the flow. Some particles, such as bubbles, can be trapped within the turbulent vortices, preventing setting altogether. Conversely, small and heavy particles which are forced to the outside of the vortices may be 'fast-tracked,' significantly enhancing their settling velocity.

4.2.3 Mass Fraction

So far, we have only discussed the impact of the carrier fluid on the particles. However, it is possible for the particles to influence the flow. For example, particles with high Reynolds number tend to enhance turbulence due to vortex shedding (Kenning and Crowe, 1997). However, the overall effect of particles on the flow field can be neglected if the particles are sufficiently dilute (Rudinger, 1965). This is often expressed in terms of the ratio of particle mass to fluid mass called the mass fraction (m_p/m_f). Unfortunately there is still a lack of understanding of the underlying mechanisms which govern the effect of mass fraction and other parameters on the turbulence and there does not seem to be a consensus on the conditions under which particle influence can be neglected (Vaillancourt and Yau, 2000).

4.2.4 Implications for Current Study

In the Chapel Hill vegetation barrier experiment, ultrane particle (UFP) size distributions were obtained capturing 88 size channels ranging from 12.6 to 289 nm. Unfortunately, detailed turbulence statistics are not available for this field experiment. However, measurements from the nearby Raleigh-Durham International airport (RDU), estimate friction velocity. Using that data we will assume $u* = 0.197ms^{-1}$. From this and an estimated average particle density of 1500 kgm^{-3} (Hagler et al., 2012), we estimate the Stokes number based on the friction velocity, St_F, for the largest particles observed in this study (289nm) to be $1.9x10^{-3}$. Therefore, since the largest Stokes number is very small, it is safe to assume all of the particles behave as a passive scalar and we can neglect inertial

forces. We admit that there is significant uncertainty in this approximation. The choice of friction velocity is not local to the site, and there may be influences from the upwind vegetation canopy as our simulations show that the flow field has not fully recovered at the sampling location. However, the Stokes number is sufficiently small that we still feel comfortable making the assumption of Stokes flow.

Particle number concentrations measured in the experiment are on the order of 10000 to 50000 particle per cubic centimeter. However, given the nanoscale size ranges of these particles, the mass fraction is essentially zero. Thus we can safely assume the particles have no impact on the flow field. This justifies our decision to de-couple the particle simulation from the flow simulation.

4.3 Model Description

CTAG is an environmental turbulent reacting flow model, designed to simulate transport and transformation of multiple air pollutants in complex environments, e.g., from emission sources to ambient background. CTAG has been applied to a wide variety of urban environments ranging from on-road modeling to simulation of several square kilometers (Tong et al., 2011; Wang and Zhang, 2009; Wang et al., 2011). Next, we will describe how we implement the effects of vegetation barriers based on the CTAG framework.

4.3.1 Eulerian-Lagrangian framework

We adopt an Eulerian framework in order to simulate the flow field, and utilize a Lagrangian framework to simulate the motion of particles within the flow field. The aerosol dynamics model consists of several components: advective transport, deposition, and coagulation. Additional aerosol processes, such as evaporation and condensation, were not modeled in this study. It is assumed that the residence time in the domain, which is estimated to be less than 10 seconds for the modeling scenarios presented in the paper, is too short for these processes to have any significant impact on the results.

Advective transport is processed by the Discrete Phase Model (DPM), which computes a force balance on a representative number of fluid particles and tracking them as they move through the domain (ANSYS, 2009). Each tracked particle actually represents a large number of physical particles. The ratio of tracked particles to physical particles is referred to as the particle strength. The particle size distributions are divided into discrete size bins. In this study, we chose 9 size bins, evenly spaced in the logarithm scale. Within the Lagrangian framework, each tracked particle is assumed to be a self-contained representation of the entire particle distribution. That is, each tracked particle will have its own size distribution profile which updates at each time step of the simulation.

After the particles have been tracked throughout the entire simulation domain, local concentrations are calculated by averaging the concentrations of the tracked particles that pass through a given area (ANSYS, 2009).

4.3.2 Aerodynamic Model

We employ ANSYS Fluent commercial software package (ANSYS, 2009) as the turbulence solver. The flow field is resolved by iteratively solving the mass conservation equation and the Reynolds Averaged Navier-Stokes (RANS) equations. The turbulence field is computed using a realizable $k-\varepsilon$ model (Jones and Launder, 1972), which uses two equations to solve the turbulent kinetic energy, k, and the turbulent dissipation rate, ε.

Spatial averaging

Vegetation consists of numerous small leaf and branch structures that cause drag to impede the motion of incoming wind, which in turn significantly influences the turbulence characteristics of the flow. This highly complex structure found within plant canopies makes it impossible to completely resolve every physical element in a computational model due to the prohibitively large computation power this would require. In order to overcome this challenge, the vegetation is spatially averaged in order to produce average wind speed and turbulence statistics within the canopy (Wang et al., 2001; Wilson and Shaw, 1977). The canopy, which in reality exists as both fluid and solid material, is represented by a region of fluid only. The solid components of the canopy are not physically modeled. The effects of the solid matter manifest as source and sink terms to the prognostic equations. By using this method, the effects of the solid elements of the canopy can be modeled without having to physically resolve them. If the model is perfectly accurate, the velocity and turbulence statistics of each cell in the simulation will be the average over that same volume in the physical system. Recently, Endalew et al. (2009) proposed a hybrid model that

represents the trunk and largest branches as solid and only spatially averages the smaller branches and leaf elements. However, the hybrid method requires explicit knowledge of canopy geometry such as trunk size and branch number and location, which is unavailable for this study.

Windbreak effects

The vegetation imposes a drag on the air moving through the leaves and branches. This flow obstruction causes some air to move up and around the canopy, thus increasing vertical mixing (Cahill, 2010). In addition, this drag creates a windbreak effect behind the barrier which is characterized by lower wind speed and lower turbulence in the wake of the canopy (Cleugh, 1998; Santiago et al., 2007; Wang et al., 2001; Wilson, 2004a,b). Since the windbreak effect decreases wind speed downwind of the barrier, it decreases the rate at which traffic-related pollutants can be advectively transported away. While not typical, one study did observe an increase in NO2 concentrations downwind of a barrier (Maerschalck et al., 2008).

The momentum drag due to vegetation is proportional to the plant coefficient of drag, C_d (dependent on the tree type) and the leaf area density, LAD (ratio of leaf surface area to total volume occupied by vegetative element). Thom (1972) gives the modeled sink term, S_u, to be:

$$S_u = -\rho C_D LAD u^2 \tag{4.9}$$

As air moves through the canopy, small leaf and stem elements disturb the mean flow and convert kinetic energy to turbulent kinetic energy. However,

this turbulence is rapidly dissipated. Thus, within the canopy, turbulence may be high but there is a low turbulent regime behind the canopy (Kaimal and Finnigan, 1994). Thus, TKE is modeled as a combination of a source term representing the creation of TKE, and a sink term relating to the rapid dissipation of eddies.

The model formulation to describe the windbreak effect is dependent on the turbulence solver being employed. For example, if using the $k-\varepsilon$ turbulence solver, source and sink terms must be added to both the turbulent kinetic energy equation and the turbulent dissipation equation. There has been significant research into this closure problem for turbulence in plant canopies and several models have been developed (Greens et al., 1995; Hiraoka and Ohashi, 2008). The second order $k-\varepsilon$ model created by Greens et al. (1995) is used in this paper and is given by:

$$S_k = -\rho C_D LAD\left(\beta_p u^3 - \beta_d u k\right) \tag{4.10}$$

where β_p is the fraction of mean flow converted to turbulent kinetic energy and β_d is fraction of turbulent kinetic energy dissipated within the canopy (Greens et al., 1995). Liu et al. (1996) used dimensional analysis to create a model for the dissipation rate source term which shows good agreement with wind tunnel data, given by:

$$S_\varepsilon = -\rho C_D LAD\left(C_{\varepsilon 4}\beta_p \frac{\varepsilon}{k} u^3 - C_{\varepsilon 5}\beta_d u \varepsilon\right) \tag{4.11}$$

$$\beta_d = C_\mu^{1/2} \left(\frac{2}{\alpha}\right)^{2/3} \beta_p + 3/\sigma_k \tag{4.12}$$

$$\alpha = \frac{1}{2} C_D LAD C_\mu^{3/4} k^{2/3} / \varepsilon \tag{4.13}$$

where $\beta_p = 1$ if one assumes a dense canopy (Walklate et al., 1996), and $C_{\varepsilon 4}$, $C_{\varepsilon 5}$, C_μ and σ_k are constants defined in the $k - \varepsilon$ model.

4.3.3 Lagrangian Aerosol Dynamics Model

Particle Aerodynamics

Particle transport is determined by the drag force enacted on the particle from the bulk flow in addition to gravitational settling. Normally, Brownian motion is considered for sub-micrometer particles. However, for turbulent flows, turbulent diffusion, due to random particle movement caused by turbulent eddies is much greater than that from Brownian motion. Therefore all random motion is modeled as a Discrete Random Walk Model (ANSYS, 2009) which works by adding a random velocity perturbation to the average velocity.

Dry Deposition

It is assumed that when a particle is intercepted by a solid surface, it is deposited and removed from the air flow. However, due to the spatial averaging described in Section 4.2.2, which removes physical surfaces from the modeled canopy, a statistical dry deposition model must be used. A number of dry deposition

models of atmospheric particles have been proposed and implemented in multi-scale air quality and ecological models by calculating a deposition velocity, v_d (Davidson et al., 1982; Petroff et al., 2009; Petroff and Zhang, 2010; Piskunov, 2009; Shimeta and Jumars, 1991; Slinn, 1982; Zhang et al., 2001, 2009) In our study, we have implemented the dry deposition models proposed by Zhang et al. (2001) and Petroff and Zhang (2010), which show good agreement with field measurements.

The actual change in the particle concentration, C, is dependent not only on the deposition velocity but also on the density of the vegetation and the concentration itself. The following equation is used to compute deposition rate:

$$\frac{\partial C}{\partial t} = -LADv_dC \tag{4.14}$$

Equation 4.14 applies to both particle number and mass concentrations. As we model particle size distributions as discrete size bins, Equation 4.14 is used to update the particle strength for each bin by assuming the percent change in tracked particle strength is equal to the percent change in particle concentration.

Coagulation

Coagulation occurs when two distinct particles collide to form a single, larger particle. We adopt a semi-implicit modeling scheme to simulate coagulation described by Jacobson (2005).

4.4 Measurement Data

The detailed description of the field measurements to characterize the effects of solid and vegetative barriers on near-road air quality in North Carolina was provided by Hagler et al. (2011). A brief summary is presented here. Stationary air quality monitoring was performed at vertical heights of 3m and 7m behind the barrier and 3m away from the barrier. The coordinates of the measurement sites behind the barrier and away from the barrier are 35.914469,-79.026081 and 35.911403, -79.026217 respectively. The vegetative barrier consisted of a mix of pine and cedar tree. Wind speed and direction measurements were collected using a 3-D ultrasonic anemometer with sampling frequency 1 Hz. Ultrafine particle (UFP) size distributions were obtained using a scanning mobility particle sizer (SMPS), which captured 88 size channels ranging from 12.6 to 289 nm with a sampling frequency of 120 seconds. In addition, a mobile sampling vehicle measured UFPs while driving on a route, including background areas far from the roadway, using a fast mobility particle sizer (FMPS). Refer to Hagler et al. (2011) for detailed instrumentation information. In addition to performing the field sampling at different roadside locations, instrument intercomparison was frequently performed by co-locating the particle instruments for approximately 30 minutes of time. The measurements shown in this paper were from a single morning sampling session in Chapel Hill, NC along state route 15-50l on November 23, 2008. The site can be seen from satellite view obtained from a Google Maps image in Figure 4.1. This site had an approximately 6 to 8 m tall stand of conifer trees located adjacent to the route for a stretch of the roadway. To correct for any instrument biases and allow the multiple data sets to be compared, data from co-located sampling of three SMPS units and the one

FMPS unit were used to develop correction factors, based on assigning one of the SMPS units as a reference.

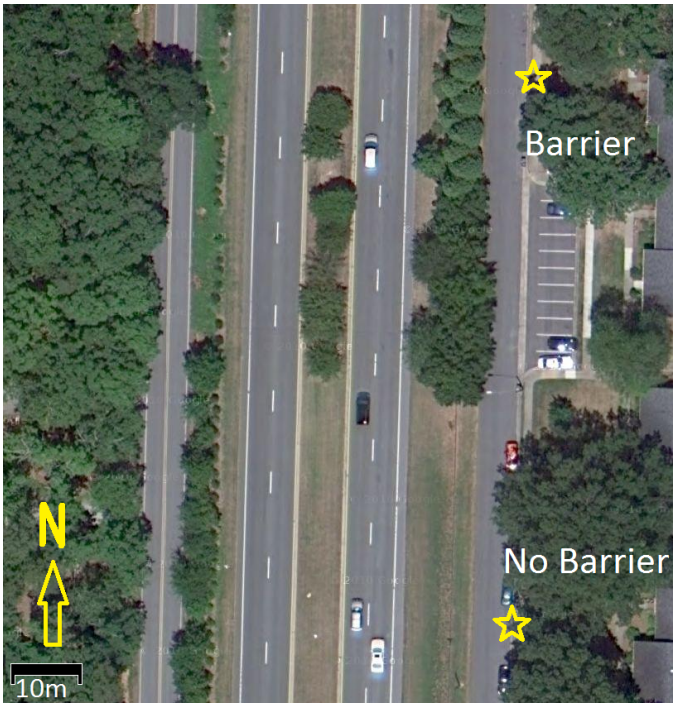

Figure 4.1: Plan view of the sampling locations (marked by stars) near NC Highway 15-501 in Chapel Hill

4.5 Modeling Scenarios

Since this study represents the first atmospheric modeling effort of pollutant transport through roadside vegetation barriers, the model formulation will only take into account a steady-state meteorological inlet condition, using average values for velocity and wind direction. The steadiness of the meteorology was evaluated on two conditions: velocity magnitude and wind direction. A 5 minute moving average of wind speed was plotted as shown in Figure 4.2. By visual inspection, it is obvious that the wind speed is more constant earlier in

the day, from about 7:00 to 7:45. The wind speeds measured over this period are low, with an average of 0.57 m/s.

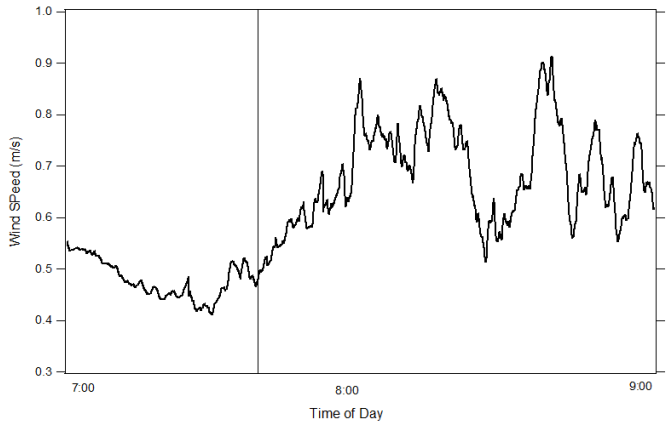

Figure 4.2: Wind speed 5 minute moving average with Morning modeling scenario represented.

Using the method of Yamartino (1984), the calmest time period was found to be from 7:00 AM to 7:45 AM, with a wind standard deviation of 48 degrees. Therefore, we will focus on this time period for the study. It is notable that 48 degrees represents a large standard deviation. Sensitivity analysis was performed by varying the wind direction plus or minus one standard deviation. It was found that at the most extreme case the particle size distribution results varied at most 15%. We further separate this period into three modeling scenarios, namely Morning, Peak 1, and Peak 2. Peak 1 and Peak 2 represent two spikes in particle number concentrations that occured 1) when there were no drastic changes in wind velocity and wind speed, and 2) at both the no barrier site and 3 m height behind the barrier. These time periods can be seen in Figure 4.3. Therefore, Peak 1 and Peak 2 captured two single plumes from traffic under steady meteorological conditions. The remaining times, when the particle number concentrations are relatively steady, are averaged and are referred to as the Morning modeling scenario throughout the paper.

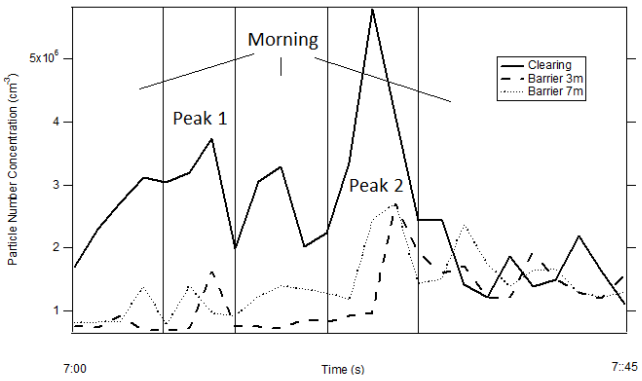

Figure 4.3: Particle number concentration for barrier and no barrier. Three modeling scenarios (Morning, Peak 1, and Peak 2) represented.

4.6 Geometry, Boundary Conditions, and Emissions

The computational domain was created using overhead satellite imagery to map the sampling area. Canopy heights were measured on site during the field study. Figure 4.4 shows the schematic of the finalized geometry. The major elements of the domain are the tree stand, the upwind and downwind canopies and a highway emissions zone. The domain has dimensions of 400 meters long by 400 meters wide by 100 meters high, divided into 4.1 million elements.

A small highway emission zone is created. This region is used to provide a source of particle emissions as well as vehicle-induced turbulence (VIT). As described in Wang and Zhang (2009), the height of this zone is taken to be roughly the height of the vehicular traffic moving along the highway (2 m). The height of the emissions zone should be dependent on the traffic composition. However, accurate traffic counts are not available for this study. However, Wang et al. (2011) found that the effect of emission zone height on concentration results is small. The size distribution profile of particle emissions released from this zone is set such that the particle size distribution simulated at the no barrier site

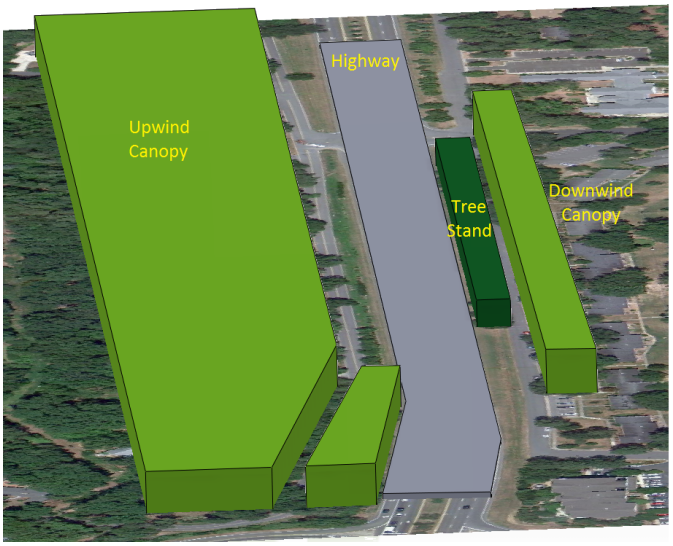

Figure 4.4: Computational domain showing highway, tree stand, upwind and downwind canopy

matches that of the experiment. The emissions released from the highway zone were taken to be constant. As vehicles travel along the roadway, they perturb the airflow, increasing the turbulence in the airflow. VIT is generated using the parameterization developed by Wang and Zhang (2009) and Wang et al. (2011).

Upwind of the highway is a forest canopy of unknown species, which is included in the model in order to allow the flow over the highway to develop naturally. The tree stand is positioned downwind of the highway, as well as the canopy further downwind of the measurement site. The small row of trees in the middle of the highway, seen in Figure 4.1, was not represented due to their small size (roughly 3m in height) and low density.

It is important to accurately represent the vegetations LAD, which is a function of height. The leaf area index (LAI) is a closely related parameter which measures the ratio of leaf surface area to ground surface are. It was measured for the site and found to be 3.3 ± 1.0 (Hagler et al., 2011). The relationship be-

tween LAI and LAD is defined as:

$$LAI = \int_0^h LADdz \tag{4.15}$$

While the LAI is not sufficient to determine the vertical profile of LAD, it does offer an important constraint. Lalic and Mihailovic (2004) offer an empirical relationship to describe LAD as a function of height given by:

$$LAD = L_m \left(\frac{h - z_m}{h - z}\right)^n exp\left[n\left(1 - \frac{h - z_m}{h - z}\right)\right], n = \begin{cases} 6, & 0 \le z \le z_m \\ 1/2, & z_m \le z \le h \end{cases} \tag{4.16}$$

where h is the canopy height, L_m is the maximum LAD and z_m is the location at which maximum LAD occurs. Lalic and Mihailovic (2004) recommend that for conifers $z_m = 0.4h$. The only remaining parameter, L_m, can be obtained by numerically integrating Equation 4.16. The LAD profile obtained from this method is shown in Figure 4.5.

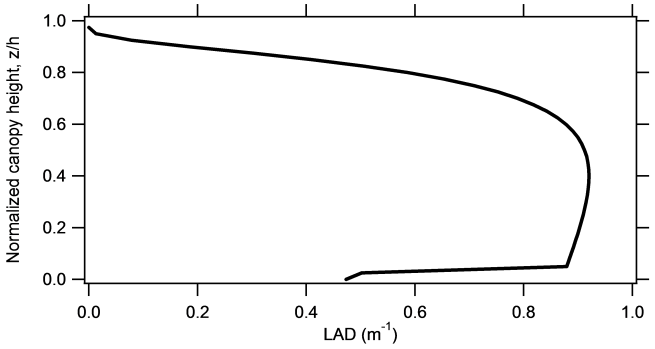

Figure 4.5: The derived LAD profile of the model vegetation barrier from observed LAI

In addition to the geometry, boundary conditions are required in order to perform simulation. The ground is defined as a no slip wall. The western side of

the domain is created to be a velocity inlet condition, where profiles of velocity and TKE must be provided. The eastern side is set to be an outlet condition. The northern and southern sides are defined as periodic conditions. This essentially allows for inlet airflow to be at any arbitrary angle and still be uniform as it exits the inlet forest canopy. The top of the domain, assumed to be high enough to not affect ground level wind flow, imposes no shearing force and is thus given a condition of no velocity gradient.

Inlet conditions are important for flow simulations and the results are sensitive to those chosen. Figure 4.1 shows that upwind of the highway, there is a fairly uniformly forested area. Cowan (1968) has created an equation to characterize the velocity profile through a forest canopy given by:

$$u = u_h \left[\frac{\sinh \beta \frac{z}{h}}{\sinh \beta} \right]^{1/2} \tag{4.17}$$

where u_h is the wind velocity at the top of the canopy and h is the canopy height. β is defined as the extinction factor and is given by (Massman, 1987):

$$\beta = \frac{4 C_D LAD}{\alpha^2 \kappa^1} \tag{4.18}$$

where κ is the von Karman constant and is typically given to be 0.4 and z_0 is the canopy roughness height and α describes the vegetative roughness and varies between 1 and 2 (Raupach and Thom, 1981). Above the canopy, the classical logarithmic atmospheric boundary layer profile is used given by:

$$\frac{u}{u^*} = \frac{1}{\kappa} ln \left(\frac{z - d}{z_0} \right) \tag{4.19}$$

The friction velocity, u^*, is not known exactly for the modeling scenario. However, it has been estimated by matching this profile to the one given in Equation 4.17 at the top of the canopy. However, the velocity and turbulence characteristics are known at the no barrier site on the other end of the highway. The velocity profile will evolve as it travels along the domain, but it is possible to vary the parameters of the inlet profile until the wind field in the simulation matches that of the measured data at the no barrier site. In this manner, some of the uncertainty is removed from the inlet boundary condition. Additionally, a sensitivity test is performed by varying the inlet parameters to gauge how the importance of the inlet parameters on concentrations.

4.7 Results and Discussions

Simulation results were obtained for the morning time period as well as the two separate peak periods. Additionally, we performed simulations to test the sensitivity of the model to geometry, upwind meteorology and vegetation leaf area.

4.7.1 Velocities

Table 4.1 shows the comparison of velocity behind the barrier between simulation and experiment for the morning period as well as each of the peak times. The velocity at a height of 3 m captures the general trend of reduced wind speed behind the barrier. However, the model is unable to accurately capture the velocity at the 7 m height. Since there is no corresponding seven meter velocity

measurement at the no barrier site, it is impossible to know what the vertical profile of velocity actually looks like. It is possible that the profiles obtained from literature do not accurately reflect the local meteorology. It is also possible that since the measurement point in near the top of the barrier, and that the barrier height is not perfectly uniform as it was modeled, that the errors lie in the geometric construction of the model. The Morning and Peak 1 modeling scenarios show the velocity to be lower at 7 m than at 3 m. Various inlet velocity profiles were simulated, and none were able to match this trend in the data. Changes in the flow field will affect particle concentrations. Since there were inaccuracies in the simulated velocities, we expect the simulated particle size distributions to also contain some inaccuracies. However, it is unclear how large of an effect this will have. A sensitivity analysis will be performed to address this issue and will be discussed in Section 4.6.3.

Table 4.1: Wind speed experimental data and simulation results

Period	Experimental Velocity (m/s)			Simulation Velocity (m/s)	
	No Barrier 3m	Barrier 3m	Barrier 7m	Barrier 3m	Barrier 7m
Morning	0.57	0.22	0.03	0.23	0.30
Peak 1	0.61	0.15	0.12	0.25	0.40
Peak 2	0.32	0.09	0.22	0.18	0.22

4.7.2 Size distributions

Figure 4.6 illustrates the comparisons between measured and predicted particle size distributions behind the barriers at the heights of 3 m and 7 m for the three simulated periods (i.e., the morning period and two peak periods) for both the Zhang et al. (2001) and the Petroff and Zhang (2010) deposition models. As described earlier, the size distributions at the no barrier site match the measured values by adjusting the emission profiles.

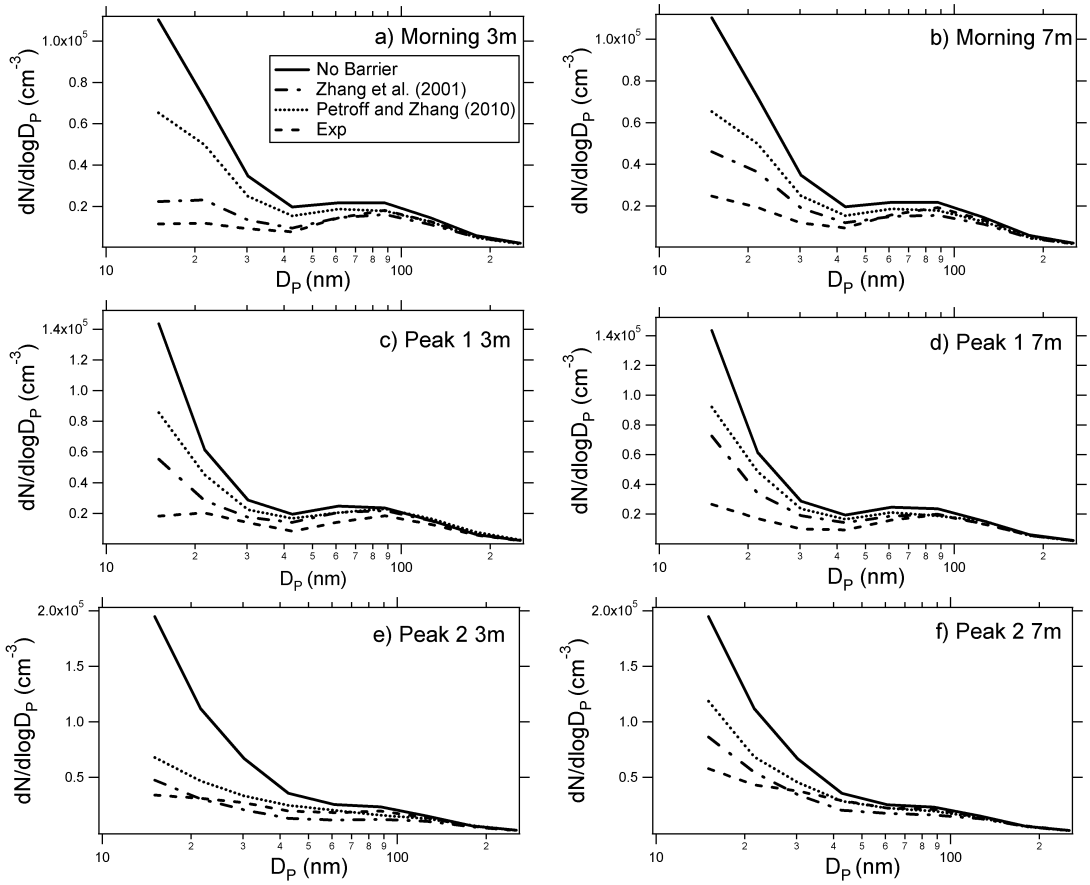

Figure 4.6: Size distribution profile comparing simulation to experiment at 3m and 7m height for modeling scenario a) Morning 3 m, b) Morning 7m, c) Peak 1 3m, d) Peak 1 7m, e) Peak 2 3m, f) Peak 2 7m.. Non-Solid lines represent concentration behind the barrier. Solid line representing no barrier site provided to illustrate concentration reduction due to the barrier.

Regardless of the dry deposition model, all of the simulations predict that more reduction in particle concentration occurs at 3m than at 7m, which agrees with the trend observed in the experimental data. The model predictions using the Zhang et al. (2001) dry deposition model show closer agreement with the measured values than those using the Petroff and Zhang (2010) dry deposition model, particularly for particle sizes below 100 nm. It should be noted that despite the discrepancies observed in the velocity measurements, the size distribution simulations perform reasonably well. There are several possible reasons to explain this phenomenon. First, since most of the dilution takes place before the barrier, and the velocity conditions in the simulation were such that they matched the experimental data, dilution should not be significantly different. Second, deposition only occurs within the canopy. However, the wind speed measurements taken in the experiment are several meters behind the barrier. It is possible that other factors, such as vegetation or other obstacles further downwind of the measurement point affected the velocity measurements but did not alter wind flow through the canopy.

For the two peak periods, the model captures the experimental concentrations with varying degrees of success. As seen with the morning period case, the model tends to predict concentrations higher than observed in the experiment in the less than 50 nm size range. The concentration differs significantly between the predicted and measured values for the first peak period in the smaller size ranges, while the comparison is quite good during the second peak period. It should be noted that the second peak period also showed the best agreement with the velocity measurement, while the morning and first peak period had larger discrepancies. It is likely then, that the errors in the flow model have a larger impact on particles less than 50 nm in diameter and that improvements

to the flow field model may have a significant improvement in the particle concentration model.

4.7.3 Sensitivity Analyses

Various sensitivity studies were performed to examine how varying the model parameters affects the simulation results. For these sensitivity tests, the morning period was used as a baseline case.

Deposition velocities

Figure 4.7 shows the deposition velocity profiles for the morning case obtained from the two dry deposition models compared with the deposition velocity profile required to produce the reduction in concentration observed during the morning period. As expected from Figure 4.6, the Zhang et al. (2001) model shows better agreement for particles less than 50 nm in diameter and the results overall. It should be noted, however, that both models were developed and validated with forest canopy field data, and not that of isolated tree stands. This may be a contributing factor for the observed discrepancies.

Coagulation

Simulations were performed both with and without the coagulation model. The difference in particle residence time behind the barrier and away from the barrier was approximately one to five seconds depending on the parameters. How-

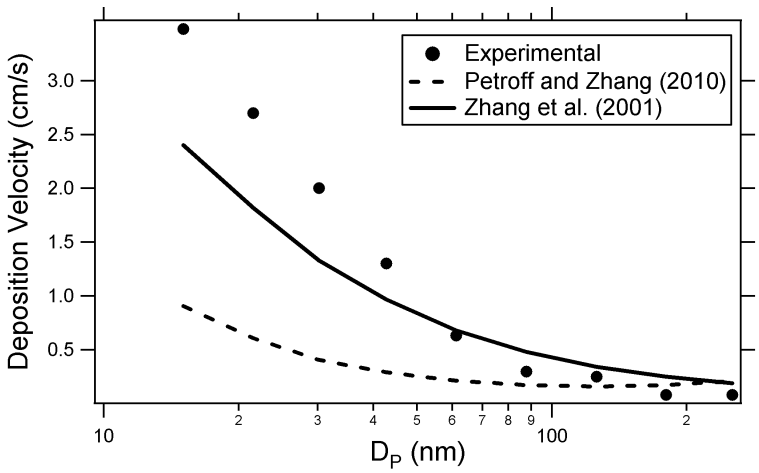

Figure 4.7: Deposition velocity curves for morning period for Petroff and Zhang (2010) and Zhang et al. (2001) models as well as deposition velocities required to exactly match experimental results

ever, such a short time was unable to produce any distinction between the simulation with and without the effects of coagulation taken into consideration.

Presence of surrounding vegetation

One possible concern is how the presence of the vegetation downwind of the measurement site affects those measurements. For this sensitivity test, the downwind vegetation was removed. It was found that doing so had negligible effect on the measured velocity at 3 m and increased the velocity at 7 m from 0.30 m/s to 0.35 m/s. However, wind speed within the canopy differed by at most 1 percent. Additionally, we simulated the case where the downwind vegetation was doubled in leaf density. We found again, that this had a negligible effect on the concentration profile.

Leaf area density (LAD)

LAD is a key parameter determining the amount of deposition that takes place within the canopy (Petroff et al., 2009). For the dependency on leaf area, three additional cases were run by multiplying the baseline leaf area density profile by a constant value to account for the effects on wind speed and deposition. Changes in vertical LAD profile may also have an effect on vertical concentration but were not considered in this study, since we only compare simulation to experiment at one height.

The three cases used leaf areas of 50, 150, and 250 percent of the baseline leaf area. Figure 4.8 shows concentration ratio between the barrier and the no barrier site, C_B/C_C, behind the barrier to the away from the barrier at three meters. Higher LAD leads to more deposition. The 150% LAD case agrees very well with the experimental data in the less than 50 nm size range. However, it over predicts concentration reduction in the larger size ranges by up to 50%. This suggests that variation of leaf area alone is insufficient in accounting for the differences between the model and the field data. It should be noted that the change in C_B/C_C is not linearly proportional to the change in LAD and affects different size ranges differently. For instance, at 50% LAD, compared to the baseline LAD, CB/CC is 2.2 times higher for 15 nm particles but only 1.2 times greater for the 273 nm particles. Conversely, at 250% LAD, compared to the baseline LAD, CB/CC is 7.4 times smaller for the 15nm particles and only 1.2 times smaller for the 273nm particles.

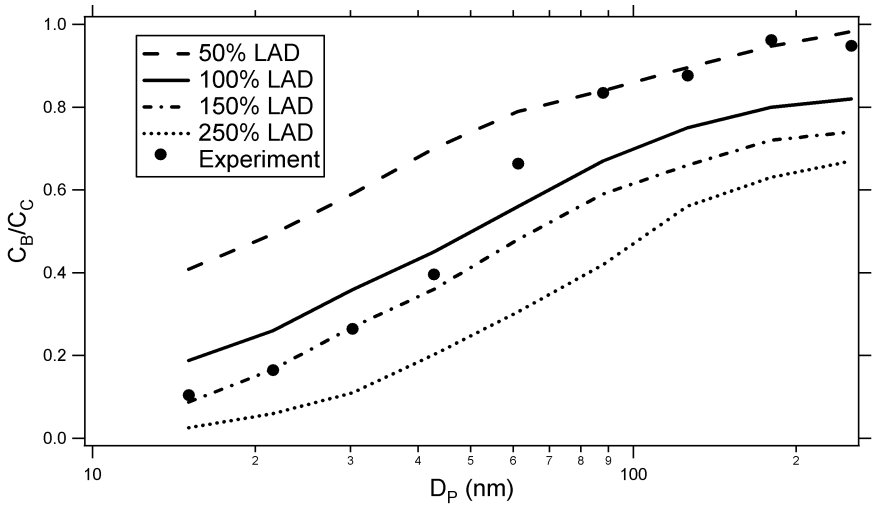

Figure 4.8: Comparison of concentration ratio between the barrier and the no barrier sites, C_B/C_C, for varying multiples of baseline LAD

Wind speed

It is also a possibility that the differences between the model and the experiment are due to uncertainties in the local meteorology. Similar to the LAD sensitivity test, the inlet meteorology sensitivity study was performed by multiplying the inlet velocity profile by a constant value. The cases performed were for inlet velocities of 50, 150 and 250 percent the baseline velocity. C_B/C_C for each velocity is shown in Figure 4.9.

For the size ranges below 50 nm, the reductions in concentration are similar for all wind speeds except the 50% velocity, which is significantly higher. There is a larger difference observed in particles greater than 50 nm in diameter. There are several competing processes which influence these changes in C_B/C_C. First, as wind speed increases, the aerodynamic resistance term in the deposition model decreases, thus increasing deposition caused by impaction. Second, an increase in wind speed decreases the residence time of the particle within the

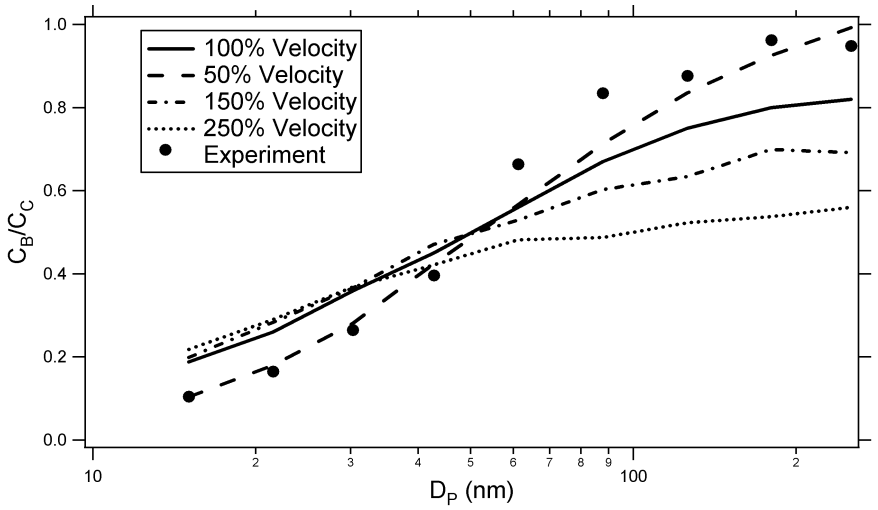

Figure 4.9: Comparison of concentration ratio between the barrier and the no barrier sites, C_B/C_C, for varying multiples of inlet velocity

canopy. This allows less time for diffusion, thus decreasing deposition. However, this does not influence impaction, since that process is not governed by how long the particle resides in the canopy but rather how likely it is to contact a solid surface as it moves through it. Third, at higher wind speeds, the particles experience more efficient vertical mixing, further enhancing the reduction of concentration. For the smaller size ranges, we see only a moderate difference in C_B/C_C for the various wind speeds. In this size range, diffusion has a much greater effect than impaction. Therefore, we expect the net effect to be an increase in C_B/C_C as velocity increases, though this effect appears to be small. Impaction becomes more important than diffusion as the particle size increases. Thus for the larger particle sizes, the net effect is a decrease in C_B/C_C as velocity increases. Overall, it appears variation in wind speed has a much greater impact on the concentration of particles larger than 50 nm than particles smaller than 50 nm.

It is also noteworthy that the 50% velocity case shows the best overall agree-

ment with the experimental data. As we have shown in Table 4.1, the simulated velocity overpredicts the velocity behind the barrier. Thus, by artificially decreasing the inlet velocity, obtaining simulated velocities closer to what was observed in the experiment, we observe an improvement in the particle concentration results. It is clear then, that further improvements must be made to the flow model in order to more accurately predict particle concentrations.

4.8 Conclusion and Recommendations

We expanded the capability of the CTAG model to account for the effects of vegetation on both the wind flow and near-road particle size distributions. The model was evaluated using experimental field measurements from Chapel Hill, North Carolina. It is found that the model performs generally well, but under predicts the reduction in concentration of particles smaller than 50 nm through a vegetation barrier.

Near-road environments are highly complex. While vegetation is just one aspect of this complexity, it offers a significant challenge in modeling these areas. The models presented in this work show generally good agreement. There are, however, areas in which these models can be improved. Most important, perhaps, is the need for improvements in the velocity simulation. It is likely that the inability of the model to fully capture velocity trends has significant impact on the particle size distributions. The model can potentially be improved by creating more detailed geometric models or by using more complicated CFD techniques such as Large Eddy Simulation (LES).

The model formulations for deposition found in literature are generally de-

veloped for regional-scale models. While this is useful for describing total deposition to forest canopies, which are generally modeled to be essentially homogenous, it may be necessary to develop newer models that take into consideration the inherent multi-dimensionality of the near-road environment. Because a large number of particles emitted by motor vehicles are smaller than 50 nm (Kittelson, 1998) and it was found that this size range is particularly sensitive to the model formulation, careful attention should be given to deposition of particles less than 50 nm in development of near-road deposition models.

The sensitivity analyses we performed show that increases in LAD will increase the amount of deposition that occurs. However, this increase is not a linear function of LAD and it affects different particle sizes differently. This suggests that in creating models, it is important to accurately represent the tree LAD, which is highly dependent on factors such as tree species and season. Likewise, changes in wind speed affect different particle sizes differently. It was observed that for the low wind speed category which we simulated, as wind speed increases, the concentration of particles less than 50nm increases while the concentration of particles greater than 50nm decreases.

As such, the aerodynamic considerations pertaining to vegetation must be handled very carefully. Realistic profiles of leaf area more accurate meteorological conditions and more detailed geometry are all areas which may need to be improved to accurately represent the flow field which ultimately drives advective transport of particulate.

CHAPTER 5

PARAMETERIZING THE EFFECTS OF SOLID BARRIERS ON NEAR-ROAD AIR QUALITY

This paper presents the development and evaluation of a parameterized model capable of predicting near-road concentrations of inert species in the vicinity of a solid barrier using a multi-regime approach. Derived based on studying the flow structures and the underlying physics, the multi-regime approach 1) describes concentration profiles outside of the wake created by the barrier (referred to as the far field regime) by a standard Gaussian plume dispersion model with a vertically and horizontally shifted emission source, 2) models the concentrations within the wake as nearly uniform (referred to as the near wake regime), and 3) creates a third regime (referred to as the transition regime) to smoothly merge the far field concentration to the wake concentration. A high-fidelity simulation model is employed to create a wide range of conditions to generate robust empirical constants. The results from this multi-regime model show good agreement with experimental wind tunnel data.

5.1 Introduction

Poor air quality near roadways has been linked to an increased risk of numerous respiratory conditions for those who live or work nearby (HEI, 2010; Adar and Kaufman, 2007; Salam et al., 2008). While reduced vehicle emissions and stricter regulation are possible strategies to improve near-road air quality, it is beneficial to investigate other possible mitigation strategies. Researchers have previously investigated the possibility that the presence of sound barriers and vegetation, while not specifically designed to do so, may result in a concentration deficit be-

hind the structure (Bowker et al., 2007; Baldauf et al., 2008; Finn et al., 2010; Heist et al., 2009) which leads to reduced exposure to these harmful pollutants. Most of the work done in this area has been experimental in nature, either through wind tunnel or field experiment. Our previous work (Steffens et al., 2013, 2014) has applied a Large Eddy Simulation (LES) turbulence model to investigate the flow structures and dispersion patterns in these regimes. While not sufficient on its own, LES analysis can provide valuable insights that experiment alone cannot. Additionally, we can use a validated computational model to perform numerical experiments, testing the response of varying flow and geometric parameters on the concentration profile relatively quickly and cost-effectively.

Simpler models for determining pollutant concentrations have been developed (Hunt et al., 1979; Sutton, 1947a,b). Gaussian plume dispersion models are one of the most widely used. These models are computationally very inexpensive, unlike the more complex simulation models, which can take days to run even with high capacity computers. Gaussian plume models, initially developed to predict pollutant concentration near stacks, have been shown to do a sufficient job even when the models have been extended to roadway concentration (Hertel et al., 1991; McHugh et al., 1997). These models have been found to be generally accurate for flat terrain cases. However, they do not accurately predict concentration when there are obstacles such as sound barriers (Hosker Jr et al., 2003).

In this study we propose a method of modifying the existing and commonly used Gaussian plume dispersion model using a multi-regime approach to account for the impact of solid barriers. Key parameters in our proposed formulation are derived from a set of numerical experiments based on LES simulations,

covering a wide range of conditions. By doing this, we hope to improve the modeling techniques used by urban designers and transportation planners.

5.2 Model Description

The main objective of this section is to describe a method of modifying a Gaussian plume dispersion model to account for the impact of solid barriers downwind of an emission source. We first describe the formulations of typical Gaussian plume dispersion models. Then, we briefly introduce the experiment and LES simulations that are basis for developing our method. Next, we present the method in great details.

5.2.1 Gaussian Dispersion Models

Employing a Gaussian model to predict near surface plume dispersion has been popular since the work of Sutton (1947a,b). Since then, several formulations have been proposed by various researchers (Van Ulden, 1978; Briggs, 1982; Venkatram, 1992). These models utilize a similar framework and act under the assumption that dispersion in both horizontal and vertical directions is Gaussian in nature. Plume spread is governed primarily by inclusion of a horizontal dispersion parameter, σ_y, and a vertical dispersion parameter, σ_z. Furthermore, these models typically assume a flat terrain.

The concentration equation generally has the same form for all of the Gaussian dispersion models. For a point source, concentration at an arbitrary point can be expressed as:

$$C(x,y,z) = \frac{A}{\sigma_y \sigma_z U} exp\left(-\frac{1}{2}\left(\frac{y}{\sigma_y}\right)^2\right)\left[exp\left(-\frac{1}{2}\left(\frac{z-z_s}{\sigma_z}\right)^2\right) + exp\left(-\frac{1}{2}\left(\frac{z+z_s}{\sigma_z}\right)^2\right)\right] \quad (5.1)$$

where A is some constant, U is the wind speed at mean plume height ($\bar{z}$), and z_s is the source height. The second vertical exponential term captures the effect of reflection from the ground. Some models also include a term to capture reflection from an inversion layer in the upper atmosphere, but it has been omitted here. Plume dispersion over a line source of length L (centered at $y = 0$) is obtained from integrating Equation 5.1 over y given by:

$$C(x,y,z) = \int_{y-L/2}^{y+L/2} C dy = \frac{A}{\sigma_z U} \times \left[exp\left(-\frac{1}{2}\left(\frac{z-z_s}{\sigma_z}\right)^2\right) + exp\left(-\frac{1}{2}\left(\frac{z+z_s}{\sigma_z}\right)^2\right)\right]\left[erf\left(\frac{y+L/2}{\sqrt{2}\sigma_y}\right) - erf\left(\frac{y-L/2}{\sqrt{2}\sigma_y}\right)\right] \quad (5.2)$$

where $erf(x)$ is the error function. For the case of an infinite line source, concentration is horizontally uniform and thus not a function of y and Equation 5.2 simplifies to:

$$C(x,y,z) = \frac{A}{\sigma_z U}\left[exp\left(-\frac{1}{2}\left(\frac{z-z_s}{\sigma_z}\right)^2\right) + exp\left(-\frac{1}{2}\left(\frac{z+z_s}{\sigma_z}\right)^2\right)\right] \quad (5.3)$$

5.2.2 Wind Tunnel Experiments and LES Simulations

The wind tunnel experiment detailed the effects of various roadway configurations on the concentration of a tracer gas, which is reported by Heist et al. (2009).

Only a brief description is presented here. Heist et al. (2009) used a meteorological wind tunnel located in USEPAs Fluid Modeling Facility. The inlet boundary layer was conditioned using Irwin spires and roughness elements along the floor to create a standard logarithmic profile. Twelve roadway configurations were used. However, for this work we only use results from the one case with a downwind barrier. The mock roadway was built to a 1:150 scale, simulating a full 6-lane highway with a 6m barrier, which corresponds to a scaled barrier height of 4 cm. A tracer gas, ethane, was released from the roadway. Concentrations of the tracer were measured at numerous heights and distances downwind of the release point.

We perform Computational Fluid Dynamics (CFD) simulations using a Large Eddy Simulation (LES) turbulence model with the Smagorinsky-Lilly subgrid model, which we found to be superior to any Reynolds Averaged Navier-Stokes (RANS) models, such as the $k - \varepsilon$ model, in our previous work (Steffens et al., 2013). We find the additional accuracy gained by the LES model to be worthwhile, despite the significantly increased computational cost over a RANS model. Computational domains were created with infinitely long barriers of heights of 3 m, 6 m, 9 m, 12 m, and 18 m at five different wind speeds, i.e., the normal wind speed and constant multiples (0.25, 0.5, 2, and 4) of the nominal wind speed. We use a power law wind profile that closely matches that of the wind tunnel experiment .

Figure 5.1 shows contours of concentration near the barrier from a LES simulation. Note the direction of wind flow is from left to right and the source is located just upwind of the barrier at ground level. Figure 5.2 shows vertical profiles of normalized concentration, which will be defined in Section 5.2.3, at

various downwind distances. Together, these figures show a couple of interesting features of the concentration behind the barrier. First, there is a zone of roughly constant concentration extending several barrier heights downwind of the barrier. Second, there is a maximum in the vertical concentration slightly above the height of the barrier. We wish to preserve these two features in creating our model.

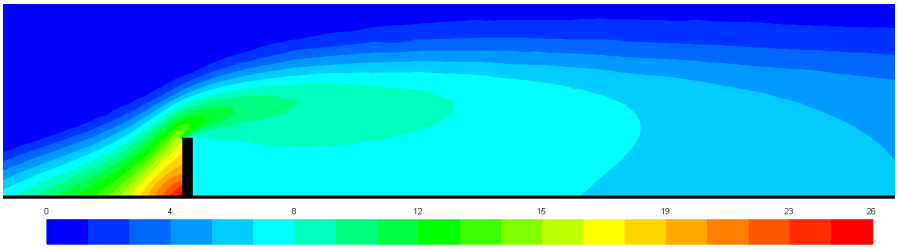

Figure 5.1: Tracer gas normalized concentration contours near a roadway with downwind barrier simulated using LES. Wind flow from left to right.

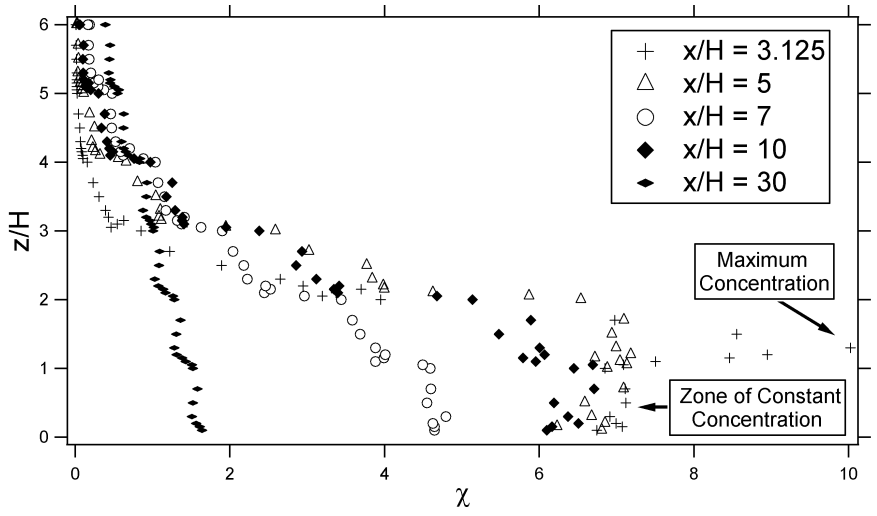

Figure 5.2: Vertical profiles of normalized concentration, , downwind at various downwind distances from the roadway. Distances all normalized by barrier height. Barrier is located at $x/H = 3$. Shown on figure are the maximum concentration occurring just above and immediately downwind of the barrier and the zone of constant concentration in the wake of the barrier.

5.2.3 The multi-regime approach

Physical characteristics

Figure 5.3 shows of the relationship between wake concentration and wind speed (Figure 5.3a) and barrier height (Figure 5.3b) from the various simulation results. In these figures we plot inverse wake concentration semi-normalized by source strength, Q, and Source length, L_y. It is clear that there is a linear relationship for both variables. This suggests that we can fully normalize concentration according to the equation $\chi = CU_H H/(Q/L_x)$ where C is local concentration, U_H is wind speed at the barrier height, H is barrier height. For an infinite source, Q/L_y is source flow rate per unit length. Assuming a linear relationships between inverse concentration and barrier height as shown in Figure 5.3a and inverse concentration and wind speed as shown in Figure 5.3b, it follows that near-wake normalized concentration, represented by the slope in these figures, is a constant , which we denote by χ_w.

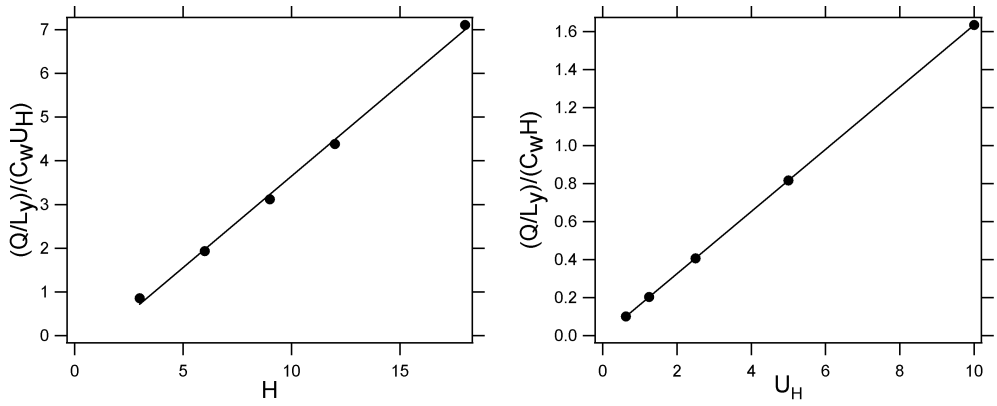

Figure 5.3: Variation in wake concentration as a function of a) barrier height and b) wind speed. Note that vertical axis shows inverse concentration.

Similarly, Figure 5.4 shows the extent of the near-wake region along the

ground, denoted by L_w, as function of barrier height (Figure 5.4a) and wind speed (Figure 5.4b). We define L_w as the distance at which change in ground level concentration first exceeds some small percent from the concentration immediately downwind of the barrier. In this study we chose 5% but note that the model is fairly insensitive to this choice. We observe that size of this region is linearly proportional to barrier height and independent of wind speed. Thus normalized wake length, which we denote by $\lambda_w = L_w/H$, is a constant. This agrees with the work of Hosker Jr (1979), who reasoned that this is true for sufficiently high Reynolds Number flow where the flow field becomes independent of Reynolds Number and sufficiently long obstacles, as the flow becomes essentially two dimensional and there is no influence from flow around the edges of the barrier. Therefore, these results are valid for long barriers and away from barrier edges. χ_w and λ_w are both evaluated from simulation data. χ_w is evaluated as the average ground level concentration from the barrier to λ_w.

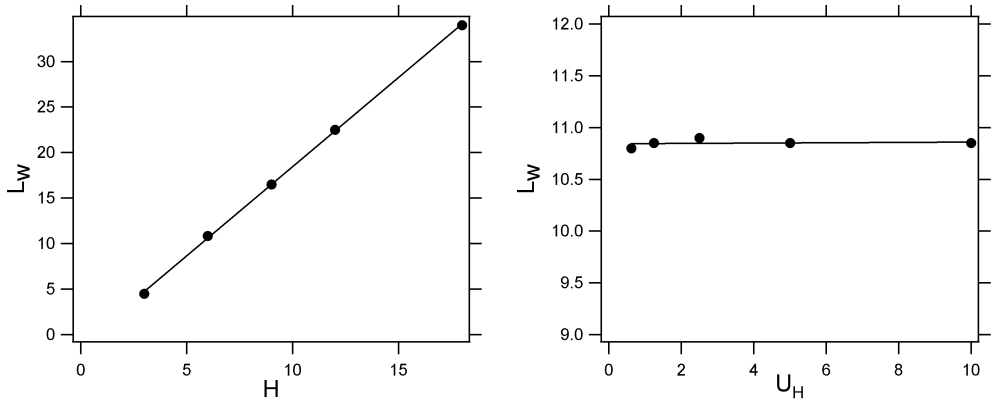

Figure 5.4: Variation in wake length as a function of a) barrier height and b) wind speed.

Formulations

We model the entire downwind space by dividing it into three regimes as shown in Figure 5.5.

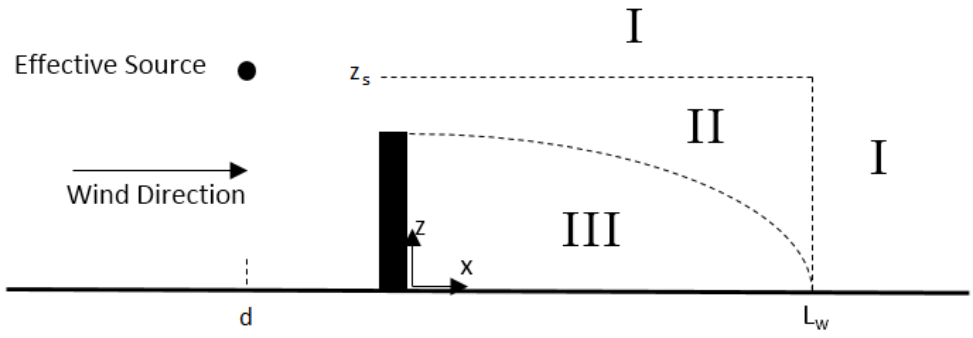

Figure 5.5: Schematic of model. Wake region forms downwind of barrier. Region I is fully outside the wake, Region III is the near-wake regime, and Region II is a transition regime. The effective source is located at (-d, zs).

Region I is fully outside the wake, referred to as far field. Region III is the near-wake regime, and Region II is a transition regime between Region I and Region III. In Region I, we assume the concentration decays according to the standard Gaussian plume dispersion model. We note that while this is not exactly true, as local changes in flow patterns are not accounted for in that model, we retain sufficient accuracy while keeping model complexity low. We require for this model a reference concentration, and an effective source location that accounts for the vertical lofting of concentration and the initial dispersion over the barrier. For the reference concentration, we observe that Region I and Region III intersect at $z = 0$, $x = L_w$. Ground level concentration is equal to a constant, χ_w, from 0 to L_w and follows the standard Gaussian decay at $x > L_w$. In order to preserve smoothness, we wish to find d such that the slope of ground level

concentration is zero at L_w since the concentration at $x < L_w$ is a constant and therefore also has a slope of 0. This is true when $\sigma_z(d + Lw) = z_s$. Therefore, d can be determined for a given function of σ_z. z_s is acquired from the simulation results. The value of z_s which bests fits the simulation data is $1.3 * H$. However, the overall model is fairly insensitive to the exact value.

Next, we solve for A in Equation 5.1 by using the condition that $\chi(x = d + L_w, z = 0) = \chi_w$ to arrive at, for concentration in Region I:

$$\chi = \frac{\sqrt{e}}{2}\chi_w \frac{z_s}{\sigma_z}\left[exp\left(-\frac{1}{2}\left(\frac{z - z_s}{\sigma_z}\right)^2\right) + exp\left(-\frac{1}{2}\left(\frac{z + z_s}{\sigma_z}\right)^2\right)\right] \tag{5.4}$$

Finally, we need to define the concentrations within Region II. In this region, we aim to create a transitional function between Region I and Region III which smoothly transitions from $\chi_w(z = z_w)$, the height of the border between Region II and Region III as a function of downwind distance, to $\chi(x, z)$ at $z = z_s$. z_w is dependent on the specified shape of the barrier. In this study we choose a quarter ellipse, given by Equation 5.5. However, we find the model to be fairly insensitive to the shape.

$$z_w = H\left[1 - \left(\frac{x}{L_w}\right)^2\right]^{1/2}, x < L_w \tag{5.5}$$

For smoothness we match both the function values and first derivatives at zw and zs using a cubic Hermite spline to obtain, for Region II:

$$\chi = [2(\chi_w - \alpha) + \beta(z_s - z_w)]\left(\frac{z - z_w}{z_s - z_w}\right)^3 - [3(\chi_w - alpha) + \beta(z_s - z_w)]\left(\frac{z - z_w}{z_s - z_w}\right)^2 + \chi_w \quad (5.6)$$

α is set to equal to χ evaluated at $z = z_s$ using Equation 4 and β is $\frac{d\chi}{dz}$ at $z = z_s$ using Equation 5.4 . This formulation assumes some way to compute z_w. In this work we assume a quarter elliptical wake from the top of the barrier at $x = 0$ to ground level at $x = L_w$. Thus $z_w = H\left[1 - (x/Lw)^2\right]^{1/2}$. Moreover, we find the results are fairly insensitive to wake shape.

5.3 Model Evaluation

We evaluate the model against the wind tunnel experimental data. A number of formulations for σ_y and σ_z have been proposed in previous studies (Miller, 1978; Venkatram et al., 2013). In this study, we use the formulation presented by Snyder et al. (2013), specifically designed for near-surface dispersion, in which the dispersion parameters are defined as:

$$\sigma_z = 0.57\frac{u^* x}{U}\frac{1}{1 + 3\frac{u^*}{U}\left(\frac{x}{L}\right)^{2/3}}, \quad for\ stable\ conditions \quad (5.7)$$

$$\sigma_z = 0.57\frac{u^* x}{U}\left(1 + 1.5\frac{u^*}{U}\frac{x}{L}\right), \quad for\ unstable\ conditions \quad (5.8)$$

$$\sigma_y = 1.6\frac{\sigma_v \sigma_z}{u^*}\left(1 + 2.5\frac{\sigma_z}{|L|}\right), \quad for\ stable\ conditions \quad (5.9)$$

$$\sigma_y = 1.6\frac{\sigma_v \sigma_z}{u^*}\left(1 + \frac{\sigma_z}{|L|}\right)^{-1/2}, \quad for\ unstable\ conditions \tag{5.10}$$

where u^* is the friction velocity, L is the Monin-Obukhov length, σ_v is the standard deviation of the horizontal velocity fluctuations.

Figure 5.6 shows the comparison of vertical concentration profiles between model and experimental observations. The model compares generally favorably. There is an overprediction of concentration at higher elevations and at $x/H = 15$.

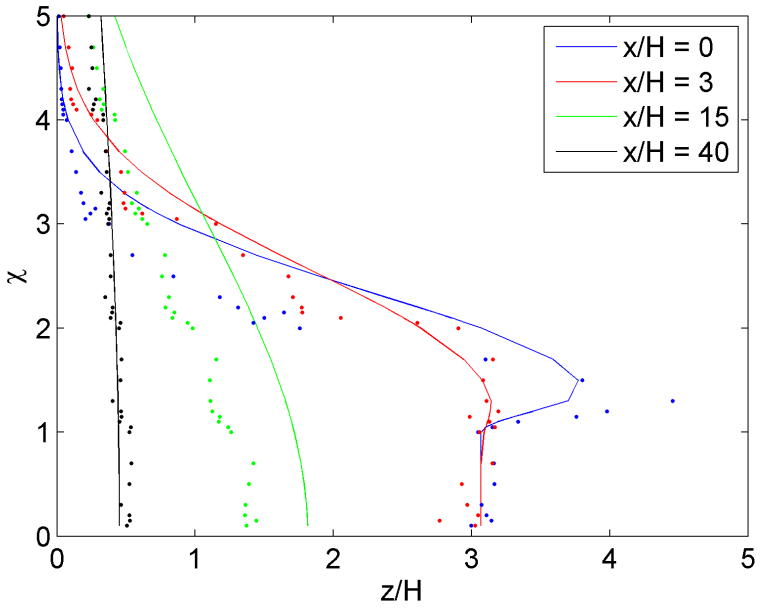

Figure 5.6: Profiles of vertical concentration for model (solid lines) and experiment (points) at $x/H = 0$ (blue), $x/H = 3$ (red), $x/H = 15$ (green), $x/H = 40$ (black).

Ground level concentration is shown in Figure 5.7. Here we observe a similar effect. The comparison is strong near the barrier and far downwind, but there is a slight overprediction in the model between $x/H = 5$ and $x/H = 20$.

Figure 5.8 shows log-log plot of modeled concentration and observed concentration at points lower than $z/H = 3$. The 1:1 centerline, which would represent a perfect correlation is shown. The outer lines represent a factor of two difference in model prediction and observed results. Overall, the model performs well, with $R^2 = 0.91$ and the majority of points within a factor of two. Many of the points which fall outside this limit are very low concentrations which have less impact on overall model accuracy. We do observe the model generally overestimates concentration slightly, but captures the general observed trends. We also calculate normalized mean error (NME) to be 0.25 and mean fractional error to be 0.51. This indicates a strong comparison for higher concentrations, but a weaker comparison for lower concentration values.

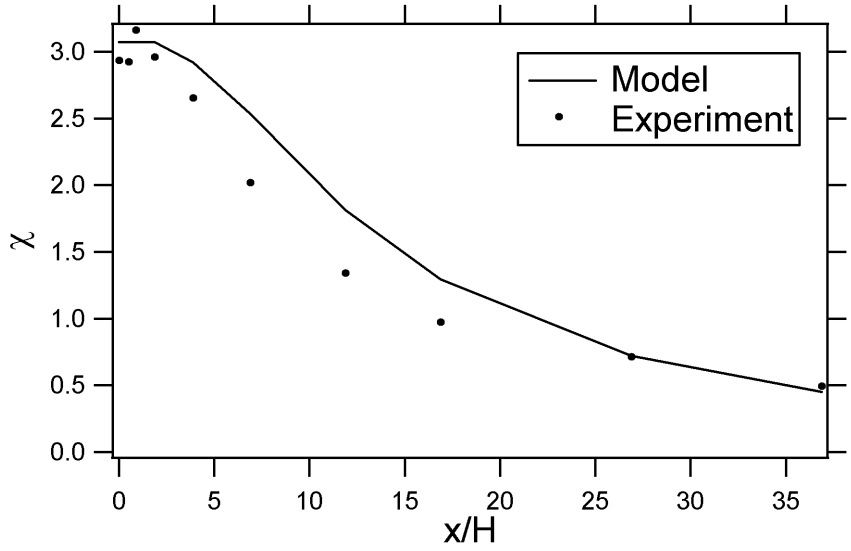

Figure 5.7: Ground level concentration for model (solid line) and wind tunnel experiment (points).

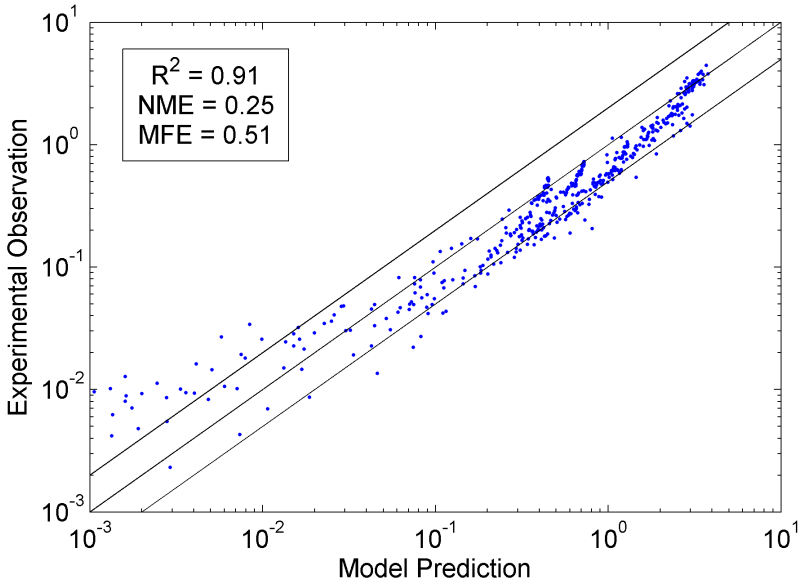

Figure 5.8: Wind tunnel experimental observation vs. model prediction for points less than z/H = 3. R2 = 0.84. Outer lines represent factor of 2 difference.

5.4 Conclusion

Gaussian plume dispersion models are a useful tool for estimating pollutant concentrations near roadways. While these models have been shown to be accurate for flat terrain, they cannot capture the concentration near solid barriers such as noise walls. We present a novel method for modifying the standard Gaussian formulation to account for these structures. Previously, we have validated our CFD model against experimental results. We choose an LES turbulence solver over the simpler RANS model as we feel the increase in accuracy necessitates the increase in computational expense. Simulations were used to observe the physical behavior of the flow around the solid barrier to inform how we can modify the Gaussian plume dispersion model to incorporate the

effects of solid barriers. We adopt a multi-regime approach which separates the computational domain into three distinct regions. The first, within the recirculation zone, is held at some constant concentration. The second, outside of the recirculation zone, follows the standard Gaussian formulation with the source of concentration shifted some distance vertically and horizontally to account for the lofting of concentration and the increased vertical dispersion caused by the presence of the barrier. Finally, the last region is a transition region which smoothly connects the others.

Several empirical coefficients are required for the model. Again, we use generated data from our simulation to determine these. Then we compare our model with a wind tunnel experiment, performed by the EPA, measuring tracer concentration downwind of a simulated roadway and solid barrier. Overall, the model performs quite well. While the model generally overpredics concentration at most locations by a relatively small amount, it captures the general trends in concentration observed in both the experiment and simulation.

CHAPTER 6

PARAMETERIZING THE EFFECTS OF VEGETATION BARRIERS ON NEAR-ROAD AIR QUALITY

6.1 Introduction

Elevated concentrations of traffic related air pollutants near roadways has been linked to serious health complications such as asthma, cardiovascular disease, and birth defects (HEI, 2010; Adar and Kaufman, 2007; Salam et al., 2008). As such, it is imperative to explore methods for reducing human exposure to these harmful emissions. One potential solution is in roadway design itself. It has been found that raised highways and solid barriers typically have a positive impact on human exposure to local pollutant concentration at ground level (Heist et al., 2009; Finn et al., 2010; Baldauf et al., 2008; Cahill, 2010; Steffens et al., 2013). Researchers have also begun to investigate the effectiveness of vegetative barriers (Buccolieri et al., 2009; Hagler et al., 2012). However, information on their efficacy is still lacking. While barriers can act as a deposition source to harmful particulate (Beckett et al., 1998; Nowak et al., 2006), reductions in turbulent diffusion and convective transport can lead to increases in concentration (McNaughton, 1988). One field experiment shows that concentration behind vegetation can be higher or lower depending on a number of factors (Hagler et al., 2012). However, due to the large number of confounding factors, it is hard to determine what sets of conditions leads to higher or lower concentrations.

Previously, we implemented and validated a Computational Fluid Dynamics (CFD) model to simulate vehicle emission dispersion for a near-road environment with a tree stand (Steffens et al., 2012). We propose that we can use this

model to simulate a variety of cases in order to gain a deeper mechanistic understanding of how vegetation affects near-road dispersion. Then we will aim to use this understanding to create a simple parameterized model which will be easily accessible to the urban and transportation planning communities, while retaining sufficient accuracy to be generally useful.

6.2 CFD Model Description

6.2.1 Aerodynamic Model

We employ the ANSYS Fluent commercial software package (ANSYS, 2009) as the flow solver. As atmospheric boundary layer flow is inherently turbulent, we must choose an appropriate turbulent closure scheme. In Steffens et al. (2012) we have shown the $k - \varepsilon$ turbulence scheme to perform adequately in the presence of vegetation (Jones and Launder, 1972). This model solves the closure problem by relating the Reynolds Stress term to the turbulent kinetic energy, TKE, and turbulent dissipation rate, ε.

6.2.2 Vegetation Model

In reality, vegetation consists of numerous small leaf and branch elements which perturb incoming wind. This results in a drag force which acts on the bulk flow. Additionally, mean flow kinetic energy is converted into turbulent kinetic energy. However, the small element spacing results in a rapid dissipation of turbulent eddies. This creates a zone of low turbulence in the lee of the barrier

(Kaimal and Finnigan, 1994) which is often referred to as a windbreak. These effects must be captured in our vegetation model. However, explicitly resolving these elements would be prohibitively computationally expensive. As such, we use a special averaging to produce average wind speed and turbulence statistics within the vegetation canopy. The canopy, then, is modeled as a completely fluid region with sink terms in the governing momentum equations, and the model equations for TKE and epsilon.

The momentum drag is given by:

$$S_u = -\rho C_D LAD u^2 \tag{6.1}$$

where ρ is the fluid density, C_D is the plant coefficient of drag (specific to plant type), LAD is leaf area density. Greens et al. (1995) formulates sink terms for the k and ε model equations as:

$$S_k = -\rho C_D LAD \left(\beta_p u^3 - \beta_d u k\right) \tag{6.2}$$

$$S_\varepsilon = -\rho C_D LAD \left(C_{\varepsilon 4}\beta_p \frac{\varepsilon}{k} u^3 - C_{\varepsilon 5}\beta_d u \varepsilon\right) \tag{6.3}$$

where β_p is the fraction of mean flow converted to turbulent kinetic energy and β_d is fraction of turbulent kinetic energy dissipated within the canopy (Greens et al., 1995) and $C_{\varepsilon 4}$ and $C_{\varepsilon 5}$ are $k-\varepsilon$ model parameters.

6.3 Model Formulation

We performed simulations for a long rectangular tree with a constant leaf area density. A simulated road source 10 m wide is centered 15 m upwind of the 8 m tall by 6 m wide vegetative barrier. The inlet is given as a standard power law atmospheric boundary layer profile with neutral stability condition and reference wind speed of 2.5 m/s at a height of 10 m. Periodic boundaries on the sides of the domain simulate an effectively infinitely long barrier and source. Figure 6.1 shows the side profile of the domain.

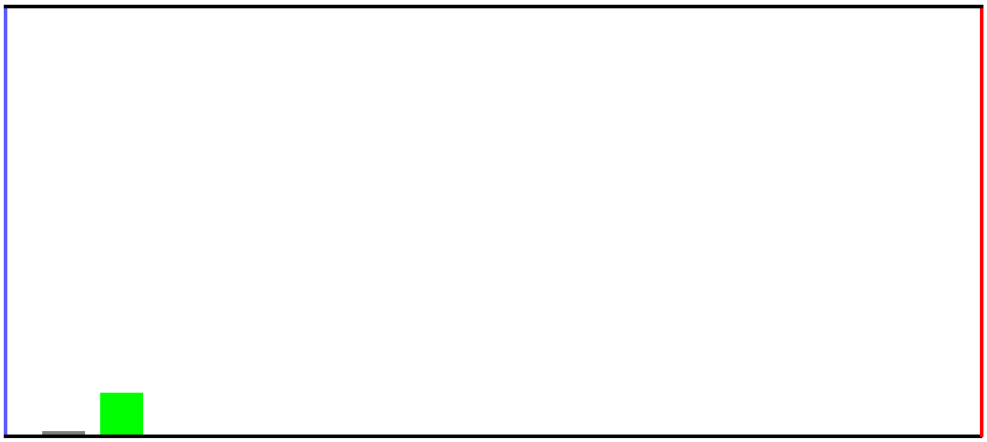

Figure 6.1: Side view of simulation domain showing relative location of vegetation barrier (green), roadway source (grey).

Figure 6.2 shows contours of TKE at several downwind locations. The barrier is located at x/H = 3. The windbreak effect is clearly visible as the TKE near the ground and immediately downwind of the barrier is very low. A band of very high TKE is observed extending from the top of the barrier downwind. This is explained by the compression of velocity streamlines over the barrier creating a shearing layer which induces turbulence (Finnigan and Bradley, 1983). Further downwind, this band expands towards the ground before it begins to

decay. This general trend agrees with wind tunnel windbreak experiments (McNaughton, 1988; Heisler and Dewalle, 1988).

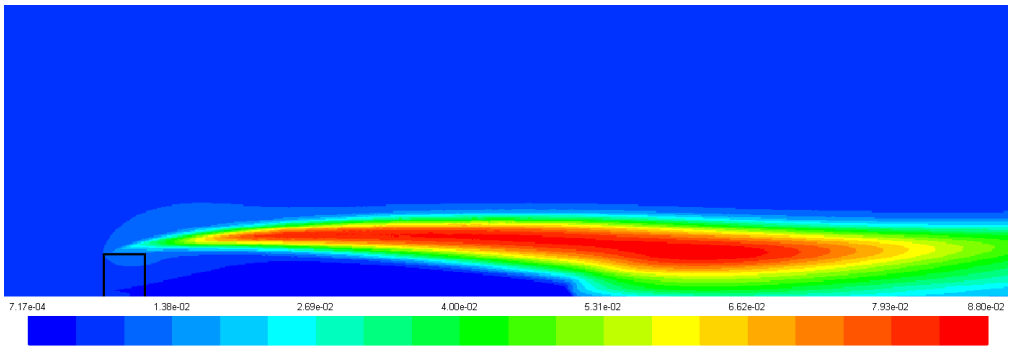

Figure 6.2: Contours of turbulent kinetic energy (TKE).Vegetation barrier outlined in black. A band of high turbulence starting near the top of the barrier and expanding downward to the ground is clearly visible. Immediately behind the barrier below this band is a very calm zone of low turbulence.

As turbulent diffusion is a significant driver of dispersion, it stands to reason this will have a significant effect. A number of studies note that this calm windbreak effect behind the barrier leads to an increase in scalar concentration as compared with a no barrier case (Patton et al., 1998; Cleugh, 1998; McNaughton, 1988; Wang et al., 2001). Indeed, as is shown in Figure 6.3, we see an interesting phenomenon.

This figure shows ground level normalized concentration profiles for a case with no vegetation and tree stands with Leaf Area Density (LAD) of 1 m^{-1} and 4 m^{-1}. Upwind of the barrier, the two cases behave similarly. Minor discrepancies are explained by deceleration of the approach flow in the vegetation case. However, immediately downwind, concentration decay behind the vegetation barrier is slower in comparison to no barrier case. Then, at some point, the decay rate increases rapidly. This coincides with the changes in TKE from Figure 6.2. Immediately downwind of the barrier, the shelter creates very low turbulence

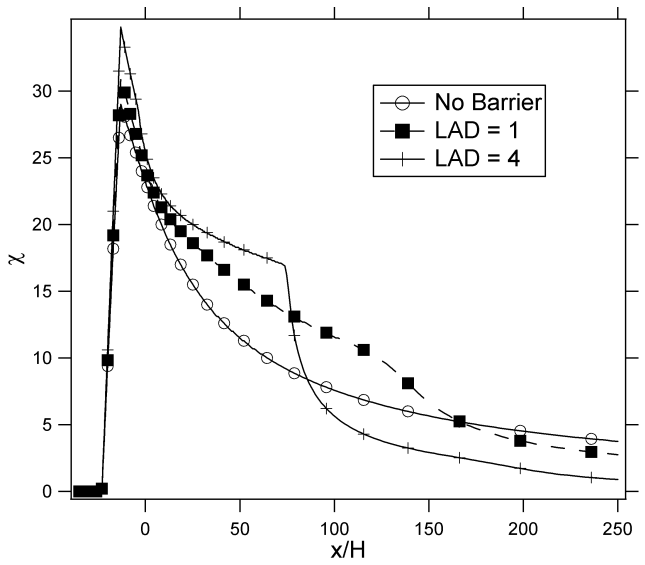

Figure 6.3: Horizontal ground level normalized concentration profiles for a barrier with leaf area density of one, leaf area density of four, and a no barrier case. Initial dispersion is slower behind vegetation barrier compared with no barrier case. After some distance, interaction with high turbulence zone causes sharp increase in dispersion.

region, which inhibits vertical transport due to very low turbulent diffusion. Then, as the large zone of turbulence expands into the path of the plume, the plume undergoes rapid dispersion. This suggests that we can model the overall dispersion as three separate zones: the upwind region, the low turbulence shelter region, and high turbulence far region, which we will denote Region I, Region II, and Region III, respectively. A schematic of these division are shown in Figure 6.4.

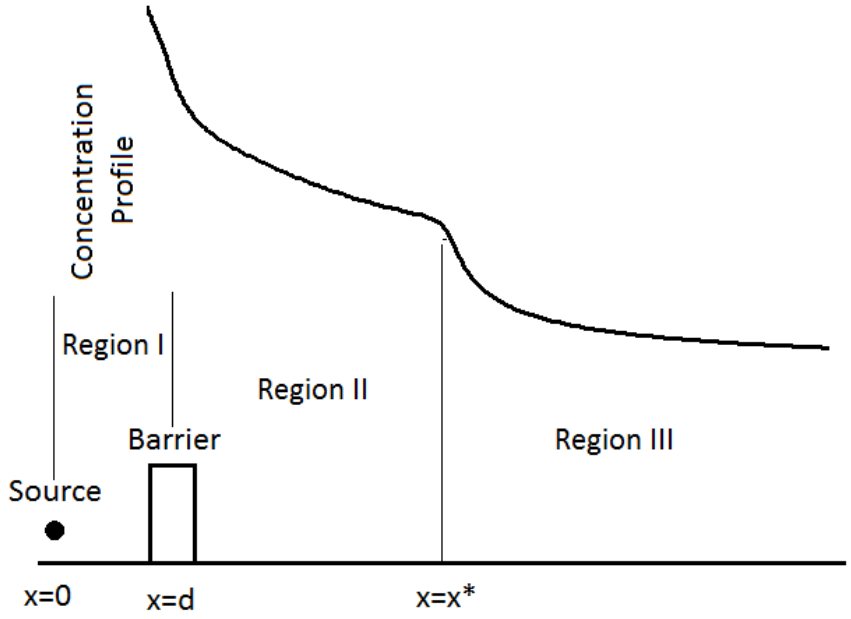

Figure 6.4: Schematic showing the division of the model into three regions with relative concentration profile overlayed. Region I extends from the source to the barrier. Region II extends from the barrier to the inflection point in the concentration profile. Region III extends downwind of the inflection point.

6.4 Gaussian Plume Dispersion Framework

Gaussian Plume Dispersion models work under the assumption that concentration is normally distributed in the vertical and crosswind directions, which can be characterized by horizontal and vertical dispersion parameters denoted by the symbols σ_y and σ_z, respectively. For the case of an infinite line source (as we have in this paper), the basic equation for concentration, C, is given by:

$$C(x,z) = \frac{Q}{\sqrt{2\pi}\sigma_z U}\left[exp\left(-\frac{1}{2}\left(\frac{z-z_s}{\sigma_z}\right)^2\right) + exp\left(-\frac{1}{2}\left(\frac{z+z_s}{\sigma_z}\right)^2\right)\right] \tag{6.4}$$

where Q is the source strength, σ_z is the vertical disperion parameter, U is the wind speed at mean plume height, and z_s is the source height. For our purposes, we wish to use normalized concentrations, χ We will normalize according the equation $\chi = CUH/Q/L_x$ where H is the barrier height and L_x is the source crosswise length. For an infinite barrier, Q/L_x is the source strength per unit width. Therefore, using normalized concentration and normalizing σ_z, z, and z_s by H, Equation 6.1 becomes:

$$\chi = \frac{1}{\sqrt{2\pi}\sigma_z}\left[exp\left(-\frac{1}{2}\left(\frac{z-z_s}{\sigma_z}\right)^2\right) + exp\left(-\frac{1}{2}\left(\frac{z+z_s}{\sigma_z}\right)^2\right)\right] \tag{6.5}$$

Additionally, we use the formulation for σ_z given by Snyder et al. (2013):

$$\sigma_z = 0.57\frac{u^* x}{U}\frac{1}{1+3\frac{u^*}{U}\left(\frac{x}{L}\right)^{2/3}}, \quad for\ stable\ conditions \tag{6.6}$$

$$\sigma_z = 0.57\frac{u^* x}{U}\left(1+1.5\frac{u^*}{U}\frac{x}{L}\right), \quad for\ unstable\ conditions \tag{6.7}$$

It is instructive to observe the trends of inverse ground level concentration as shown in Figure 6.5. The no barrier case is nearly linear over the entire domain, except for very near the source. This is consistent with equations 6.2 and 6.3, since, as σ_z increases, the exponential terms quickly go to unity, and dispersion is dominated by the linear term and σ_z is almost linearly proportional to downwind distance. Likewise, the three sections of the barrier profiles are each nearly linear. There is some curvature observed in the far field concentration which is expected as the region of very high turbulence damps out. However, the concentrations that far downwind are small and we will not lose significant

accuracy by assuming linearity. We can define some $\sigma_{z,eff}$ by linearly transforming σ_z. In doing this, we assume the sharp changes in TKE have a constant and linear effect on vertical dispersion. In other words, the vertical concentration profiles remain Gaussian in nature, but the rate of decay slows down in Region II and speeds up in Region III and we will modify the vertical dispersion parameter to account for this.

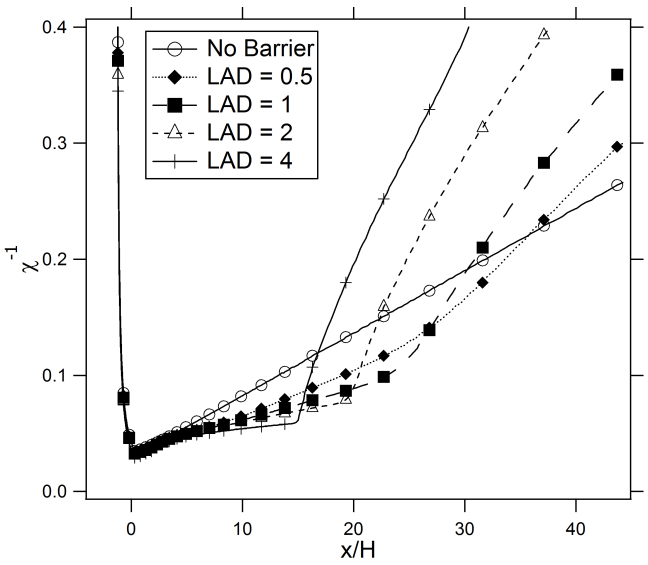

Figure 6.5: Horizontal ground level inverse normalized concentration profiles for varying Leaf Area Densities showing decay generally follows x^{-1}

To do this, we must make a couple of assumptions in our model. In defining a $\sigma_{z,eff}$, we assume the vertical dispersion of the plume is still represented by the Gaussian model. This is not exactly true. From Figure 6.2, we observe that the band of high turbulence moves down into the path of the plume at some angle. As such, the top of the plume would interact with the high turbulent zone further upwind than the bottom part of the plume. This will lead to a non-uniform change in vertical dispersion. For our model, we essentially assume the plume interacts with this band as if it were a vertical wall of high turbulence.

To minimize the impact of this effect, we also assume that the source is close enough to the barrier that the entire plume passes through the barrier. If any of the plume passes over the barrier, it would immediately interact with the region of high turbulence and significantly distort the vertical profile. This has the effect of making our model less accurate for very dense canopies as more of the flow is diverted up and over the barrier, increasing the chance that the plume is convectively transported over the barrier and greatly skewing the vertical concentration profile away from a Gaussian curve.

By defining an effective σ_z, we will expand or contract the plume equation to effectively change the decay rate. And since, except for the edge of the plume, the decays are nearly linear, we can linearly transform σ_z. $\sigma_{z,eff}$ must have two constraints. It must preserve continuity over all z in order for our solution to be continuous and it must have a term which can freely be altered to change the decay rate. As such, we can define $\sigma_{z,eff}$ in a piecewise function given by:

$$\sigma_{z,eff} = \begin{cases} \sigma_z(x), \quad x \leq d \ (\textit{Region I}) \\ \alpha\Big(\sigma_z(x) - \sigma_z(d)\Big) + \sigma_z(d), \quad d \leq x \leq x* \ (\textit{Region II}) \\ \alpha\Big[\beta\Big(\sigma_z(x) - \sigma_z(x*)\Big) + \sigma_z(x*)\Big] - \sigma_z(d) + d \quad x \geq x* \ (\textit{Region III}) \end{cases} \tag{6.8}$$

where d is the distance from the source to the barrier, dividing Region I from Region II and $x*$ is the inflection point dividing Region II from Region III, as seen in Figure 6.4. α and β are slope parameters. Physically, α is the ratio of slopes between Region I and Region II and β is the ratio of slopes between Region II and Region III. d should be prescribed by the roadway geometry. $x*$, α and β will be determined empirically. As we noted before, this method assumes the plume retains its Gaussian profile. However, since we demonstrated that the

top of the plume will begin rapid expansion further upwind, there will be some sensitivity in our empirical parameters to height at which we observe where the plume transitions from Region I to II and II to III. As such, our empirical fits will occur at the mean plume height, $\bar{z}$, recognizing that the model will overpredict concentration above the mean plume height as it will expand faster than the model predicts, and the model will underpredict concentration below the mean plume height for the opposite reason.

6.5 Empirical Fitting

We have performed a number of simulations to determine how the three empirical coefficients, α, β, and $x*$ vary as a function of leaf area density and barrier height. To do this, we simulate several different leaf area densities. Figure 6.6 shows how these coefficients vary with LAD. We can see that the relationships are clearly not linear so we have fit a power function curve to each. The best fit curves are found to be:

$$\alpha = 0.43 LAD^{-0.54} \tag{6.9}$$

$$\beta = 2.41 LAD^{0.66} \tag{6.10}$$

$$x* = 12.61 LAD^{-0.37} \tag{6.11}$$

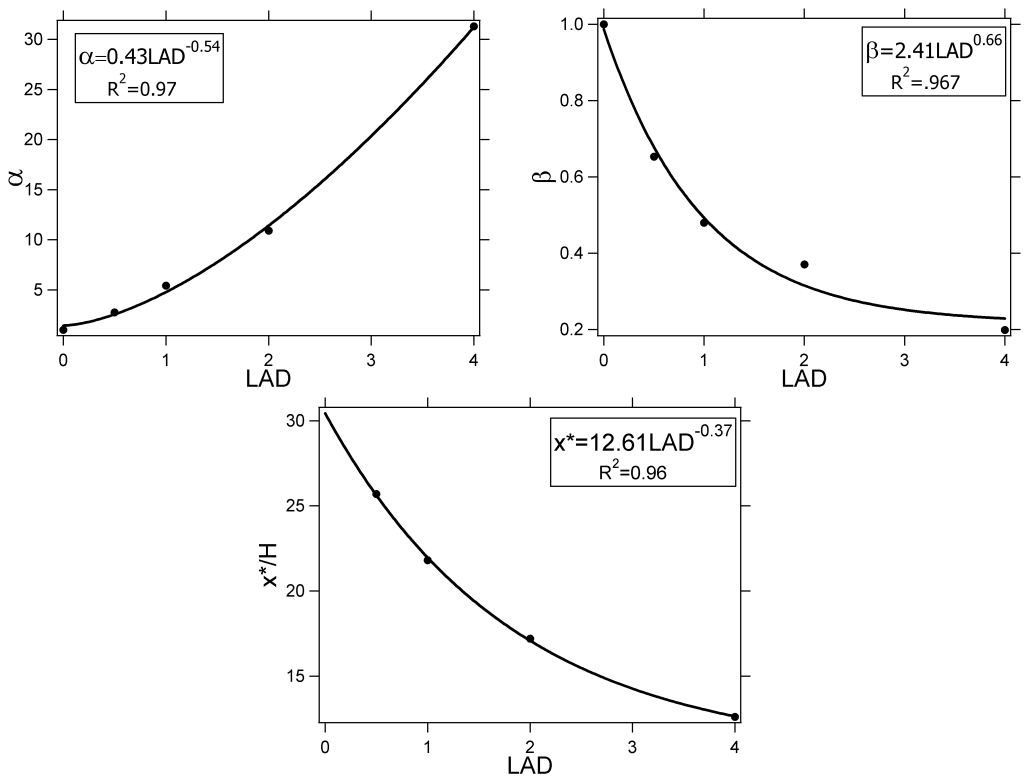

Figure 6.6: Relationship between LAD and the empirical coefficients a) α, b) β, and c) $x*$. Power law curves are used to fit the data with a high correlation.

In Figure 6.7 we show ground level inverse concentration for barrier heights of 5 m, 10 m, and 15 m. It is clear that the Region II slopes are highly similar and the Region III slopes are fairly similar near the inflection point and only begin to curve further downwind. As such, we will assume α and β have no dependence on barrier height. However, $x*$ clearly does have dependence on barrier height. Figure 6.8 shows a fairly linear relationship between barrier height $x*$, which suggests we should normalize x* by H.

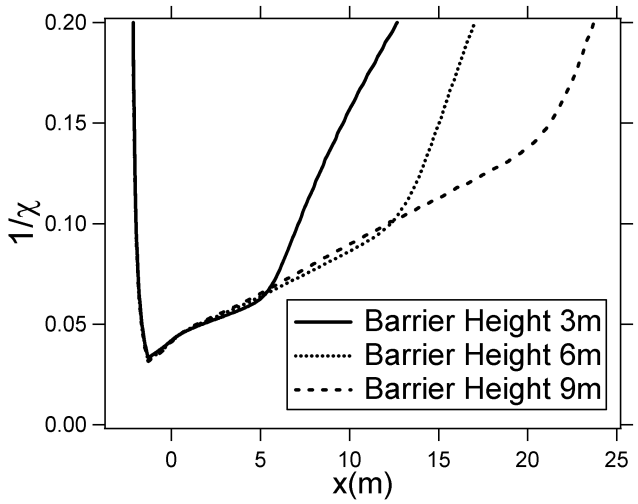

Figure 6.7: Ground level inverse concentration for barrier heights of 5 m, 10 m, and 15 m showing $x*$ varies with barrier height while α and β (related to the slopes in Regions I, II, and III) have little dependence on barrier height.

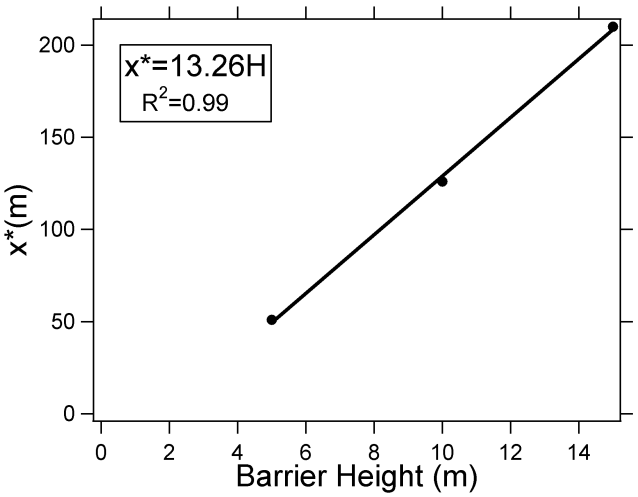

Figure 6.8: Nearly linera relationship between barrier height and $x*$, suggesting we normalize $x*$ by barrier height, H

6.6 Results and Discussion

Unfortunately, we lack experimental validation for our model. However, we can compare the Gaussian model results with the CFD simulation results. The following comparisons are made with $H = 6m$ and $LAD = 1$. Figure 6.9 shows the comparison of inverse ground level concentration. The model compares quite favorably overall. The slope of concentration decay is similar at the mean plume height as it is at ground level for both Region II and Region III. However, as expected the location of $x*$ is further downwind at ground level, as it takes longer for the lower part of the plume to interact with the band of high turbulence.

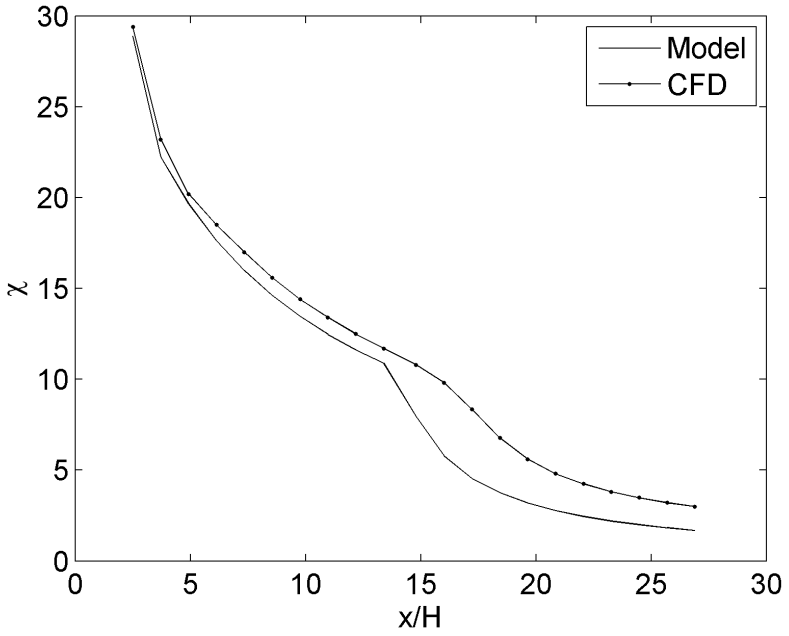

Figure 6.9: Ground level inverse concentration comparison between Gaussian model and CFD. Model run with H=8m, LAD = 1

We show several statistical metrics to demonstrate the strength of the model. Table 6.1 summarizes the statistical metrics for each of the three densities we

have compared. We present values of R^2, normalized mean error (NME), and mean fractional error (MFE). NME measures the percent difference between the predicted and observed values with a larger weighting for larger values. MFE is a measure of percent difference (bounded by 0% and 200%) which does not give preferential weighting to larger values. Figure 6.10 shows the overall comparison of sampled points from the barrier extending downwind $40H$ and from the ground extending upward to $5H$ for a) LAD = 1, b) LAD = 2, and c) LAD = 4. We use a log-log plot since the values of concentration span many orders of magnitude. Outer bars represent a factor of two difference. The results overall are fairly strong for the lower density case (LAD = 1) and become weaker as LAD increases. As stated in Section 6.4, we assume the canopy density is not large in developing our model. It would appear that this assumption should be seriously considered when applying this model to dense canopies, as the model begins to break down.

Table 6.1: Comparison of model with simulation data showing R^2, normalized mean error (NME), and mean fraction error (MFE)

LAD	R^2	NME	MFE
1	0.96	0.26	1.37
2	0.89	0.33	1.31
4	0.65	0.48	1.13

It is immediately apparent that the fit for the largest values of concentration is quite good. These values would fall near the ground immediately behind the barrier, before the plume begins rapidly dispersing. In this sense, the model accurately predicts how the plume dispersion slows dramatically behind the barrier. The smaller concentrations tend to be either severely overpredicted or

underprediced, with few falling within a factor of two. These points are generally those near the edges of the plume. Above the mean plume height, the plume undergoes rapid dispersion further upwind than predited resulting in large model overprediction. The opposite is true for concentration below the mean plume height.

6.7 Conclusion

We develop a simple parameterized model to modify existing Gaussian plume dispersion models. By observing the influence of the barrier on turbulent kinetic energy, and therefore turbulent diffusion, we see that a high band of TKE creates regions of vastly different diffusion rates. Thus we separate the domain into three regions and define a diffusion parameter based on mean plume height concentration and an effective downwind distance. Overall, the model performs reasonably well considering its simplicity, with $R^2 = 0.96$, $NME = .26$, and $MFE = 1.37$ for LAD = 1. However, model performance is worse for larger values of LAD. The model shows strong agreement immediately behind the barrier, where the windbreak effect strongly damps turbulence. We recognize that this work is still somewhat preliminary as we lack experimental validation. For future work, we hope to have a wind tunnel or field experiment suitable for proper validation and to help further refine the model.

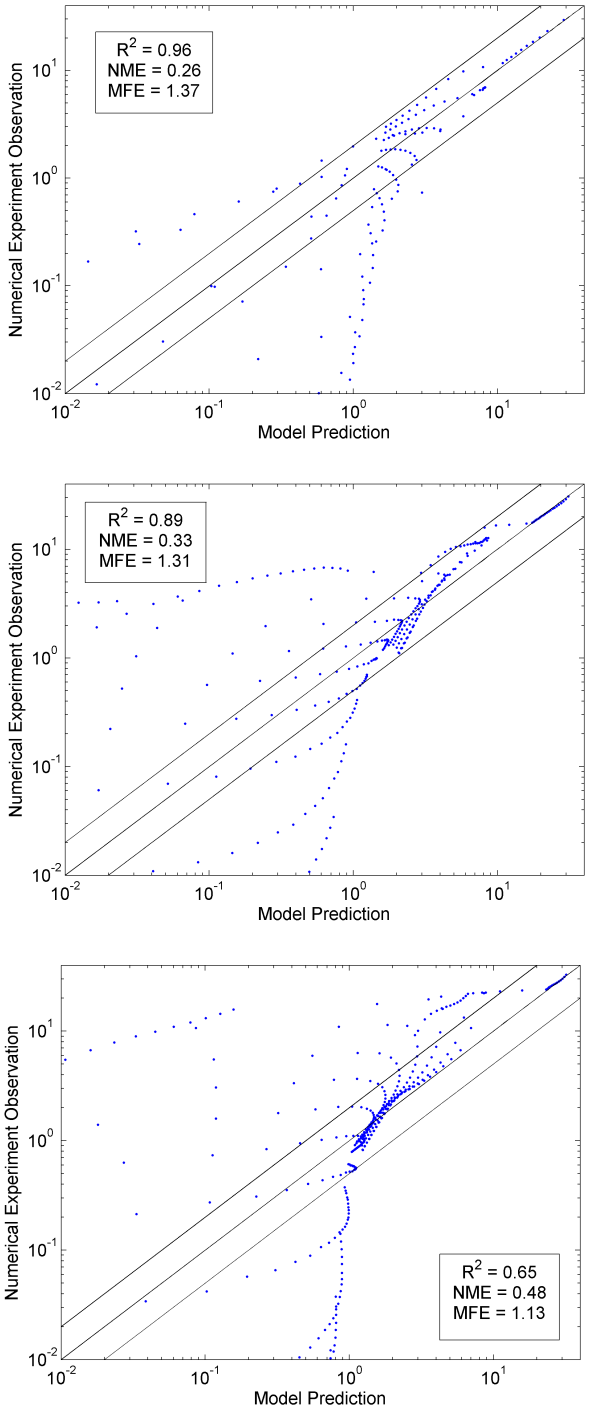

Figure 6.10: Comparison of modeled vs. predicted concentration for a) LAD = 1, b) LAD = 2, and c) LAD = 4. Outer lines show a factor of two difference. The model performs better at lower densities with higher R^2 and lower NME .

CHAPTER 7

CONCLUSION

The impact of solid and vegetative barriers on near-road air quality has recently become a popular topic for many researchers in a variety of fields as pollutant levels and human exposure are continually a concern. Much of this dissertation represents some of the earlier simulation work done in characterizing the impact of roadway features on near-road air quality. Specifically, I used computational fluid dynamics to simulate the subjects of two field studies, one studying the effects of atmospheric stability on concentration near a solid barrier performed in Idaho Falls, ID, and another studying the effect of vegetation on concentration performed in Chapel Hill, NC. Additionally, I simulated the conditions of a wind tunnel experiment which examined 12 different roadway configurations including solid barrier, depressed roadways, and elevated roadways.

In the solid barrier field study simulation I employed both a RANS and an LES turbulence model to judge the effectiveness of these models at capturing the flow in the vicinity of the barrier and the dispersion of a tracer gas. I found that the two models perform similarly for flat terrain, but the LES performs significantly better downwind of the barrier, particularly near the edges of the barrier. Therefore, the increased accuracy of the LES model may justify the greatly increased computational time. Overall, my LES simulations of the wind tunnel experiment and Idaho Falls field study showed very good agreement with both wind speed and tracer measurements. The vegetation barrier model performs reasonably well, showing good agreement with particle number concentration (though under predicting concentrations of particles less than

50 nm). However, there are some inconsistencies with the comparison of wind speed measurements. Possibly this model could be improved with use of an LES model adapted to include for the effect of vegetation on turbulence characteristics. After validating these models, I performed a variety of simulations to conduct numerical experiments in order to more fully understand the underlying mechanisms of the flow and observe the effect of various flow parameters on resulting concentrations.

The results of the wind tunnel experiment suggested, confirmed by our numerical simulations, that a solid barrier can greatly reduce concentration compared to a case without a barrier. In some cases, this reduction was upwards of 80%. Other roadway configurations also generally showed reduced downwind ground level concentration. However, in all of the roadway configurations, some locations showed an increase in concentration, either on the roadway or at the height of the obstacle. Vegetation barriers have a more complicated effect. Downwind of the vegetation there is a calm wake region with damps turbulent mixing which can result in increases in concentration. However, vegetation can effectively filter particulate matter, often resulting in large reduction in concentration.

I go on to develop a method of modifying a Gaussian plume dispersion model to account for the effects of a solid barrier. To my knowledge only one other group has produced such a model, and it did not accurately represent the concentration within the recirculation region. I used simulation data to show that the concentration field can be normalized by the barrier height, wind speed, and source strength. My model utilizes a multi-regime approach which divides the model domain into three distinct regions. Far from the barrier, the con-

centration field is prescribed by a standard Gaussian formulation, shifted some distance horizontally and vertically. In the barrier wake, I assumed a constant concentration created by strong mixing in the recirculation zone. A transition region is used to smoothly connect the concentration in the other areas. This model requires several empirically coefficients. I used simulation data to fit these parameters and compare with the wind tunnel experimental concentration. Overall, the model is quite accurate and correlated very well with experimental data. Inputs into the model are fairly simple, including atmospheric conditions, barrier height, and emission strength and it is computationally very cheap. This model will be a tool for those who use Gaussian plume models on a regular basis as it will further expand the usefulness of those tools.

I also created a similar Gaussian dispersion model modification for vegetation barriers. Behind the vegetation barrier, a very calm windbreak region damps vertical dispersion. However, a strong zone of turbulence which forms over the vegetation canopy eventually interacts with the plume causing rapid vertical dispersion. In the calm wake region behind the vegetation, the rate of decay is slowed. As the plume interacts with the band of high turbulence, concentration quickly decays. Thus we modified the vertical dispersion parameter to account for these changes. While I lacked experimental validation, it is the only model of its kind, and the strong correlation between the model and simulation data suggests that it could be a very worthwhile tool. I plan to further develop and refine this model to account for the stretching of the plume by non-uniform vertical dispersion.

BIBLIOGRAPHY

Adar, S. and Kaufman, J. (2007). Cardiovascular disease and air pollutants: evaluating and improving epidemiological data implicating traffic exposure. *Inhalation Toxicology*, 19(S1):135–149.

ANSYS, I. (2009). Ansys fluent 12.0 theory guide. ansys.

Aylor, D. E. (1975). Deposition of particles in a plant canopy. *Journal of Applied Meteorology*, 14(1):52–57.

Baldauf, R., Bailey, C., Cook, J., Cahill, T., Khlystov, A., Zhang, K., Cowherd, C., and Bowker, G. (2009). Can roadway design be used to mitigate air quality impacts from traffic? *Atmospheric Environment*, 43:697–705.

Baldauf, R., Thoma, E., Khlystov, A., Isakov, V., Bowker, G., Long, T., and Snow, R. (2008). Impacts of noise barriers on near-road air quality. *Atmospheric Environment*, 42(32):7502 – 7507.

Beckett, K. P., Freer-Smith, P., and Taylor, G. (1998). Urban woodlands: their role in reducing the effects of particulate pollution. *Environmental pollution*, 99(3):347–360.

Bouvet, T., Loubet, B., Wilson, J., and Tuzet, A. (2007). Filtering of windborne particles by a natural windbreak. *Boundary-Layer Meteorology*, 123(3).

Bowker, G. E., Baldauf, R., Isakov, V., Khlystov, A., and Petersen, W. (2007). The effects of roadside structures on the transport and dispersion of ultrafine particles from highways. *Atmospheric Environment*, 41(37):8128 – 8139.

Briggs, G. A. (1982). Similarity forms for ground-source surface-layer diffusion. *Boundary-Layer Meteorology*, 23(4):489–502.

Buccolieri, R., Gromke, C., Sabatino, S. D., and Ruck, B. (2009). Aerodynamic effects of trees on pollutant concentration in street canyons. *Science of The Total Environment*, 407(19):5247 – 5256.

Cahill, T. A. (2010). How does vegetation affect pollution removal? In *The Workshop on the Role of Vegetation in Mitigation Air Quality Impacts from Traffic Emissions. RTP, North Carolina*.

Chang, C.-H. and Meroney, R. N. (2003). Concentration and flow distributions in urban street canyons: wind tunnel and computational data. *Journal of Wind Engineering and Industrial Aerodynamics*, 91(9):1141 – 1154.

Chen, L., Goto, S., and Vassilicos, J. (2006). Turbulent clustering of stagnation points and inertial particles. *Journal of Fluid Mechanics*, 553:143–154.

Cleugh, H. (1998). Effects of windbreaks on airflow, microclimates and crop yields. *Agroforestry Systems*, 41(1).

Cowan, I. R. (1968). Mass, heat and momentum exchange between stands of plants and their atmospheric environment. *Quarterly Journal of the Royal Meteorological Society*, 94(402).

Cowan, I. R., Castro, I. P., and Robins, A. G. (1997). Numerical considerations for simulations of flow and dispersion around buildings. *Journal of Wind Engineering and Industrial Aerodynamics*, 67:535–545.

Davidson, C. I., Miller, J. M., and Pleskow, M. A. (1982). The influence of surface structure on predicted particle dry deposition to natural grass canopies. In *Long-Range Transport of Airborne Pollutants*, pages 25–43. Springer.

Deaves, D. and Harris, R. (1982). A note on the use of asymptotic similarity theory in neutral atmospheric boundary layers. *Atmospheric Environment (1967)*, 16(8):1889–1893.

Earsom, S., Hallett, R., Perrone, T., Poe, C., and Greenfield, M. (2010). Estimated land available for carbon sequestration in the national highway system.

Endalew, A. M., Hertog, M., Gebrehiwot, M. G., Baelmans, M., Ramon, H., Nicolai, B., and Verboven, P. (2009). Modelling airflow within model plant canopies using an integrated approach. *Computers and Electronics in Agriculture*, 66(1):9–24.

Finn, D., Clawson, K. L., Carter, R. G., Rich, J. D., Eckman, R. M., Perry, S. G., Isakov, V., and Heist, D. K. (2010). Tracer studies to characterize the effects of roadside noise barriers on near-road pollutant dispersion under varying atmospheric stability conditions. *Atmospheric Environment*, 44(2):204–214.

Finnigan, J. and Bradley, E. F. (1983). The turbulent kinetic energy budget behind a porous barrier: An analysis in streamline co-ordinates. *Journal of Wind Engineering and Industrial Aerodynamics*, 15(1):157–168.

Flemmer, R. and Banks, C. (1986). On the drag coefficient of a sphere. *Powder Technology*, 48(3):217–221.

Gowardhan, A. A., Pardyjak, E. R., Senocak, I., and Brown, M. J. (2011). A cfd-based wind solver for an urban fast response transport and dispersion model. *Environmental fluid mechanics*, 11(5):439–464.

Greens, S., Grace, J., and Hutchings, N. (1995). Observations of turbulent air flow in three stands of widely spaced sitka spruce. *Agricultural and Forest Meteorology*, 74(3):205–225.

Gromke, C., Buccolieri, R., Di Sabatino, S., and Ruck, B. (2008). Dispersion study in a street canyon with tree planting by means of wind tunnel and numerical investigations–evaluation of cfd data with experimental data. *Atmospheric Environment*, 42(37):8640–8650.

Gromke, C. and Ruck, B. (2007). Influence of trees on the dispersion of pollutants in an urban street canyonexperimental investigation of the flow and concentration field. *Atmospheric Environment*, 41(16):3287–3302.

Guha, A. (2008). Transport and deposition of particles in turbulent and laminar flow.

Hagler, G. S., Lin, M.-Y., Khlystov, A., Baldauf, R. W., Isakov, V., Faircloth, J., and Jackson, L. E. (2012). Field investigation of roadside vegetative and structural barrier impact on near-road ultrafine particle concentrations under a variety of wind conditions. *Science of the Total Environment*, 419:7–15.

Hagler, G. S., Tang, W., Freeman, M. J., Heist, D. K., Perry, S. G., and Vette, A. F. (2011). Model evaluation of roadside barrier impact on near-road air pollution. *Atmospheric Environment*, 45(15):2522–2530.

Hanna, S., Tehranian, S., Carissimo, B., Macdonald, R., and Lohner, R. (2002). Comparisons of model simulations with observations of mean flow and turbulence within simple obstacle arrays. *Atmospheric Environment*, 36(32):5067–5079.

Hargreaves, D. and Wright, N. G. (2007). On the use of the¡ i¿ k¡/i¿–ε model in commercial cfd software to model the neutral atmospheric boundary layer. *Journal of Wind Engineering and Industrial Aerodynamics*, 95(5):355–369.

HEI (2010). *Traffic-related air pollution: a critical review of the literature on emissions, exposure, and health effects*. Number 17. Health Effects Institute.

Heisler, G. M. and Dewalle, D. R. (1988). Effects of windbreak structure on wind flow. *Agriculture, Ecosystems and Environment*, 22–23(1):41 – 69.

Heist, D., Perry, S., and Brixey, L. (2009). A wind tunnel study of the effect of roadway configurations on the dispersion of traffic-related pollution. *Atmospheric Environment*, 43(32):5101–5111.

Hertel, O., Berkowicz, R., and Larssen, S. (1991). The operational street pollution model (ospm). In *Air Pollution Modeling and Its Application VIII*, pages 741–750. Springer.

Hiraoka, H. and Ohashi, M. (2008). A (¡ i¿ k¡/i¿–¡ i¿ ε¡/i¿) turbulence closure model for plant canopy flows. *Journal of Wind Engineering and Industrial Aerodynamics*, 96(10):2139–2149.

Hosker Jr, R. (1979). Empirical estimation of wake cavity size behind block-type structures. *Environmental Research Laboratories*, page 299.

Hosker Jr, R., Rao, K., Gunter, R., Nappo, C., Meyers, T., Birdwell, K., and White, J. (2003). Issues affecting dispersion near highways: light winds, intra-urban dispersion, vehicle wakes, and the roadway-2 dispersion model. Technical report.

Houston, D., Krudysz, M., and Winer, A. (2008). Diesel truck traffic in low-income and minority communities adjacent to ports: environmental justice implications of near-roadway land use conflicts. *Transportation Research Record: Journal of the Transportation Research Board*, 2067(1):38–46.

Huang, C. (1979). A theory of dispersion in turbulent shear flow. *Atmospheric Environment (1967)*, 13(4):453–463.

Hunt, J., Puttock, J., and Snyder, W. (1979). Turbulent diffusion from a point source in stratified and neutral flows around a three-dimensional hillpart i. diffusion equation analysis. *Atmospheric Environment (1967)*, 13(9):1227–1239.

Irwin, H. (1981). The design of spires for wind simulation. *Journal of Wind Engineering and Industrial Aerodynamics*, 7(3):361–366.

Jacobson, M. Z. (2005). *Fundamentals of atmospheric modeling*. Cambridge University Press.

Jones, W. and Launder, B. (1972). The prediction of laminarization with a two-equation model of turbulence. *International journal of heat and mass transfer*, 15(2):301–314.

Kaimal, J. C. and Finnigan, J. J. (1994). *Atmospheric boundary layer flows: their structure and measurement*. Oxford University Press.

Kenning, V. and Crowe, C. (1997). On the effect of particles on carrier phase turbulence in gas-particle flows. *International Journal of Multiphase Flow*, 23(2):403–408.

Kittelson, D. B. (1998). Engines and nanoparticles: a review. *Journal of aerosol science*, 29(5):575–588.

Kraichnan, R. H. (1970). Diffusion by a random velocity field. *Physics of Fluids (1958-1988)*, 13(1):22–31.

Lalic, B. and Mihailovic, D. T. (2004). An empirical relation describing leaf-

area density inside the forest for environmental modeling. *Journal of Applied Meteorology*, 43(4):641–645.

Lapple, C. and Shepherd, C. (1940). Calculation of particle trajectories. *Industrial & Engineering Chemistry*, 32(5):605–617.

Launder, B. and Sharma, B. (1974). Application of the energy-dissipation model of turbulence to the calculation of flow near a spinning disc. *Letters in heat and mass transfer*, 1(2):131–137.

Legg, B. and Powell, F. (1979). Spore dispersal in a barley crop: a mathematical model. *Agricultural Meteorology*, 20(1):47–67.

Lidman, J. K. (1985). Effect of a noise wall on snow accumulation and air quality. *Transportation Research Record*, 1033:79–88.

Lilly, D. K. (1992). A proposed modification of the germano subgrid-scale closure method. *Physics of Fluids A: Fluid Dynamics (1989-1993)*, 4(3):633–635.

Liu, J., Chen, J., Black, T., and Novak, M. (1996). E-ε modelling of turbulent air flow downwind of a model forest edge. *Boundary-Layer Meteorology*, 77(1):21–44.

Maerschalck, B., Janssen, S., Vankerkom, J., Mensink, C., van den Burg, A., and Fortuin, P. (2008). Cfd simulations of the impact of a line vegetation element along a motorway on local air quality. *Hrvatski meteorološki časopis*, 43(43/1):339–344.

Massey, B. S., Ward-Smith, A. J., and John, A. (1989). *Mechanics of fluids*, volume 45. Springer.

Massman, W. (1987). A comparative study of some mathematical models of the mean wind structure and aerodynamic drag of plant canopies. *Boundary-layer meteorology*, 40(1-2):179–197.

Maxey, M. (1987). The gravitational settling of aerosol particles in homogeneous turbulence and random flow fields. *Journal of Fluid Mechanics*, 174:441–465.

May, K. and Clifford, R. (1967). The impaction of aerosol particles on cylinders, spheres, ribbons and discs. *Annals of Occupational Hygiene*, 10(2):83–95.

McHugh, C., Carruthers, D., and Edmunds, H. (1997). Adms-urban: an air quality management system for traffic, domestic and industrial pollution. *International Journal of Environment and Pollution*, 8(3):666–674.

McNaughton, K. (1988). Effects of windbreaks on turbulent transport and microclimate. *Agriculture, Ecosystems and Environment*, 22–23(1):17 – 39.

Michael, D. and Norey, P. (1969). Particle collision efficiencies for a sphere. *Journal of Fluid Mechanics*, 37(03):565–575.

Miller, C. (1978). An examination of gaussian plume dispersion parameters for rough terrain. *Atmospheric Environment (1967)*, 12(6):1359–1364.

Morrison, F. A. (2013). *An introduction to fluid mechanics*. Cambridge University Press.

Neophytou, M., Gowardhan, A., and Brown, M. (2011). An inter-comparison of three urban wind models using oklahoma city joint urban 2003 wind field measurements. *Journal of Wind Engineering and Industrial Aerodynamics*, 99(4):357–368.

Nielsen, P. (1993). Turbulence effects on the settling of suspended particles. *Journal of Sedimentary Research*, 63(5).

Nokes, W. and Benson, P. (1984). Carbon monoxide concentrations adjacent to sound barriers. office of transportation laboratory, california department of transportation. Technical report, Report FHWA/CA/TL-84/04.

Nowak, D. J., Crane, D. E., and Stevens, J. C. (2006). Air pollution removal by urban trees and shrubs in the united states. *Urban forestry and urban greening*, 4(3):115–123.

Obukhov, A. (1971). Turbulence in an atmosphere with a non-uniform temperature. *Boundary-layer meteorology*, 2(1):7–29.

Patton, E. G., Shaw, R. H., Judd, M. J., and Raupach, M. R. (1998). Large-eddy simulation of windbreak flow. *Boundary-Layer Meteorology*, 87(2):275–307.

Perry, R., Chilton, C., and Kirkpatrick, S. (1999). *Chemical engineers handbook*. McGraw-Hill New York.

Petroff, A. and Zhang, L. (2010). Development and validation of a size-resolved particle dry deposition scheme for application in aerosol transport models. *Geoscientific Model Development*, 3(2):753–769.

Petroff, A., Zhang, L., Pryor, S., and Belot, Y. (2009). An extended dry deposition model for aerosols onto broadleaf canopies. *Journal of Aerosol Science*, 40(3):218–240.

Piskunov, V. (2009). Parameterization of aerosol dry deposition velocities onto smooth and rough surfaces. *Journal of Aerosol Science*, 40(8):664–679.

Pontiggia, M., Derudi, M., Busini, V., and Rota, R. (2009). Hazardous gas dispersion: a cfd model accounting for atmospheric stability classes. *Journal of hazardous materials*, 171(1):739–747.

Pope, S. B. (2000). *Turbulent flows*. Cambridge university press.

Raupach, M. and Thom, A. S. (1981). Turbulence in and above plant canopies. *Annual Review of Fluid Mechanics*, 13(1):97–129.

Raupach, M., Woods, N., Dorr, G., Leys, J., and Cleugh, H. (2001). The entrapment of particles by windbreaks. *Atmospheric environment*, 35(20):3373–3383.

Richards, P. and Hoxey, R. (1993). Appropriate boundary conditions for computational wind engineering models using the k- turbulence model. *Journal of wind engineering and industrial aerodynamics*, 46:145–153.

Rudinger, G. (1965). Some effects of finite particle volume on the dynamics of gas-particle mixtures. *AIAA journal*, 3(7):1217–1222.

Salam, M. T., Islam, T., and Gilliland, F. D. (2008). Recent evidence for adverse effects of residential proximity to traffic sources on asthma. *Current opinion in pulmonary medicine*, 14(1):3–8.

Santiago, J., Martin, F., Cuerva, A., Bezdenejnykh, N., and Sanz-Andres, A. (2007). Experimental and numerical study of wind flow behind windbreaks. *Atmospheric Environment*, 41(30):6406–6420.

Seinfeld, J. H. and Pandis, S. N. (2012). *Atmospheric chemistry and physics: from air pollution to climate change*. John Wiley & Sons.

Shimeta, J. and Jumars, P. A. (1991). Physical mechanisms and rates of particle capture by suspension feeders. *Oceanogr. Mar. Biol. Annu. Rev*, 29(19):l–257.

Slinn, W. (1982). Predictions for particle deposition to vegetative canopies. *Atmospheric Environment (1967)*, 16(7):1785–1794.

Smagorinsky, J. (1963). General circulation experiments with the primitive equations: I. the basic experiment*. *Monthly weather review*, 91(3):99–164.

Smirnov, A., Shi, S., and Celik, I. (2001). Random flow generation technique for large eddy simulations and particle-dynamics modeling. *Journal of Fluids Engineering*, 123(2):359–371.

Snyder, M. G., Venkatram, A., Heist, D. K., Perry, S. G., Petersen, W. B., and Isakov, V. (2013). Rline: a line source dispersion model for near-surface releases. *Atmospheric Environment*, 77:748–756.

Snyder, W. H. (1979). *The EPA meteorological wind tunnel: its design, construction and operating characteristics*. US Environmental Protection Agency, Office of Research and Development, Environmental Sciences Research Laboratory.

Steffens, J. T., Heist, D. K., Perry, S. G., Isakov, V., Baldauf, R. W., and Zhang, K. M. (2014). Effects of roadway configurations on near-road air quality and the implications on roadway designs. *Atmospheric Environment*, 94(0):74 – 85.

Steffens, J. T., Heist, D. K., Perry, S. G., and Zhang, K. M. (2013). Modeling the effects of a solid barrier on pollutant dispersion under various atmospheric stability conditions. *Atmospheric Environment*, 69:76–85.

Steffens, J. T., Wang, Y. J., and Zhang, K. M. (2012). Exploration of effects of a vegetation barrier on particle size distributions in a near-road environment. *Atmospheric Environment*, 50:120–128.

Sundaram, S. and Collins, L. R. (1997). Collision statistics in an isotropic

particle-laden turbulent suspension. part 1. direct numerical simulations. *Journal of Fluid Mechanics*, 335:75–109.

Sutton, O. (1947a). The problem of diffusion in the lower atmosphere. *Quarterly Journal of the Royal Meteorological Society*, 73(317-318):257–281.

Sutton, O. (1947b). The theoretical distribution of airborne pollution from factory chimneys. *Quarterly Journal of the Royal Meteorological Society*, 73(317-318):426–436.

Tanire, A., Oesterl, B., and Monnier, J. C. (1997). On the behaviour of solid particles in a horizontal boundary layer with turbulence and saltation effects. *Experiments in Fluids*, 23(6).

Thom, A. (1972). Momentum, mass and heat exchange of vegetation. *Quarterly Journal of the Royal Meteorological Society*, 98(415):124–134.

Tong, Z., Wang, Y. J., Patel, M., Kinney, P., Chrillrud, S., and Zhang, K. M. (2011). Modeling spatial variations of black carbon particles in an urban highway-building environment. *Environmental science and technology*, 46(1):312–319.

Vaillancourt, P. A. and Yau, M. (2000). Review of particle-turbulence interactions and consequences for cloud physics. *Bulletin of the American Meteorological Society*, 81(2):285–298.

Van Ulden, A. (1978). Simple estimates for vertical diffusion from sources near the ground. *Atmospheric Environment (1967)*, 12(11):2125–2129.

Venkatram, A. (1992). Vertical dispersion of ground-level releases in the surface boundary layer. *Atmospheric Environment. Part A. General Topics*, 26(5):947–949.

Venkatram, A., Snyder, M. G., Heist, D. K., Perry, S. G., Petersen, W. B., and Isakov, V. (2013). Re-formulation of plume spread for near-surface dispersion. *Atmospheric Environment*, 77:846–855.

Walklate, P., Weiner, K.-L., and Parkin, C. (1996). Analysis of and experimental measurements made on a moving air-assisted sprayer with two-dimensional air-jets penetrating a uniform crop canopy. *Journal of Agricultural Engineering Research*, 63(4):365–377.

Wang, H., Takle, E. S., and Shen, J. (2001). Shelterbelts and windbreaks: mathematical modeling and computer simulations of turbulent flows. *Annual Review of Fluid Mechanics*, 33(1):549–586.

Wang, Y. J., DenBleyker, A., McDonald-Buller, E., Allen, D., and Zhang, K. M. (2011). Modeling the chemical evolution of nitrogen oxides near roadways. *Atmospheric Environment*, 45(1):43–52.

Wang, Y. J. and Zhang, K. M. (2009). Modeling near-road air quality using a computational fluid dynamics model, cfd-vit-rit. *Environmental science & technology*, 43(20):7778–7783.

Wang, Y. J. and Zhang, K. M. (2012). Coupled turbulence and aerosol dynamics modeling of vehicle exhaust plumes using the ctag model. *Atmospheric Environment*, 59:284–293.

Wilson, J. D. (2004a). Oblique, stratified winds about a shelter fence. part i: Measurements. *Journal of applied meteorology*, 43(8):1149–1167.

Wilson, J. D. (2004b). Oblique, stratified winds about a shelter fence. part ii: Comparison of measurements with numerical models. *Journal of applied meteorology*, 43(10):1392–1409.

Wilson, N. R. and Shaw, R. H. (1977). A higher order closure model for canopy flow. *Journal of Applied Meteorology*, 16(11):1197–1205.

Xie, Z.-T. and Castro, I. P. (2009). Large-eddy simulation for flow and dispersion in urban streets. *Atmospheric Environment*, 43(13):2174–2185.

Yamartino, R. (1984). A comparison of several single-pass estimators of the standard deviation of wind direction. *Journal of Climate and Applied Meteorology*, 23(9):1362–1366.

Yule, A. (1980). Investigations of eddy coherence in jet flows.

Zhang, K. M. and Wexler, A. S. (2004). Evolution of particle number distribution near roadwayspart i: analysis of aerosol dynamics and its implications for engine emission measurement. *Atmospheric Environment*, 38(38):6643–6653.

Zhang, L., Gong, S., Padro, J., and Barrie, L. (2001). A size-segregated particle dry deposition scheme for an atmospheric aerosol module. *Atmospheric Environment*, 35(3):549–560.

Zhang, L., Wright, L. P., and Blanchard, P. (2009). A review of current knowledge concerning dry deposition of atmospheric mercury. *Atmospheric Environment*, 43(37):5853–5864.